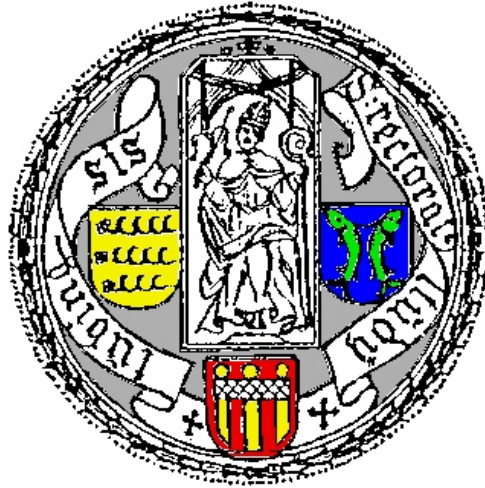# Production of $\pi^0\pi^0$ and $\pi^+\pi^+$ Pairs in Proton-Proton Collisions

Dissertation

zur Erlangung des Grades eines Doktors
der Naturwissenschaften
der Fakultät für Mathematik und Physik der
Eberhard-Karls-Universität Tübingen

vorgelegt von

Tatiana Skorodko
aus Moskau, Russland

2009

Tag der mündlichen Prüfung: 17. Juli 2009

Dekan: Prof. Dr. Wolfgang Knapp

1. Berichterstatter: Prof. Dr. Heinz Clement

2. Berichterstatter: Prof. Dr. Gerhard J. Wagner

Abstrakt

Die $\pi^0\pi^0$-Produktion im Proton-Proton-Stoß wurde von der Schwelle bis zu einer Strahlenergie von 1.3 GeV gemessen. Die Experimente wurden mit dem WASA 4π-Detektor mit internem Pellet-Target am CELSIUS Speicherring in Uppsala / Schweden durchgeführt. Zusätzlich wurde die $\pi^+\pi^+$-Production bei einer Einschussenergie von 1.1 GeV gemessen. Die an WASA erhaltenen $\pi^0\pi^0$- und $\pi^+\pi^+$-Daten stellen die ersten exklusiv vermessenen Daten von ausreichender Statistik im betrachteten Energiebereich dar, die Zugang zu differentiellen Observablen erlaubt.

Die extrahierten totalen und differentiellen Wirkungsqueschnitte für die Reaktionen $pp\rightarrow pp\pi^0\pi^0$ und $pp\rightarrow nn\pi^+\pi^+$ werden mit den theoretischen Vorhersagen des Valencia-Models verglichen. Für Energien nahe der Schwelle, d. h. bis zu 0.9 GeV, werden die $\pi^0\pi^0$-Daten quantitativ durch Anregung und Zerfall der Roper-Resonanz beschrieben. Dabei stellt sich heraus, dass der direkte Zerfall in den $N\sigma$-Kanal der klar dominierende Zwei-Pion-Zefallsprozess ist – was für die Interpretation der Roper-Resonanz als einer Monopol-Anregung des Nukleons spricht.

Bei Energien von $T_p > 1$ GeV, d. h. im Energiebereich oberhalb der Roper-Anregung, aber am Beginn der $\Delta\Delta$-Anregung, werden die beobachteten totalen und differentiellen Wirkungsquerschnitten sehr verschieden von den theoretischen Vorhersagen. Die differentiellen Wirkungsquerschnitte können allerdings zufriedenstellend beschrieben werden, wenn die Bildung der speziellen Konfiguration $(\Delta\Delta)_{0^+}$ angenommen wird. Darüber hinaus zeigen die $\pi^0\pi^0$-Daten eine kleine, aber systematische Erhöhung bei kleinen Massen im invarianten $\pi^0\pi^0$-Massenspektrum. Außerdem liegt der totale $pp\pi^0\pi^0$-Wirkungsquerschnitt weit unterhalb der theoretischen Vorhersagen, während gleichzeitig der $nn\pi^+\pi^+$-Wirkungsquerschnitt einen Faktor fünf größer ist als in diesen Rechnungen erwartet.

Eine modellunbeschränkte Isospin-Zerlegung der totalen Wirkungsquerschnitte liefert eine s-Kanal ähnliche Energieabhängigkeit der Roper-Anregung ebenso wie einen signifikanten Beitrag einer höher liegenden Isospin=3/2-Resonanz. Als möglicher Kandidat wird die $\Delta(1600)$-Resonanz diskutiert.

Abstract

The $\pi^0\pi^0$ production in proton-proton collisions has been measured in the energy range from threshold up to 1.3 GeV using the WASA 4π detector setup with an internal pellet target at the CELSIUS storage ring in Uppsala. In addition the $\pi^+\pi^+$ production has been measured at an incident energy of 1.1 GeV. The $\pi^0\pi^0$ and $\pi^+\pi^+$ data taken at WASA constitute the first exclusively measured samples of solid statistics in the considered energy range.

Total and differential cross sections for the $pp\rightarrow pp\pi^0\pi^0$ and $pp\rightarrow nn\pi^+\pi^+$ reactions are systematically compared to the Valencia model predictions. At incident energies close to threshold, i.e. up to 0.9 GeV, the $\pi^0\pi^0$ data can be successfully explained by excitation and decay of the Roper resonance. Its direct decay into the $N\sigma$ channel is found to be by far the dominating two-pion decay process – in favor of a monopole excitation of the Roper resonance.

At energy $T_p > 1$ GeV, i.e. in the energy region, which is beyond the Roper excitation but at the onset of $\Delta\Delta$ excitation, a behavior is observed which is different from the theoretical prediction both in differential and total cross sections. The differential cross sections for $\pi^0\pi^0$ channel in the $\Delta\Delta$ region can be described, if the special configuration $(\Delta\Delta)_{0^+}$ is assumed. Moreover, the $\pi^0\pi^0$ data exhibit a small systematic low-mass enhancement in the $\pi^0\pi^0$ invariant mass spectrum. The total $pp\pi^0\pi^0$ cross sections fall behind theoretical predictions, whereas the $nn\pi^+\pi^+$ cross section is a factor of five larger that expected.

A model-unconstrained isospin decomposition of the total cross sections points to a s-channel-like energy dependence of the Roper excitation as well as to a significant contribution of an isospin 3/2 resonance other than the $\Delta(1232)$. As a possible candidate the $\Delta(1600)$ is discussed.

Pour bien savoir les choses, il en faut savoir le détail ; et comme il est presque infini, nos connaissances sont toujours superficielles et imparfaites.

François de La Rochefoucauld

List of contents

1 Introduction

For the explanation of the world surrounding us we try for each natural phenomenon to develop a model for its description. And then we try to find evidences, which are in favor or in disfavor of this model. These are two steps, which allow us to understand better the laws of nature and motivate us to proceed to a better comprehension of nature.

Our present knowledge about the fundamental building blocks and the interactions between them are collected in the co-called Standard Model. The Standard Model (SM) states that the matter around us is made of particles called quarks and leptons. The SM describes three of the four known fundamental interactions: strong, weak and electromagnetic. The strong interaction is responsible for holding the quarks together in order to build up hadrons. The structure and interaction of hadrons are described by quantum chromodynamics (QCD), which is established as the fundamental theory of the strong interaction. Using perturbative methods QCD has given extremely good predictions in the perturbative region of high energy physics [1].

However, many phenomena cannot be treated by perturbation theory due to the increasing coupling strength for decreasing momentum transfer. There still exists no analytical method within the QCD framework to describe the low- energy phenomena that leads to a very rich partly understood phenomenology. For example, how the observed hadrons, including their wide resonance spectrum, are created by QCD dynamics is still insufficiently understood. The answer to this question relates to the basic many-body problem, how complex systems can be constructed from elementary ones.

A better comprehension of QCD can be developed only through precise and systematic calculations matched by equally accurate data. Furthermore, in order to really understand the issue of confinement, one needs first to explore the hadron spectrum. The spectrum can only be described, if we are able to state, which states are genuine quark model states, which ones are dynamically generated through channel couplings or which ones are exotics. For that purpose precise measurements of many properties of these states are needed and analysis tools have to be developed to separate the often overlapping resonances [2].

1.1 Experimental and theoretical situation

The production, decay and interaction of hadrons remains a main source in understanding QCD in the non-perturbative region. Two-pion production reactions at low and intermediate energies are one of the possible tools to systematically study the hadron structure. While for photo- and pion-induced two-pion production reactions a wealth of data have been recently obtained (from ELSA, MAMI, SLAC, Saclay), the data base for nucleon-induced reactions is still much poorer and there are still a lot of questions to be learned about physics in these reactions. Up to the beginning of the experiments described in this thesis, only two main sources for $\pi\pi$ production at low and intermediate energies existed. The first one is bubble-chamber data measured in a rather wide range of energies from threshold up to the GeV region , but mostly with poor statistics [3]. From these data only total cross sections for several $\pi\pi$ production reactions are available. Another data sample includes exclusive measurements on the $pp{\rightarrow}pp\pi^+\pi^-$ reaction performed at the PROMICE-WASA detector [4,5]. These data have much better statistics but have been obtained only at 0.75 and 0.775 GeV.

Already from the first Brookhaven meson production experiments with a Wilson chamber it was concluded that the angular distributions of emitted particles agree with a model, where the nucleon is excited to an intermediate resonant state, which subsequently decays by emission of a meson [6].

To describe $\pi\pi$ production in the energy range up to several GeV an isobaric nucleon model has been suggested [7]. In this model one assumed that the resonances (isobars) with isospin I=1/2 and I=3/2 were predominantly responsible for pion production at energies from 0.8 to 3 GeV and the decay of the isobar was treated independently of possible interactions between its decay products and the other particles in the collision. It was assumed that isobars were produced in relative S state and decayed isotropically. The relative probability for isobar formation was related to the experimentally measured total interaction cross sections for the pion-nucleon system in the I=1/2 or I=3/2 state. Originally in this model one assumed that the isospin I=3/2 resonance corresponds to the Δ-resonance and the isospin I=1/2 one corresponds to resonances with mass m_1=1.51 GeV and m_2=1.68 GeV.

This model has been developed further to a full reaction model including also non-resonance terms by the Valencia theoretical group ("Valencia model") at the end of the nineties. These calculations became a quantitative step forward in the attempt to understand and describe $NN{\rightarrow}NN\pi\pi$ reaction data quantitatively at energies from threshold up to 1.5 GeV [8].

The Valencia model (VM) includes amplitudes generated by a chiral pion-nucleon Lagrangian (non-resonant chiral term) plus amplitudes describing the Δ and the Roper excitations. All amplitudes have been studied asserting their relevance as a function of energy. One observes that the importance of the different amplitudes varies appreciably from channel to channel. Hence the combined information from these channels should be a crucial test of this model.

Furthermore, the model has been developed as "phenomenological absolute" calculations: to evaluate total cross sections for different channels no single experimental point in the $NN{\to}NN\pi\pi$ data was used for normalization. The coupling constants and cut off parameters used in the calculations have been extracted from data obtained in other experiments.

In the channels, where the two pions can be in an isospin $I=0$ state, as $\pi^+\pi^-$ and $\pi^0\pi^0$, the model calculations predict that the Roper excitation in one of the nucleons and its decay $N^*{\to}N(\pi\pi)_{I=0}$ is a dominant production mechanism at energies close to the threshold. As the energy increases, the Roper decay via the Δ resonance $N^*{\to}\Delta\pi{\to}N(\pi\pi)_{I=0}$ gives an increasing contribution to the cross section. At energies $T_p > 1.3$ GeV the excitation of a Δ in each of the nucleons becomes the main production mechanism. Other VM terms have been found to play a minor role in $\pi^+\pi^-$ and $\pi^0\pi^0$ productions.

Also, the model calculations show that the Roper resonance is excited dominantly by effective σ exchange. Its contribution to the total cross section is larger by one order of magnitude than that from correlated $\pi+\rho$ exchange.
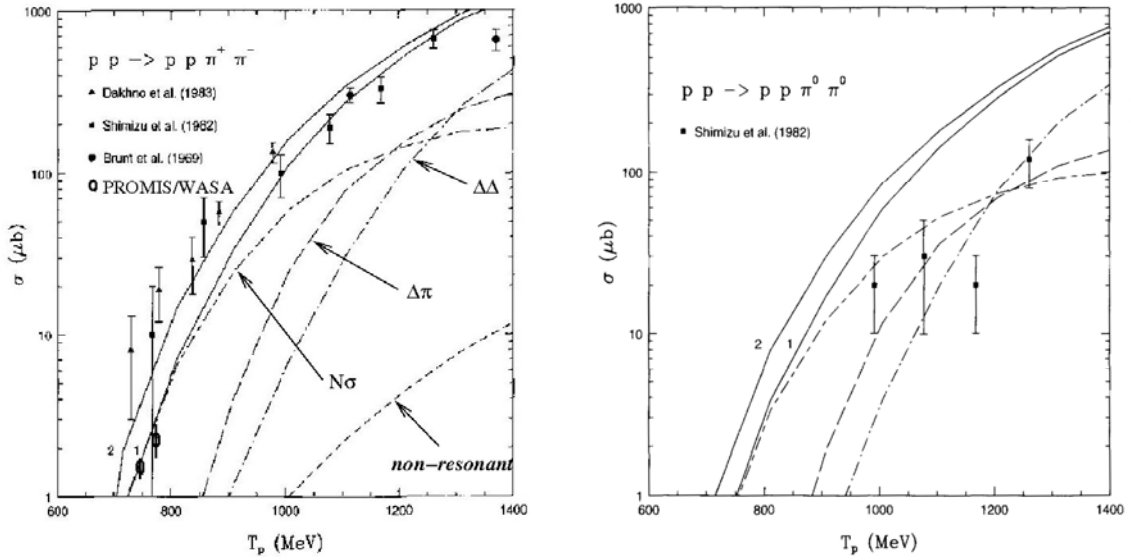
Figure 1.1 *Total cross section as a function of the incoming proton kinetic energy for the reaction $pp{\to}pp\pi^+\pi^-$ (left) and $pp{\to}pp\pi^0\pi^0$ (right). The solid lines give the full Valencia model calculations for two parameterizations of the Roper excitation (from Ref. [8]).*

Fig. 1.1 exhibits the energy dependence of the total cross sections for the reaction channels $pp{\to}pp\pi^+\pi^-$ and $pp{\to}pp\pi^0\pi^0$. The plotted data describe the experimental situation before the start of this work. The plotted curves denote the VM calculations. In Fig. 1.1 (left) one can see that the VM calculations give a good account for the total cross section of the $pp{\to}pp\pi^+\pi^-$ reaction as given by the bubble-chamber data in the energy range from threshold up to 1.4 GeV.

In order to check the VM predictions about the dominant role of the Roper excitation in $(\pi\pi)_{I=0}$ channels at low energies, exclusive measurements of the $\pi^+\pi^-$ channel have been performed at T_p=0.75 and 0.775 GeV using the

PROMICE/WASA detector at the Celsius storage ring [9]. The good statistics obtained in these experiments allows not only to compare the measured total cross sections with the predicted ones, but also to perform in detail the analysis of the features emerging in the differential cross sections.

To see, whether the reaction proceeds via Roper excitation, the $\pi^+\pi^-$ differential distributions have been inspected in Ref. [5] with the co-called Roper ansatz. In this ansatz the leading term of the two-pion Roper decay is given by:

$$A \sim 1 + c\vec{k}_1 \cdot \vec{k}_2 (3 \cdot D_{\Delta^{++}} + D_{\Delta^0})$$

1.1

In the full reaction amplitude this factor A has been complemented by the propagators for σ exchange and N^* excitation. The full reaction amplitude also includes an expression for the final state interaction (FSI) between two outgoing protons in relative s-wave. The constant 1 stands for the process $N^* \to N\sigma$ and the scalar product $k_1 \cdot k_2$ of the pion momenta k_1 and k_2 in the overall cm system describes double p-wave decay of the route $N^* \to \Delta\pi \to N\pi\pi$. $D_{\Delta^{++}}$ and D_{Δ^0} are the Δ^{++} and Δ^0 propagators correspondingly. The constant c gives the relative strength between the two Roper decay roots. It was treated in Ref. [5] as a parameter to be adjusted to the data, in particular to the distribution of the invariant mass $M_{\pi\pi}$ and of the opening angle $\delta_{\pi\pi}$ between two pions in the overall cm system. These two distributions, which are most sensitive to the parameter c, are shown in Fig. 1.2. The analysis of the $M_{\pi\pi}$ and $\delta_{\pi\pi}$ distributions has shown that even at energies close to the threshold, where the direct Roper decay $N^* \to N\sigma \to N(\pi\pi)_{I=0}$ has to give the main production contribution, a good description of the data requires a coherent admixture from the decay root $N^* \to \Delta\pi$ (Fig. 1.2). With c being adjusted appropriately a quantitative description almost of all observables both at T_p=0.75 and 0.775 GeV has been obtained. Only the distributions for the invariant masses $M_{p\pi^+}$, $M_{p\pi^-}$ and for the scattering angle $\Theta_\pi^{\pi\pi}$ in $\pi^+\pi^-$ subsystem show slight but systematic deviations.

Having fitted the parameter c, the ratio of partial decay widths has been calculated in Ref. [5] as

$$R(M_{N^*}) = \frac{\Gamma_{N^* \to \Delta\pi}(M_{N^*})}{\Gamma_{N^* \to N\sigma}(M_{N^*})} = \frac{9}{8}c^2 \frac{\int |M_{\Delta\pi}|^2 \, dM_{p\pi^+}^2 dM_{\pi^+\pi^-}^2}{\int |M_{N\sigma}|^2 \, dM_{p\pi^+}^2 dM_{\pi^+\pi^-}^2}$$

1.2

in dependence of the excited N^* mass with the matrix elements $M_{N\sigma} = 1$ and $M_{\Delta\pi} = k_1 \cdot k_2 (3D_{\Delta^{++}} + D_{\Delta^0})$. The factor 9/8 denotes isospin coupling coefficients. The ratio *R(1440)*, extrapolated to the conventional Roper mass of M_{N^*}=1440 MeV, has been obtained as 3.4(3). This result is in a good agreement with the PDG value 4(2). However, it has been noticed that $R(M_{N^*})$ is strongly

dependent on the assumed mass of the Roper resonance due to $\langle k_1 k_2 \rangle^2$. So already at $M_{N^*} = 1371\,\text{MeV}$ the value of R decreases to 1.2(1).
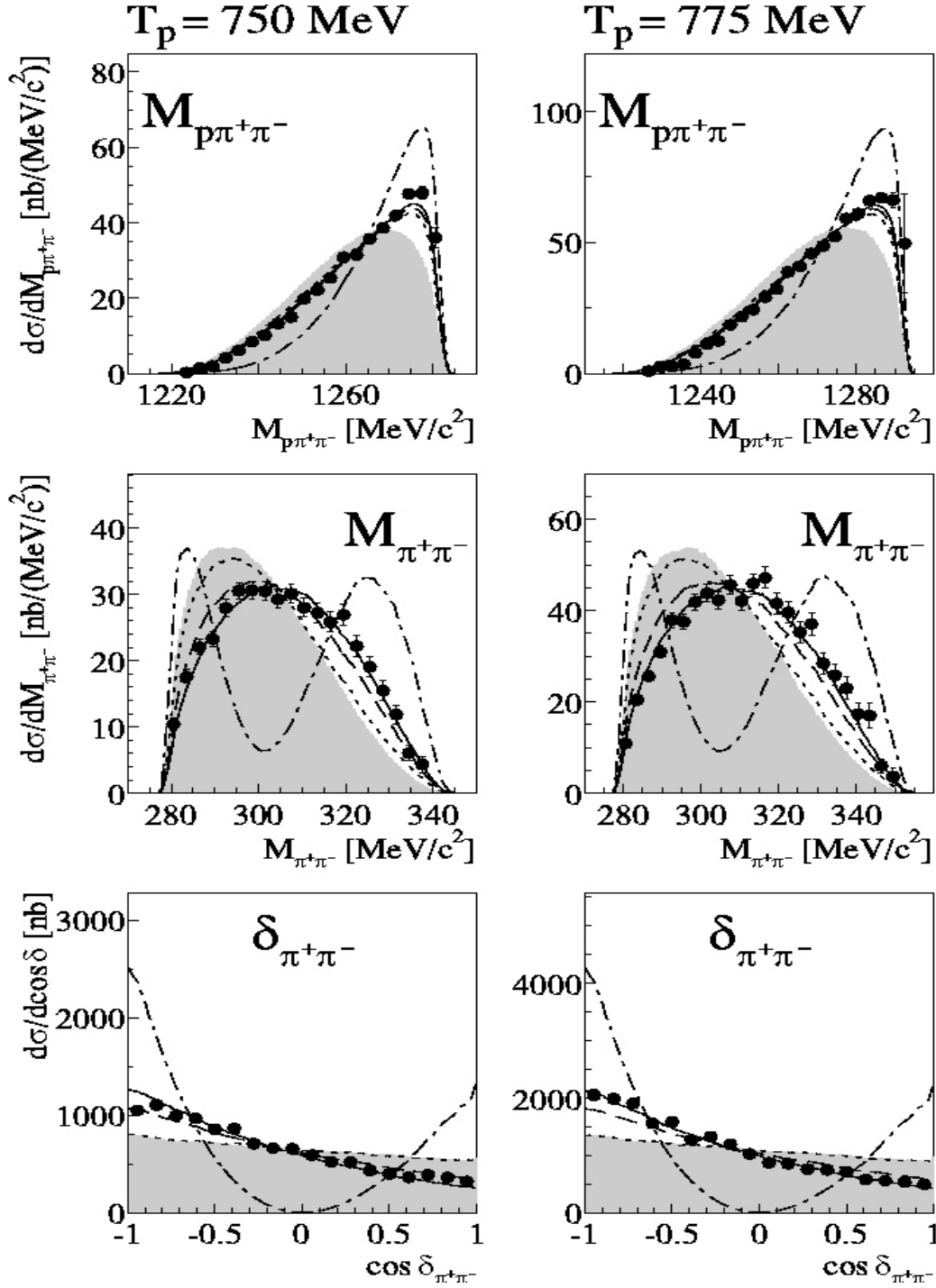
Figure 1.2 *Distribution of the invariant masses* $M_{p\pi^+\pi^-}$, $M_{\pi^+\pi^-}$ *and the opening angle* $\delta_{\pi^+\pi^-}$ *between two pions in the cms for* $T_p = 0.75$ *(left) and 0.775 GeV (right) from [5]. The data are shown in comparison to phase space (shaded area) and MC simulations for pure decay* $N^* \to N\sigma$ *(dotted), pure decay* $N^* \to \Delta\pi$ *(dashed-dotted) and their coherent sum (dashed and solid given for two different parameters c).*

At T_p=0.75 and 0.775 GeV the experimental $M_{p\pi^+}$ and $M_{p\pi^-}$ spectra show some asymmetry in their distributions. Whereas the $M_{p\pi^-}$ spectrum exhibits a slight shift towards smaller masses relative to the phase space distribution, the $M_{p\pi^+}$ spectrum shows a shift towards higher masses. This effect was expected to be described within the Roper ansatz (1.1), which expresses the known preference of the Δ^{++} excitation over the Δ^0 excitation. However, the data would prefer an even stronger Δ^{++} predominance. In Ref. [4, 5] it was noted that the 'ad hoc' ansatz:

$$A \sim (1 + c_1 \vec{k}_1 \cdot \vec{k}_2) D_{\Delta^{++}} \qquad\qquad 1.3$$

provides an excellent description of all $\pi^+\pi^-$-data of T_p=0.75 and 0.775 GeV including the asymmetry between the $M_{p\pi^+}$ and $M_{p\pi^-}$ distributions. It also was noted there that the admixture of the $N^* \to \Delta\pi$ branch to the dominant $N^* \to N\sigma$ branch adjusted to the data just corresponds on average to that of the pions four-vector scalar product $(1 + c_1 \vec{k}_1 \cdot \vec{k}_2) \sim (\omega_1\omega_2 - \vec{k}_1\vec{k}_2) = k_1^\mu k_2^\nu$.

To solve the problem with the asymmetry between invariant mass $M_{p\pi^+}$ and $M_{p\pi^-}$ spectra in Ref. [10] one has assumed that the observed difference might be better described by use of the reaction amplitude:

$$A \sim a + b \cdot k_1^\mu k_2^\nu [D_{\mu\upsilon}(P_{\Delta^0}) + 3 \cdot D_{\mu\upsilon}(P_{\Delta^{++}})] \qquad\qquad 1.4$$

where k_1, k_2 are pions 4-momenta, P_{Δ^0} and $P_{\Delta^{++}}$ are 4-momenta of the Δ^0 and Δ^{++}, respectively. $D_{\mu\upsilon}(P)$ stands for the Δ- propagators, a and b are adjustable parameters. However, except of a Lorentz-invariant representation, this description is not principally different from the Roper ansatz: the parameter a can be considered for the process $N^* \to N\sigma$ and the Roper decay $N^* \to \Delta\pi$ can be associated with the second term from formula (1.4) with the Roper-propagator included in b. However this ansatz does not lead to any significant improvement as compared to the non-relativistic Roper ansatz (1.1), see Fig. 1.3.

Another model for the $\pi^+\pi^-$ production at low energy has been suggested in Ref. [11]. In contrast to the Valencia calculations, which include no dynamical correlations, this model assumes that close to threshold the $pp \to pp\pi^+\pi^-$ reaction is dominated by production and decay of the σ meson, which appears as a dynamical resonance in $\pi\pi$ rescattering. The $\pi\pi$ scattering amplitude in I=0 has been constructed in chiral loop calculations and has been supplemented by a scalar factor for the absolute production strength. The main manifestation from dynamical correlations should be seen in the distributions of the invariant mass $M_{\pi\pi}$ and in the opening angle $\delta_{\pi\pi}$.
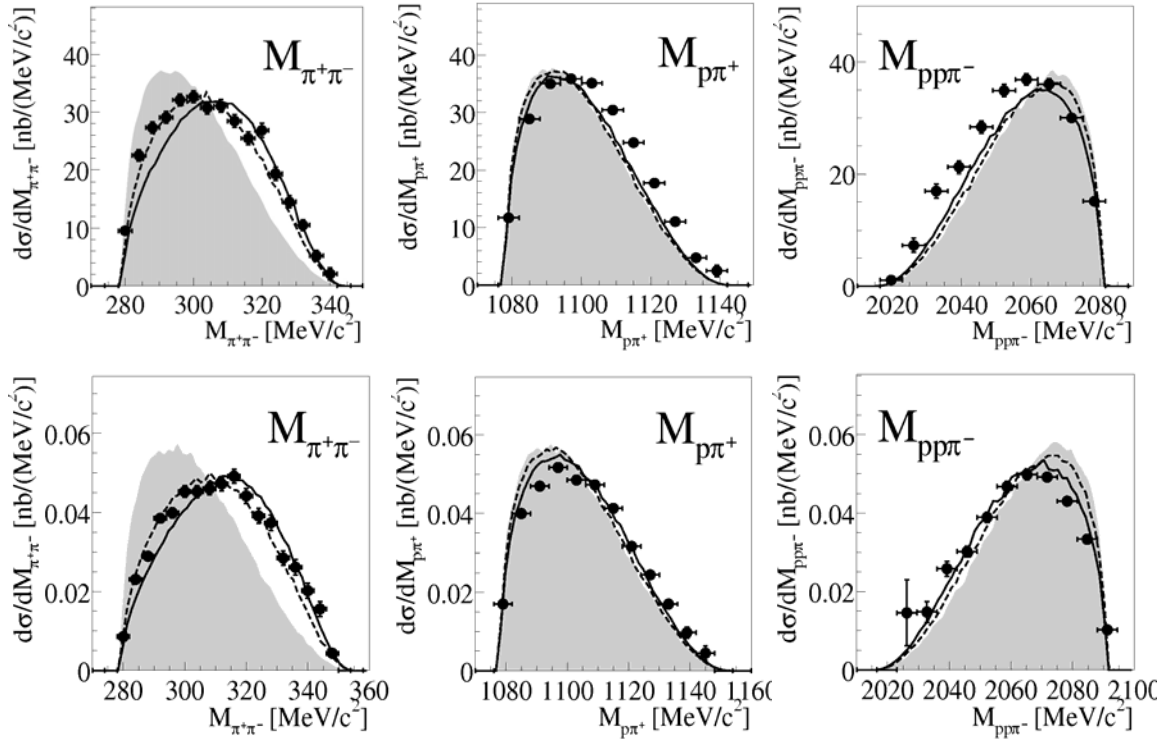
Figure 1.3 *Invariant masses* $M_{\pi^+\pi^-}$, $M_{p\pi^+}$, $M_{pp\pi^-}$ *at T_p=0.75 GeV (top) and 0.775 GeV (bottom). Phase space is shown as shaded area, dotted lines are the Roper ansatz calculations, solid ones are calculations according to formula (1.4) with parameters adjusted to the data at T_p=0.775 GeV.*
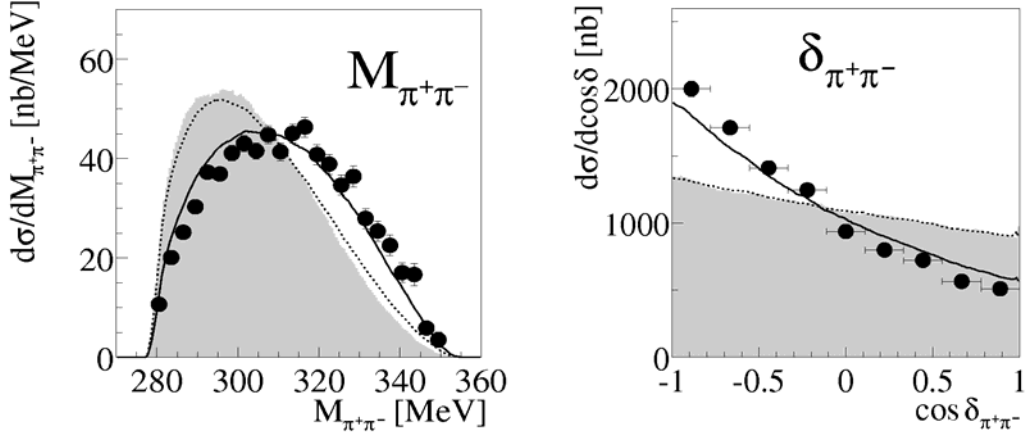
Figure 1.4. *Invariant mass and opening angle between two pions in $\pi^+\pi^-$ data at beam energy 0.775 GeV. Phase space is shown as shaded area, dotted lines show the FSI effect and solid ones correspond to the full calculation from Ref. [11] including $\pi\pi$ rescattering.*

Indeed, the experimental distributions at beam energies 0.75 and 0.775 GeV are very well described by these chiral loop calculations (Fig. 1.4).

The investigation of $\pi^0\pi^0$ production, the second possible channel with two pions in the *I=0* state, has been planned as a cross check of conclusions obtained for the $\pi^+\pi^-$ production. Furthermore, we would like to check bubble-chamber results for

$\pi^0\pi^0$ total cross sections, which show unexpected large discrepancies to the Valencia model predictions at energies of more than 1 GeV (Fig. 1.1, right). To clarify this situation and also to check the Valencia model at low and intermediate energies for $\pi^0\pi^0$ production, measurements with the CELSIUS-WASA detector setup were performed at the Theodor Svedberg Laboratory (TSL) in Uppsala in the energy region T_p=0.775 – 1.3 GeV.

2 CELSIUS/WASA experimental setup

2.1 CELSIUS storage ring

The experiment was performed in Uppsala at the Theodor Svedberg Laboratory (TSL), the national Swedish facility for accelerator based research operating two accelerators. The first accelerator is the Gustav Werner Cyclotron. It accelerates protons, deuterons and heavier ions, which can be injected into the second CELSIUS ring, a combined accelerator and storage ring (Fig. 2.1). The CELSIUS accelerator operates in cycles, it starts with the injection of protons from a cyclotron, usually by converting the H^2-ions to protons in a 20 mg/cm^2 carbon foil and then, during ramping, the circulating a bunch of protons accelerating them to the final beam energy. In the next step, called flat top, the beam energy is kept constant and data are measured. After the flat top, the beam is decelerated and dumped. Some of the beam properties are shown in Tab. 2.1. For proton beam energies up to 550 MeV electron cooling can be used to decrease the momentum spread of the beam.
In this thesis data were obtained only by use of a proton beam.

	uncooled	cooled
circumference [m]	81.8	
maximum proton energy [MeV]	1450	550
relative momentum spread $\Delta p/p$	$2 \cdot 10^{-3}$	$2 \cdot 10^{-4}$
beam cross section at target (hor./vert.) [mm]		5
injection energy	20/10	2/1
final energy	5/2.5	2/1
beam divergence at target [mrad]	9	0.9
number of stored protons	$5 \cdot 10^{10}$	$1 \cdot 10^{10}$
beam current [mA]	27	4.5

Table 2.1 *Parameters of the CELSIUS proton beam*

2.2 CELSIUS/WASA detector setup

A cross view of the WASA detector is presented in Fig. 2.2. It was designed as a 4π detector for measurements of rare decays of light meson produced in reactions between protons in CELSIUS ring and hydrogen pellet targets. The setup can be divided into a pellet-target system, forward and central part.
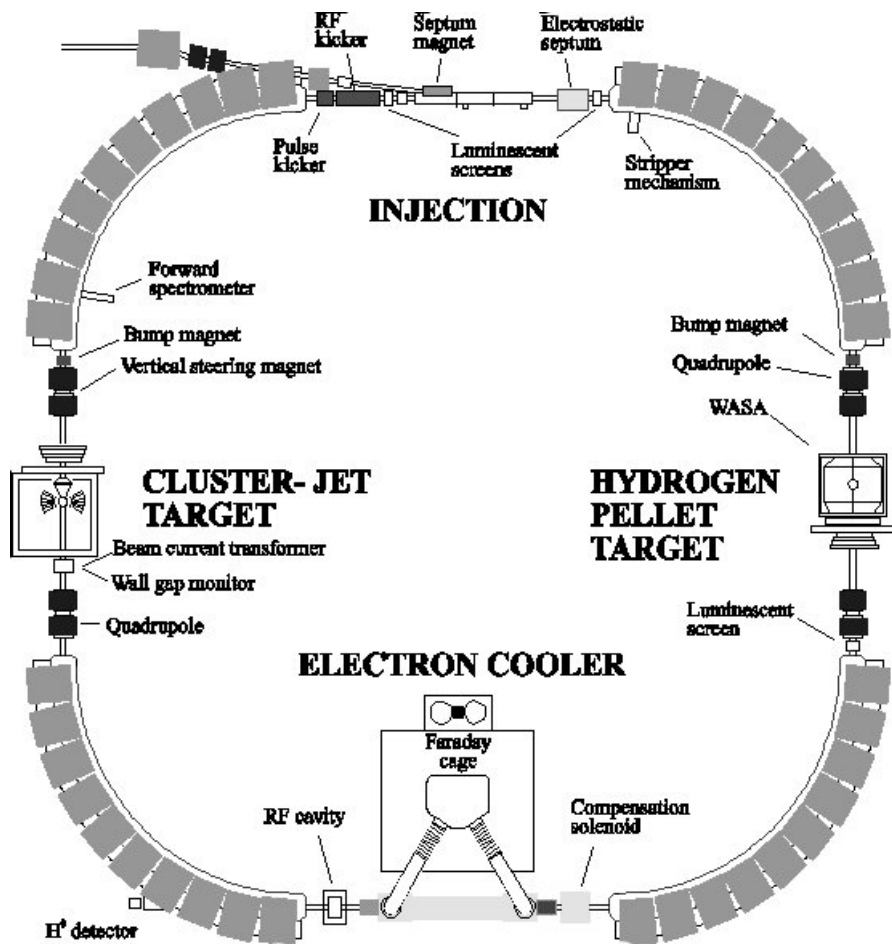
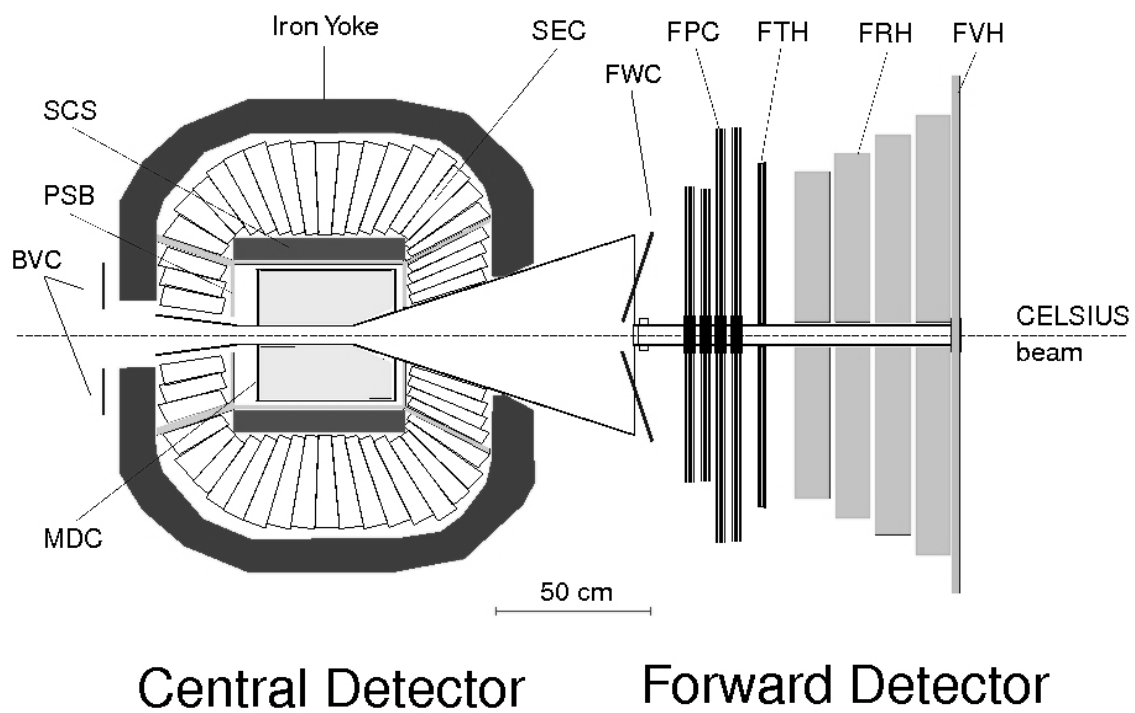Figure 2.1 *Top view of the CELSIUS accelerator.*

Central Detector   **Forward Detector**

Figure 2.2. *Cross view of the WASA detector.*

2.2.1 Pellet-target system

The pellet target (fig. 2.3) provides a narrow beam of frozen hydrogen (or deuterium), which cross the WASA detector perpendicular to the beam axis. In the ideal case, at each moment only one pellet is in the beam region.

The pellets are generated by breaking up a liquid hydrogen jet into uniformly sized droplets by acoustical excitation of the jet nozzle. The pellets freeze by evaporation when they pass the droplet chamber. The pellet beam is collimated by the skimmer and travels down the narrow pellet tube to the circulated proton beam. After crossing the CELSIUS beam, pellets are collected in the pellet dump [12].

Some of the pellet properties are shown in Tab. 2.2.

Pellet diameter [μm]	20-30
Pellet frequency (at interaction vertex) [kHz]	5-15
Pellet velocity [m/s]	89
Pellet-pellet distance [mm]	9-20
Pellet stream diameter (at CELSIS beam) [mm]	2-4
Effective target thickness [$s^{-1} \cdot cm^{-2}$]	$> 10^{15}$

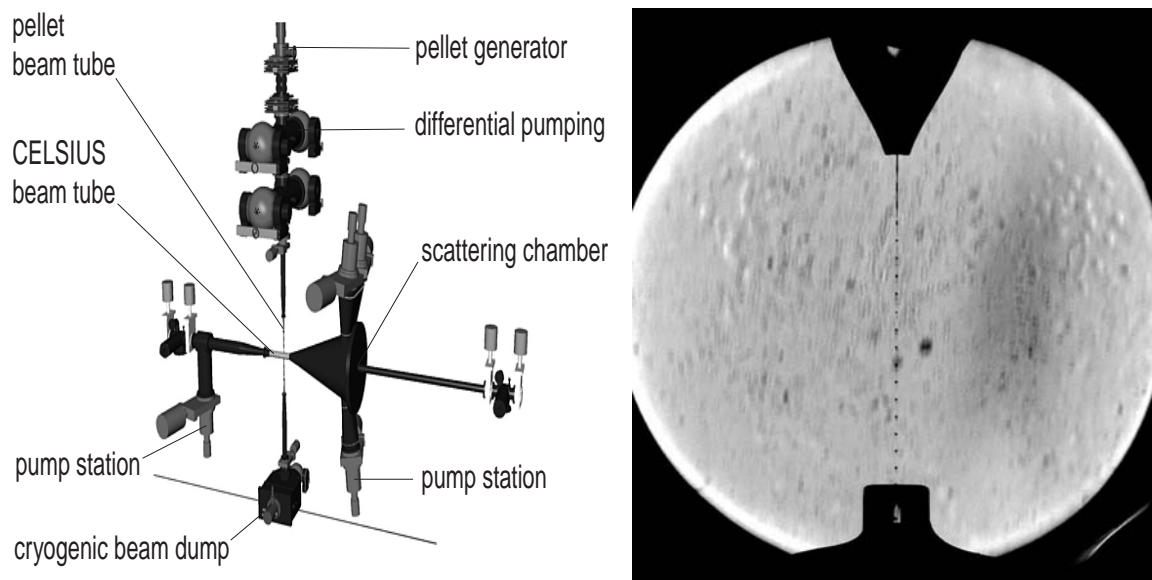Table 2.2 *Parameters of the pellet target.*

Figure 2.3 *Schematic view of the pellet target (left) and a photograph with the pellet nozzle, which creates a stream of liquid hydrogen droplets (right).*

2.2.2 Central Detector

The central detector (CD) covers almost 4π steradians and includes a CsI calorimeter (SEC) and a magnetic spectrometer, which consists on a superconducting solenoid (SCS) surrounding a plastic scintillator barrel (PSB) and a mini drift chamber (MDC). The solenoid has a wall thickness of only 7 mm, in order to avoid electromagnetic showers and not to change much the initial energy of particles. With the solenoid it is possible to generate axial magnetic fields up to 1.3 Tesla, which provides the possibility to determine the particle charge and measure their momentum in the MDC. The fast signal from the plastic scintillator barrel is used for the first-level trigger and its analog information about the deposited energy loss can be used for particle identification.

Scintillator Electromagnetic Calorimeter - SEC
SEC consists of 1012 sodium-doped CsI scintillating crystals (Fig. 2.4) placed between the superconducting solenoid and the iron yoke. Their primary purpose is to detect and measure photons, electrons and positrons. One can also measure the energy of pions and protons in the calorimeter. One has used CsI(Na) instead of the more commonly used CsI(Tl) scintillators, for the following reasons:
1. The emission peak at 420 nm matches well the bi-alkali S11 photocathode of the used PM tubes.
2. CsI(Na) gives less afterglow than CsI(Tl) and has a shorter scintillation decay time.
3. It is more resistant against radiation. Irradiated by a proton beam corresponding to 10 years of operation these crystals did not show any visible change in their performance [13].
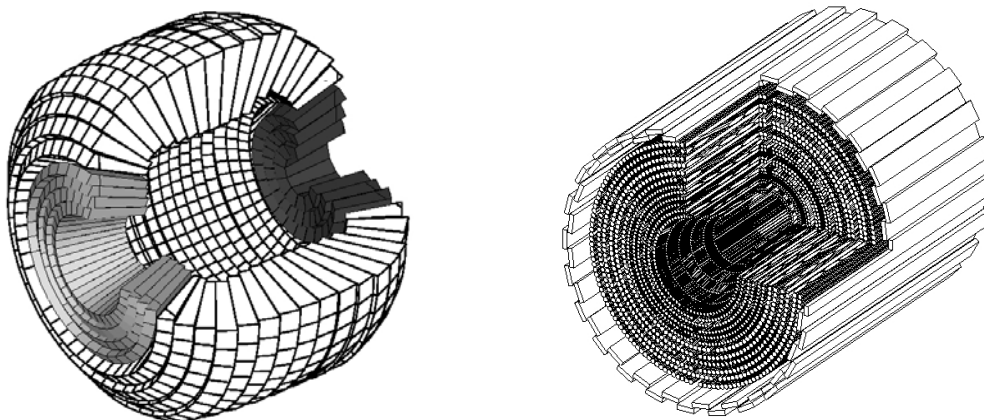Some of the properties of SEC are shown in Tab. 2.3.

Figure 2.4 *The scheme of the Scintillating Electomagnetic calorimeter (left): the marked parts correspond to the forward (SEF) and backward (SEB) parts. The scheme of the MDC, enclosed by the Plastic Barrel (right).*

amount of sensitive material [g/cm^2]	≈ 135
radiation lengths [g/cm^2]	≈ 16
nuclear interaction lengths [g/cm^2]	~ 0.8
nonuniformity of the signal along the crystal	$< 15\%$
signal decay time [ns]	650
geometric acceptance:	96%
polar angle	20^0-169^0
azimutal angle	0^0-360^0
max kinetic energy for stopping	
π/proton/deuteron [MeV]	190/400/500
scattering angle resolution	$\sim 5^0$ (FWHM)
time resolution [ns]:	
charged particles	5 (FWHM)
photons	≈ 40 (FWHM)
energy resolution:	
charged particles	$\approx 5\%$ (FWHM)
photons	$\approx 8\%$ (FWHM)
π and η results from γγ decay:	
energy resolution π /η	10 %/20 % (FWHM)
angular resolution π /η	7^0/7^0 (FWHM)

Table 2.3 *Properties of the SEC.*

Mini Drift Chamber – MDC

The MDC is a cylindrical drift chamber (Fig. 2.4 (right)), consisting of thin-walled (25 μm) aluminized mylar straw tubes. 1738 straw tubes in 17 cylindrical layers were used. Nine layers are parallel to the beam direction and the other eight layers have small skew angles (6-9 degrees) with respect to the beam axis in order to allow for position sensitivity in z-direction. The MDC is placed within the magnetic field of the solenoid and covers scattering angle from 24^0 to 154^0. Detailed information about the present performance of the MDC can be found in [15].

Superconducting solenoid – SCS

The ultra-thin walled superconducting solenoid magnet [14] has been developed in collaboration with KEK (Tsukuba) and Nippon Kokan Co., Ltd. (Kawasaki).The solenoid, with a size of 554 mm in diameter, 465 mm in length and a cold mass of 20 kg, was positioned in the central part of the WASA detector.

Its purpose is to provide a central axial magnetic field, up to 1.3 Tesla, for measuring charged particle moment in the MDC. It also protects the CD against low-energy delta electrons copiously produced in the interaction of beam particles with the pellets.

The return path for the magnetic flux is provided by a yoke, made out of 5 tons of pure iron with very low carbon content. The yoke also shields the detector readout electronics from the magnetic field and serves as a support for the SEC detector elements [13].

Plastic Scintillator Barrel – PSB
The plastic scintillator barrel (Fig. 2.5), prepared by the Warsaw group, provides a fast logic signal for the first level trigger and also its analog signal could be used for particle identification by the ΔE-E technique. The PSB was placed just inside the superconducting solenoid surrounding the mini-drift-chamber. It consists of a cylindrical part and two end caps. In the cylindrical part the layers have a small overlap between neighboring elements.
Some of the properties of the PSB are shown in Tab 2.4.

Radius [mm]	230
Length of the cylindrical part [mm]	550
Plastic scintillator thickness [mm]	8
Total number of elements	146
Bin width in azimuthal angle	7.5
Time resolution [ns]	5 (FWHM)
Energy resolution:	
Elastic scattering of 400 MeV protons	~30% (FWHM)

Table 2.4 *Properties of the plastic scintillator barrel.*
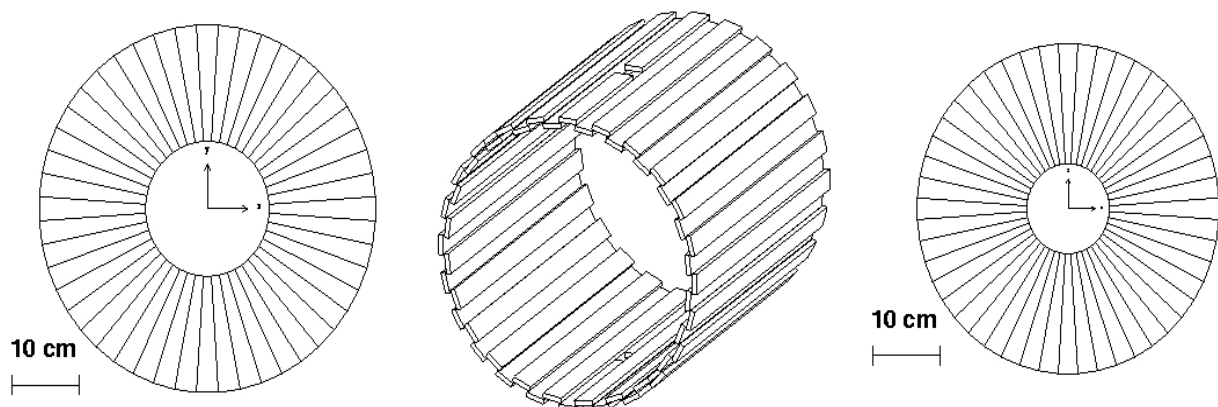

Figure 2.5 *The scheme of the PSB: forward (left), central (middle) and backward (right) parts.*

2.2.3 Forward Detector

The forward detector covers scattering angles from 3^0 to 18^0 and provides energy and angle reconstruction of the charged particles emitted into the forward cone. As detector material plastic scintillator was chosen in order to provide fast signals for the first level trigger. Due to the low atomic mass of plastic scintillator, the forward detector is not well suited for reconstruction of gammas. The forward detector has been structured in several detector layers, which contain a window counter, a forward tracker, a thin scintillator hodoscope, a calorimeter, an additional thin scintillator hodoscope (FRI) and a downstream veto (FVH). Some of the properties of the FD are shown in Tab. 2.5.

scattering angle coverage	3^0-18^0
scattering angle resolution (tracker)	$< 0.2^0$ (FWHM)
hit time resolution [ns]	< 3 (FWHM)
amount of sensitive material [g/cm^2]	50
radiation lengths [g/cm^2]	≈ 1
nuclear interaction lengths	≈ 0.6
vacuum chamber window thickness [mm Al]	≈ 2
max kinetic energy for stopping (T_{stop} [MeV]): pion/proton/deuteron/alpha	170/300/400/900
energy resolution for stopped particles	$\approx 3\%$ (FWHM)
energy resolution for particles $T_{stop} < T < 2 \cdot T_{stop}$	$4 - 8 \%$ (FWHM)
particle identitfcation	ΔE–E
π^+/π^- separation	delayed signal technique

Table 2.5 *Properties of the Forward Detector*

Forward Window Counter - FWC
The forward window counter has been located directly in front of the scattering chamber and consists of twelve segments of 5mm thick plastic scintillator, inclined by 10^0. It provides the fast signal on the multiplicity of charged tracks in the first level trigger (fig. 2.6).

Forward Proportional Chamber – FPC
The forward proportional chamber placed behind the FWC allows the precise angular reconstruction of charged particles. It consists of two modules with four layers of drift tubes. One layer has 122 individual straws and each second layer of straws is shifted by the radius of the tube in order not to leave gaps between individual straws. The modules are rotated by 90 degrees with respect to each other to allow for a two dimensional hit reconstruction (Fig. 2.6).

Forward Hodoscope – FHD

The next detector downstream of the FPC is the forward hodoscope. It consists of three layers of 5 mm thick plastic scintillator. The first two layers have 24 elements each. These were shaped in the form of Archimedian spirals with opposite direction. The third layer was shaped in the form of 48 pie elements. The overlap of all three layers creates 1104 hit pixels with resolution (FWHM) 1.2^0 in polar and 4.6^0 in azimuthal angle (Fig. 2.7).

The fast logic signal from FHD is used in the first level trigger, usually in coincidence with the FWC or/and FRH. Analog information from the third layer of FHD could be used in the analysis together with information from the FRH in the ΔE-E method for charged particle identification.
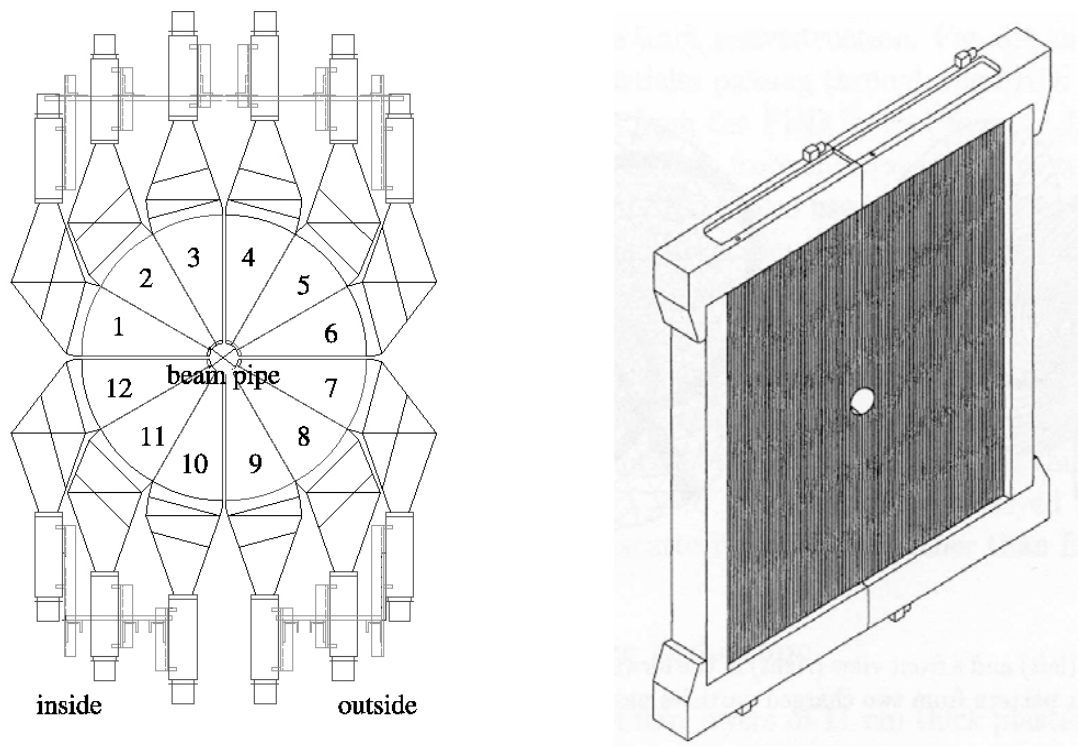

Figure 2.6 *The scheme of the Forward Window Counter (left). One module of the Forward Proportional Chamber (right).*

Forward Range Hodoscope – FRH

Behind the FTH, the forward calorimeter FRH has been located. It consists of four layers of 11 cm thick plastic scintillators, subdivided into 24 pie-shaped elements covering a polar angle of 15^0 (Fig. 2.8, left). The main purpose of the FRH is the measurement of the kinetic energy of charged particles. The division into four planes provides the energy deposit information, which can be used individually for one plane or as a sum over several planes in the particle identification utilizing the ΔE$-$E method. The logic signal from first or second layer of the FRH is used in the first level trigger.
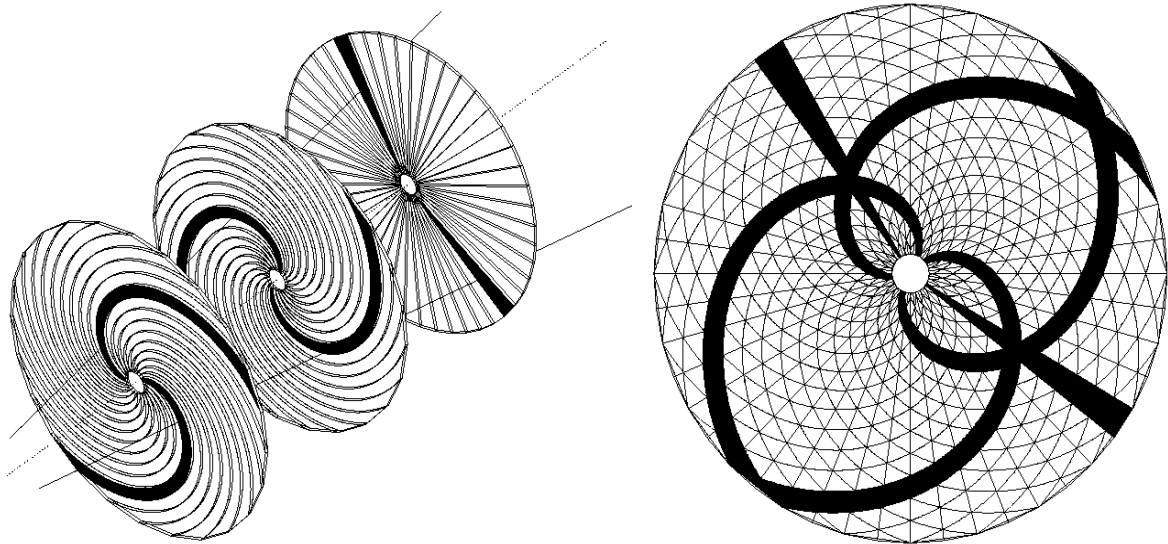
Figure 2.7 *The scheme of the Forward Hodoscope.*

Forward Range Intermediate Hodoscope – FRI

The FRI is an additional thin scintillator hodoscope located between the 3rd and 4th FRH layers. This detector provides the two-dimensional position sensitivity in conjunction with a fast time signal (Fig. 2.8, right). One of the FRI applications is the possibility to detect the angle of recoil protons from neutrons produced in the beam-target interaction.

More details about the FRI can be found in [16].

Forward Veto Hodoscope – FVH

The last detector layer of the FD is the Forward Veto Hodoscope. It was made out of 12 horizontal bars, 2 cm thick and 13.7 cm wide. Each bar was read out with photo multipliers on both sides in order to calculate the horizontal hit position by analyzing the time difference of signals from both ends of the bar (Fig. 2.9). The FVH serves as veto counter in the first level trigger logic for rejection of the FRH punching through particles.
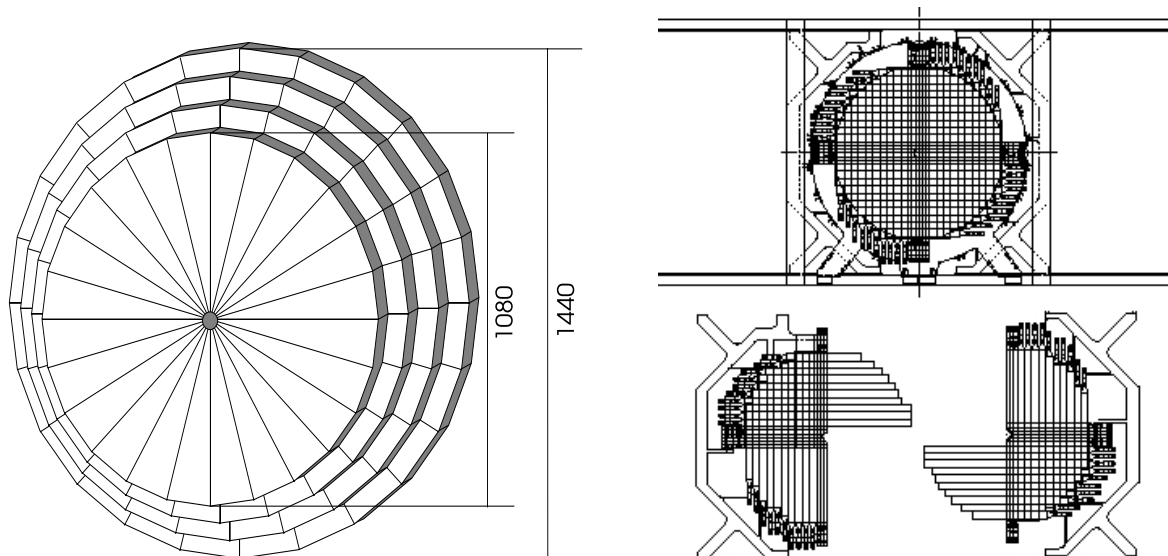
Figure 2.8 *The scheme of the Forward Range Hodoscope (left). The scheme of the Forward Range Intermediate Hodoscope (right)*
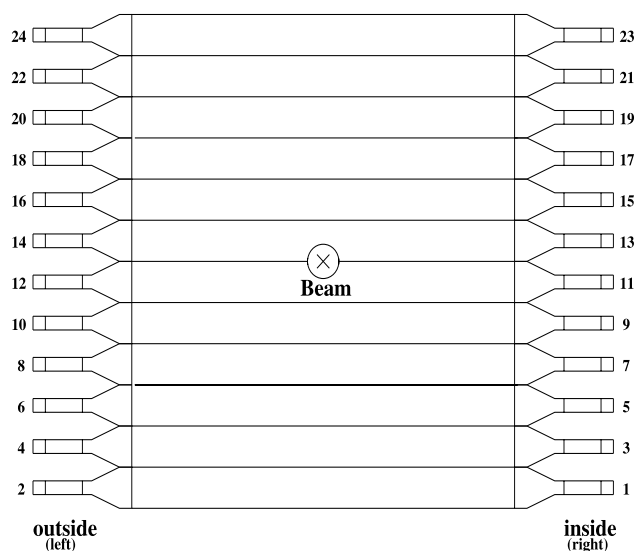

Figure 2.9 *The scheme of the Forward Veto Hodoscope.*

2.3 Trigger and data acquisition system

In the WASA experiment the total reaction rate was several million events/s at the design luminosity 10^{32} cm^{-2}s^{-1}. The front-end electronics comprised about 1500 ADC channels and 4000 TDC channels (multi-hit type), corresponding to an average event size of 2-3 kBytes. With the use of front-end electronics the maximum read-out rate was between 10 and 20 kHz. In order to suppress

background and to extract interesting events the sophisticated trigger system had to be used [17].

2.3.1 Readout system

The overall structure of the data acquisition system is shown in Fig. 2.10. The analog signals from all scintillator detectors are transmitted from the experimental hall to the electronics hut on RG58 cables. In specially built splitter-delay boxes the signals are divided into two branches. At one of them the signals are delayed by built-in 300 ns delay lines and then passed to Analog-to-Digital Converters (ADCs). The other branch was used for triggering and timing and is connected to discriminators. The signals from the discriminator are split for concurrent Time-to-Digital Conversion (TDC) and trigger building. Front-end digitizers for the WASA detector are read out by Fastbus Smart Crate Controllers developed in Fermilab. The data collected in the FASTBUS crates are distributed to the Data Acquisition System and monitoring stations via parallel data links.

2.3.2 Trigger system

The trigger system constantly monitors the signal in the detector and detects pre-defined "interesting" events. The triggers, used in this thesis, were based on detecting two charged particles in Forward Detector and a specific number of tracks in the Central Detector. For these selected cases, gate and strobe signals (Starts) are generated for the front-end digitizers and for the WASA Data Acquisition System, which starts the conversion process in the ADC and TDC modules. The trigger system could also deliver a "fast clear" signal, discarding further conversion in case when a second level trigger condition was not met.
The triggers are organized in two levels. The first level trigger decision is based on a set of hit multiplicity and coincidence conditions from signals produced by the plastic scintillator. The processing time of the first level trigger is about 100 ns and intended for triggering the Data Acquisition System and producing control signals for the front-end electronics. The number of incident particles per reaction could not be directly determined from the number of hits. Electromagnetic shower and nuclear reactions induced in the detector and the surrounding material by the incident particles could give parasitic hits. The background is further reduced by putting certain thresholds on the total energy deposited or cluster multiplicity in SEC into the second level trigger. If no valid second level condition was received, a "fast clear" was sent to the front-end modules. After a "fast clear" all data digitizers recovered within 1 μs.
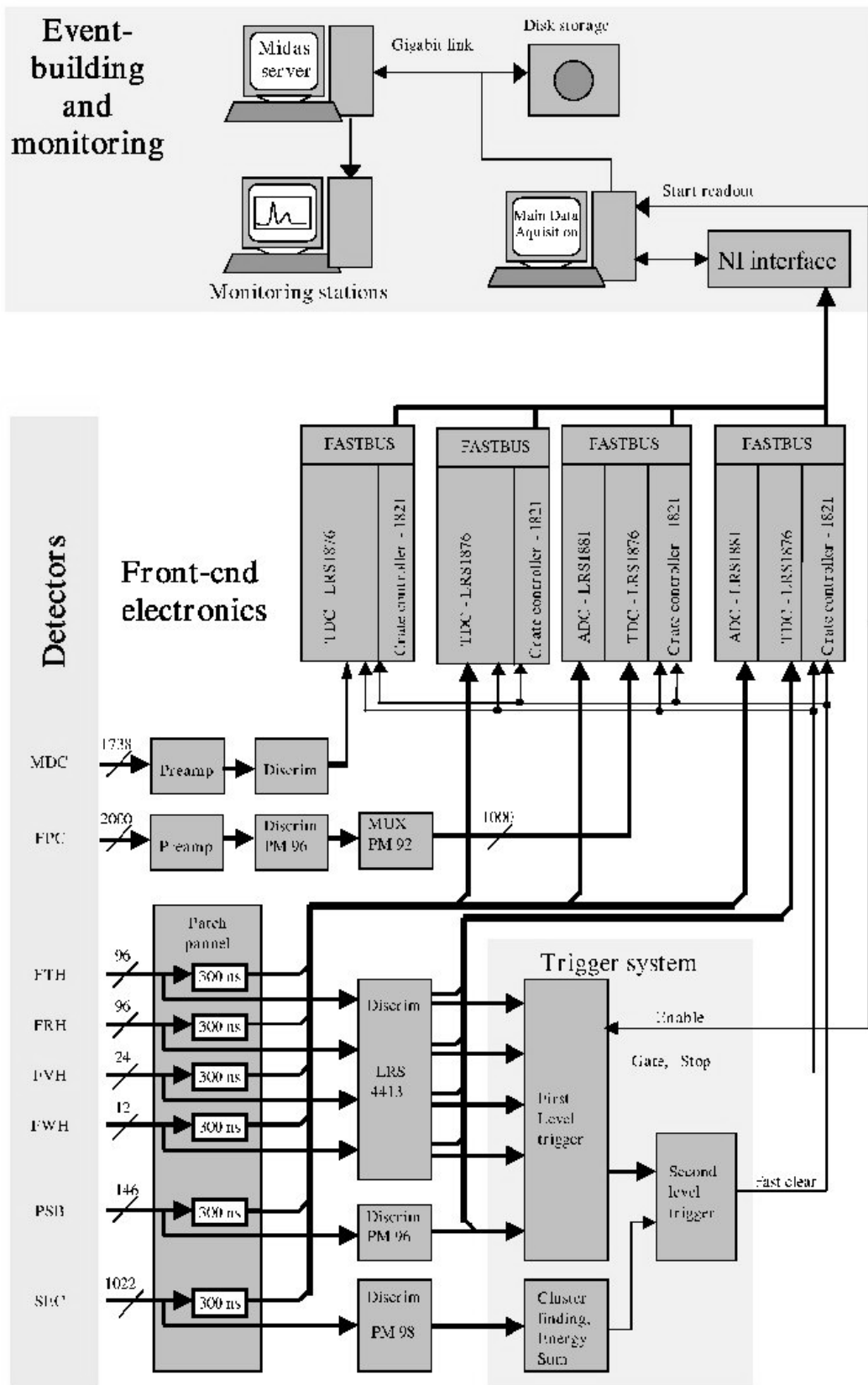
Figure 2.10 *The scheme of the readout system*

3 Analysis

3.1 Analysis tool

The general structure of the analysis package is shown in Fig. 3.1. In order to get corrections for detector acceptance and efficiency both experimental data and Monte Carlo simulations have to be reconstructed, selected and analyzed in the same way.

3.1.1 Event generator – GIN

The event generator GIN is based on the program FOWL [21] from the CERN program library and produces events according to phase space. As output GIN delivers the momentum vector at the interaction point for each outgoing particle and an individual weight factor for each event. This weight is kept through the whole procedure of detector simulation and event analysis. The user can simulate a resonance production mechanism by modifying the phase space weight according to production dynamics. GIN allows also making fast simplified estimations of the detector acceptance providing the possibility to set geometrical cuts for different kind of particles.

3.1.2 Detector simulation – WMC

The detector simulation program WMC is based on the GEANT3 package [22] from CERN, in which one uses Monte Carlo techniques to simulate the detector response for incident particles. In GEANT3 the detector setup has to be described in detail by a set of geometrical volumes, filled by an appropriate material. Both active (e.g. scintillators) and passive (e.g. superconducting solenoid) materials have to be defined in WMC. Passive volumes do not give signals, however influence the particle tracks. The user defines the reaction vertex position, which can be shifted in all space directions, and WMC reads the information about the laboratory momentum of the generated GIN events. The tracking routines simulate the particle passing through the detector volumes in small steps. For each step, using known cross sections, the routines calculate the probability of energy loss, multiple scattering, particle decay and different secondary interactions. If a reaction occurs, energy and direction of the reaction products are calculated. The procedure is repeated until all primary and secondary particles, produced in the detector material, either left the detector volume or lose all energy or decay or will be absorbed. Finally the energy and time information for detector elements are saved in a format, which is similar to that of the experimental data and later, can be analyzed with the same reconstruction program. In addition, WMC output data contain the original particle momentum

and vertex bank with the true information about the event. This true information can be used to test the reconstruction efficiency and the detector resolution.

3.1.3 Event reconstruction – W4PREC

The event reconstruction program W4PREC is used for decoding and reconstructing experimental and simulated data. At the beginning the information regarding the detector, beam time and control parameters for processing are read in.

The W4PREC procedure starts from decoding the hardware address of hit to a detector element number. Then each ADC information is corrected for pedestals and each TDC is corrected for time offsets. The ADC information is translated to deposited energy and the TDC information is converted to time. Hits with ADC or TDC information outside allowed regions are removed. After the hits are combined into clusters and the clusters are combined into tracks, particles and events are identified. The user can define, how many hits should occur in each detector part in order to accept a track as a 'good' one. Finally the selected events are written on disc as four-vectors for the subsequent physical analysis. In addition to the data file the W4PREC program creates also a set of histograms of different kinematical variables.

3.1.4 Kinematical fit – KFIT

The KFIT program was developed to test the hypothesis that the reconstructed event belongs to a given reaction channel by checking energy and momentum conservation, and then to improve the kinematical variables of all measured and unmeasured particles. The method, applied in the calculations, is a least-squares fit with constraints for energy-momentum conservation and additional constraints for invariant masses of selected groups of particles (when checking the hypothesis of resonance decay) [23].
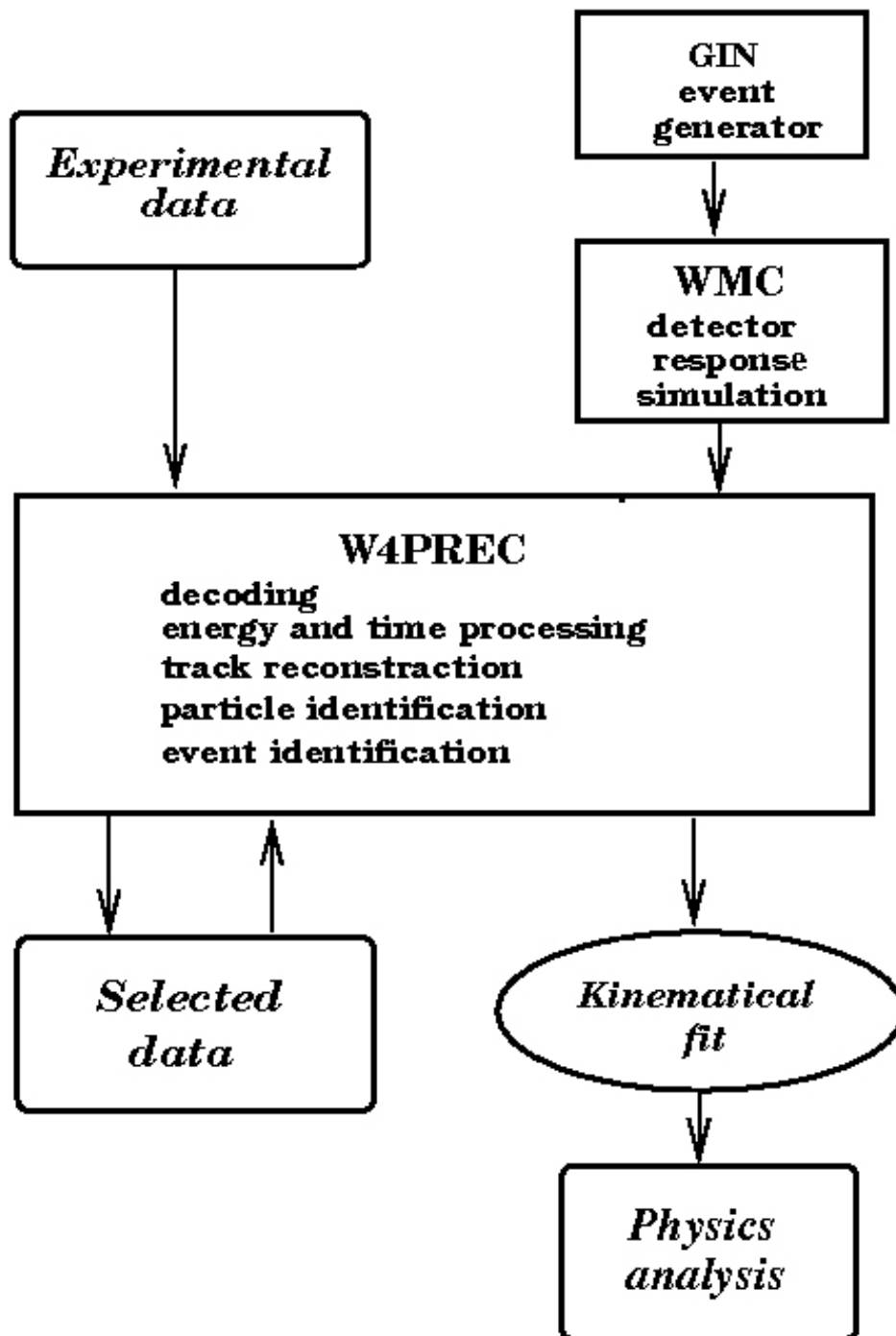
Figure 3.1 *Flow chart of the offline data analysis procedure*

3.2 Reconstruction and calibration

3.2.1 Track reconstruction

There are several procedures of track reconstruction developed for different parts of the WASA detector. In the FD the track reconstruction routine consists of three steps:

• first - hits in each detector plane are combined into a hit cluster. The merging into the cluster is done by checking the neighboring elements of the hit element and (optionally) the hits time difference. The geometrical size and allowed time window can be defined by the user. The integral energy deposit and the mean time of the cluster are calculated.

• Then clusters in different detector planes are merged into a detector track. Again the geometrical overlaps of the clusters and time differences are checked.

• Finally, the tracks in separate detectors are combined into one track. The track reconstruction procedure combines the all found hits into track candidates, so some tracks can consist of only one hit.

The deposited energy of a track is the sum of all cluster energies. The FD track time is the cluster time in the first hit plane after the vertex. The track direction in FD for charged tracks is given by FPC hit coordinates with respect to the assumed vertex. If FPC hits are missing, then the FHD defines the track direction [18]. The track direction for neutral tracks is defined by the coordinate of the first hit in FRH with respect to the assumed vertex.

As a first step for the track reconstruction in CD the routine looks for the element with the maximum energy deposit, which is not included in the cluster yet and searches in a square pattern of 3x3 elements for neighbouring elements having a non-zero value of deposited energy. If such an element is found, its time is checked. If the hit time is inside the defined time window, this element is added to the cluster and the routine looks around this new element inside the square pattern. The procedure is repeated until no new neighbouring elements with energy deposited are found. Finally the deposited energy of all elements in the cluster is added up and the cluster time and coordinates are calculated as mean value of all added elements weighted by their energy deposition [20].

The track reconstruction in MDC consists of two parts: pattern recognition and full fitting [15]. As a last step the routine tries to combine MDC tracks with hits in PSB and tracks in SEC using the space and optionally for PSB time information. For charged CD tracks having the MDC information the kinetic energy can be reconstructed from the energy deposited in CsI crystals and from the momentum measured in the MDC. The track direction is defined by the MDC track parameters. For charged tracks not having the MDC information as well as for neutral CD tracks the kinetic energy can be reconstructed only from the deposited energy in the crystals and the track direction is calculated from the cluster coordinate with respect to the assumed vertex. The CD track time is defined by either the PSB hit time or the cluster time, if the PSB information is absent.

After reconstruction all tracks can be classified by:

• FDC Forward charged tracks, which have at least one hit in FHD or FPC,

• FDN Forward neutral tracks, which do not have a hit neither in FHD not in FPC, but have hit at least one layer of the FRH,

• CDC Central charged tracks, which have PSB or MDC information and

• CDN Central neutral tracks, which do not have hit neither in PSB not in MDC, but have at least one hit in the calorimeter.

In the beginning of the event reconstruction all charged and neutral tracks are checked for 'event' time: this means that track time has to belong to some time window around the fastest track time. This fastest track usually is chosen among the FDC tracks and has the time closest to the trigger time. The time window is defined from experimental data and could be different for neutral and charged tracks (for example, the time of charged FD tracks are defined by a hit in the fast FHD layer and the time of neutral FD tracks correspond to time of the slower hit in FRH) and for different detectors (Fig. 3.2). Even for the same detector the time window may be shifted for events collected by different triggers. This checking was especially necessary for neutral tracks in CD. Due to longer collection time in CD the real data could have hits and clusters with a time beyond the event time. For example, the neutral tracks multiplicity in CD at beam energy 0.895 GeV could reach up to 10, but at this energy one can produce at most two π^0, producing only four gammas. After time checking the neutral tracks multiplicity usually was reduced to 4-5 tracks.
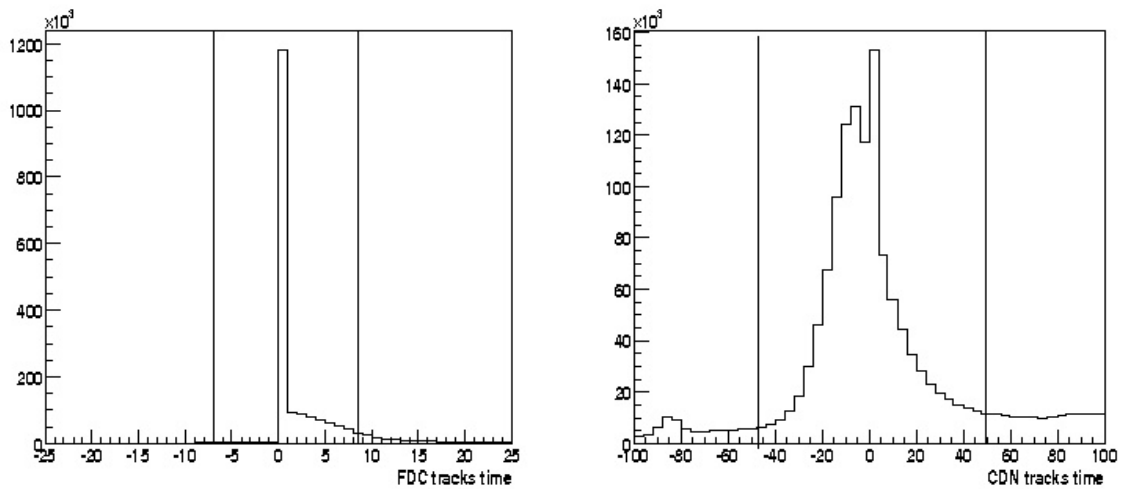

Figure 3.2 *Time [in ns] of charged tracks in FD (left) and neutral tracks in CD (right). Horizontal black lines show the time window used for selection.*

3.2.2 Detector calibration

The measured experimental data consist of sets of digital ADC and TDC information for the different detector elements. The ADC information has to be

translated to corresponding deposited energy. For the scintillator elements this translation from the ADC content in channels to the deposited energy is described by a function, parameterized by a set of calibration constants. For different types of detectors one uses different parameterized functions and different methods for finding calibration constants. The calibration procedure has to take into account the non-linear response of the detector, which can be due to:

• non-uniformity of the light output, when the light output depends on the position of the energy deposition;

• quenching, when the light output depends also on the particle type and its energy;

• nonlinearities, when photo multiplier tube (PMT) can give non linear response for large light input.

Calibration of the FD

The calibration of the forward detector initially was done using data from elastically scattered protons. The proton energy and scattering angle are correlated and therefore the ADC information from experiment can be compared with the deposited energy information from Monte Carlo (MC) simulations at the same beam energy.

In order to obtain non-uniformity values the detector elements are divided into several radial bins and for each bin the measured deposited energy from high-energy punched through protons was compared with MC data. The high-energy protons have almost constant differential energy loss, independent of the scattering angle. In this case the deposited energy should be the same through one detector element. The non-uniformity correction factors have to describe the angular dependence of the calibration.

In order to extract the nonlinearity of PMT one usually takes data from one π^0 or two π^0 production events with non-relativistic protons. The experimental data from several proton energies, already corrected for non-uniformity, are combined in ΔE-E plots for different layers of the FRH [18]. The relative difference between measured and MC data is extracted and a linear function is adjusted to the data to get an energy-dependent calibration function. The effects due to quenching are taken from the literature and were included in data analysis [19].

Calibration of the CsI detectors

The initial calibration of the CsI detectors was done with cosmic muons. These approximate calibration constants serve as starting values for an iterative procedure, in which the photons from the $pp \rightarrow pp\pi^0\pi^0$ reaction are used. In this method for each photon shower the crystal with the maximum deposited energy is found. Then the mass of the π^0 meson is calculated from the energy and opening angle of the photons. Since the crystal with the maximum energy deposition has the main contribution in the π^0 mass, its calibration constants are improved by changing them so that the invariant-mass peak from several events becomes centered at the position expected from the MC. The tuning of the CsI calibration constants is done for each run period [20].

Calibration of the PSB

The calibration of the PSB was done with elastically scattered protons, for which energy and scattering angle are exactly correlated. The detector is divided into angular bins and for each bin the measured ADC spectrum is compared with the expected from the MC one [15].

Calibration of the Mini Drift Chamber

The application of MDC in the experiment is based on the possibility to determine the charged particle position from the drift time of electrons, which are produced by an ionizing particle in a gas-filled chamber. This drift time measurement can be used for the calculations of the drift distance (the minimal distance from the anode wire to the particle trajectory). The MDC calibration procedure is described in detail in [15]. Drift time spectra for each layer are obtained after the calibration. These spectra serve as a basis for the calculation of the time-distance function, which connects the measured drift time with the shortest track-to-wire distance.

3.3 Identification and selection

The next important step in the event reconstruction is the particle identification. The accuracy in the particle identification and energy reconstruction defines how well one can separate the explored reaction from possible background applying invariant and missing mass cuts. The information about the mass is especially needed in cases, when one particle of an event was reconstructed from the four-momentum of the other particles.

3.3.2 Particle identification in Central Detector

In the central detector the information from MDC, PSB and CsI was used for the charged particle identification. After track reconstruction in MDC one can get information about the momentum of a charged particle. Comparing the deposited energy in CsI or PSB to the particle momentum one can reasonably well separate the protons from pions. Alternatively, one can create also a ΔE-E plot for particle identification in CD using the information from the thin PSB scintillator and from the calorimeter. Fig. 3.3, 3.4 and 3.5 show examples of particle identification in CD. Since in the present work only protons and positively charged pions had to be identified, only positive momenta are presented in the plots.

Neutral pions were identified by the proper invariant mass of two neutral tracks, which were assumed to be caused by photons (Fig.3.6, right).
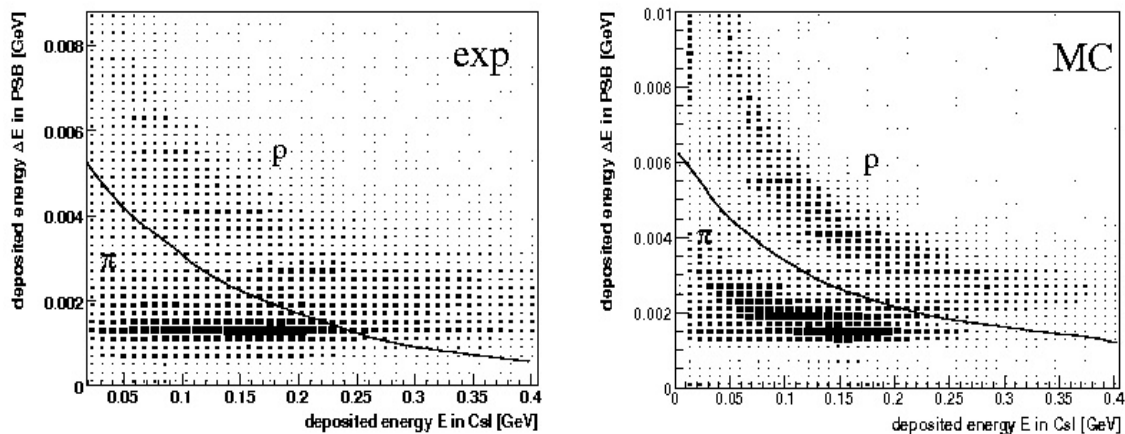
Figure 3.3 *Deposited energy in CsI crystals versus deposited energy in PSB. Particles below the black line were identified as pions, the ones above this line as protons. Left: experimental data, right: MC.*
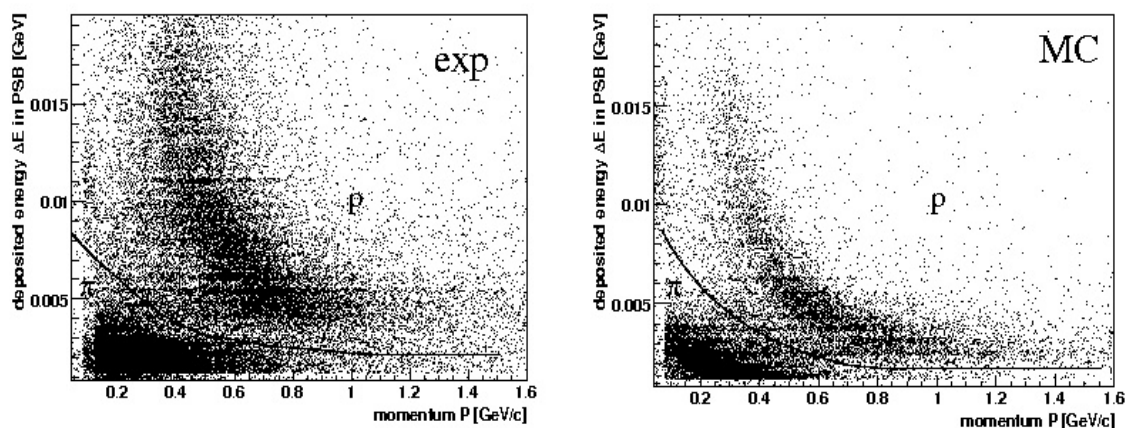

Figure 3.4 *Momentum from MDC versus deposited energy in PSB. Particles below the black line were identified as pions, the ones above as protons. Left: experimental data, the right: MC.*
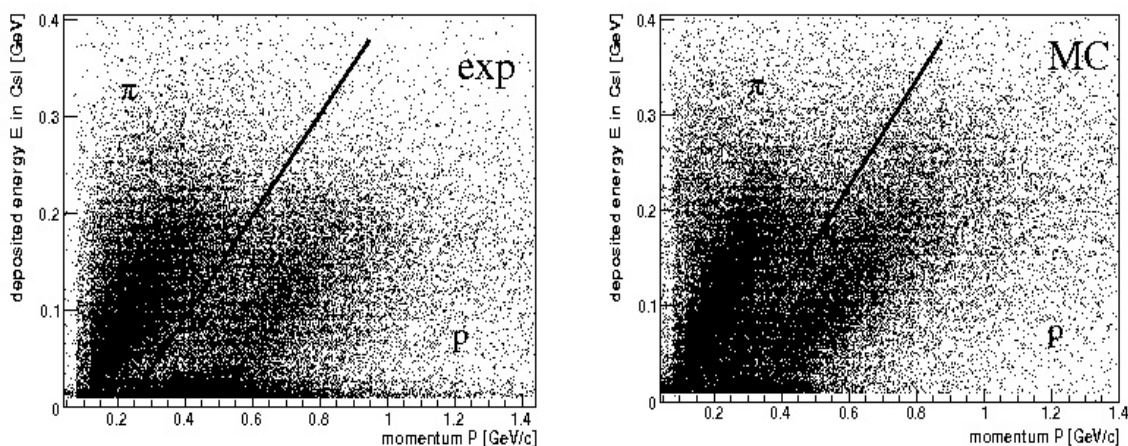

Figure 3.5 *Momentum from MDC versus deposited energy in CsI crystals. Particles right of the black line were identified as protons, the ones on the left side as pions. Left: experimental data, right: MC.*

3.3.1 Particle identification in the Forward Detector

For FD charged particle identifications the information from FRH and FHD have been used: the deposited energy in all FRH planes has been compared with the energy deposited in the third thin FHD plane, which consists of straight elements having the best performance. Also the energy deposited in one FRH plane has been compared with the deposited energy in neighboring planes. This method is based on the specific ionization energy loss per unit length described by the Bethe-Bloch formula. For velocities lower than $0.96 * c$ the energy loss behavior is usually different for different particles. As an example in Fig 3.6 (left) exhibits a ΔE-E plot, which was used for proton identification in FD. Neutral particles in FD were identified in this work as follows: any neutral track is assumed to be a neutron. Later on this hypothesis is checked by the kinematical fit.
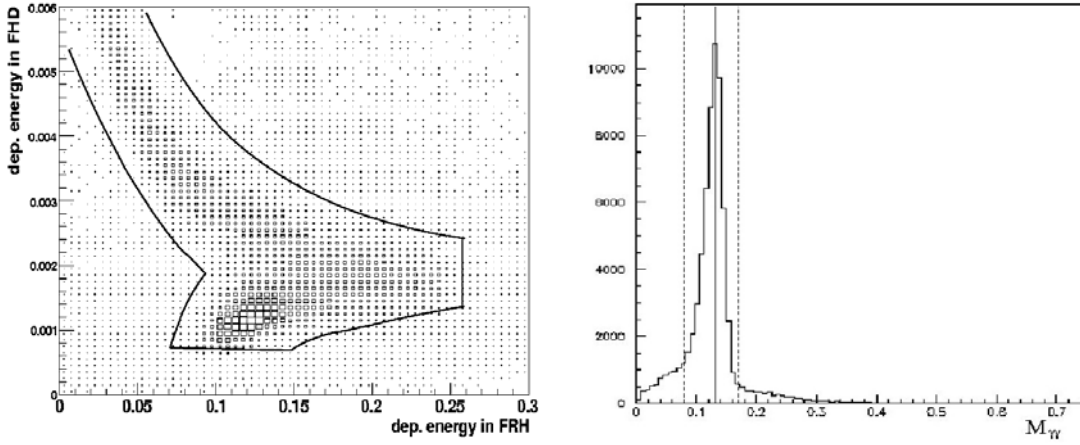

Figure 3.6 *Left: ΔE-E plot - deposited energy in the FRH versus the deposited energy in FHD. The particles lying inside the black contour line were identified as protons. Right: invariant mass $M_{\gamma\gamma}$ of two photons in CD. Vertical solid line shows the $M_{\gamma\gamma} = M_{\pi^0} = 0.135$ GeV, the vertical dashed lines show the invariant mass limits for π^0 selection.*

3.3.3 Selection of pp→ppπ⁰π⁰ events

The reconstruction of $pp{\rightarrow}pp\pi^0\pi^0$ events was the main aim of the presented work. Two triggers were used for $\pi^0\pi^0$ event selection: cluster and energy triggers. Both triggers required two charged particles in FD and no charged ones in CD. The cluster trigger demanded in addition two or more neutral clusters in CD and the energy trigger established a threshold for the energy deposited in the calorimeter. There were several reasons for selecting two charged tracks in FD as well as neutral ones in CD:

Due to kinematics for energies up to 0.9 GeV most protons fly into the FD. With increasing beam energy protons increasingly fly also into larger angles, but even at a beam energy of 1.3 GeV the two-proton acceptance in FD is still about 55%. Furthermore, there are two problems with CD, which made it almost senseless to select one rescattered proton in FD and another one in CD: the first problem is connected with a low efficiency of the first CD layer. This layer was excluded from triggering, so all events with one proton in the angular range from 20^0 to 25^0 should be lost.

Secondly, due to the specific MDC construction there was a decreasing MDC efficiency in the forward part of CD (the first five inner layers were cut to fit the rescattering chamber). The forward part of CD covers the angle range from 20^0 to 40^0, which are exactly the angles, where protons from the $\pi^0\pi^0$ production should be registered in CD.

Gammas from π^0 decay fly in any direction. The probability to have all four gammas in CD is about 60% (Fig. 3.7). The plastic FD has low photon registration efficiency and hence was not used as photon detector.

The total geometrical acceptance for such a selection is then 0.41 at beam energy 0.775 GeV decreasing to 0.17 at 1.3 GeV. Another reason, why protons were selected in FD and gammas in CD, was the fact, that FD was tuned to register fast charged particles and CD was tuned to register gammas. The main background reaction, which could satisfy the trigger demands, was $pp{\rightarrow}pp\pi^0$. This reaction has approximately a 10^3 times bigger cross section than the $\pi\pi$ production reaction. To remove this background in the offline analysis exactly four neutral tracks in CD, which were assumed to be gammas, have been required. This simple condition has reduced the contribution from one π^0 production by a factor of more than 10^4.

As a next step one futher condition was applied: four gammas had to give two pions in the invariant mass. For four gammas there are six possible gamma combinations for one π^0 and there are only three not crossing gamma pairs for two π^0. The pair combination, which had minimum distance from the point (135 MeV, 135 MeV) in the two dimensional invariant mass plot was chosen as the right one (Fig.3.8, left). Only if this distance was less that 35 MeV, the event was accepted.

Two charged tracks in FD had to be identified as protons using the ΔE-E method. This selection gives already a rather clean sample. In addition the cuts on the total kinetic energy of all particles, cuts on the two protons and one pion missing mass and cuts on the two proton missing mass were applied in order to remove the background as much as possible and to select properly reconstructed events (Fig.3.8, right).
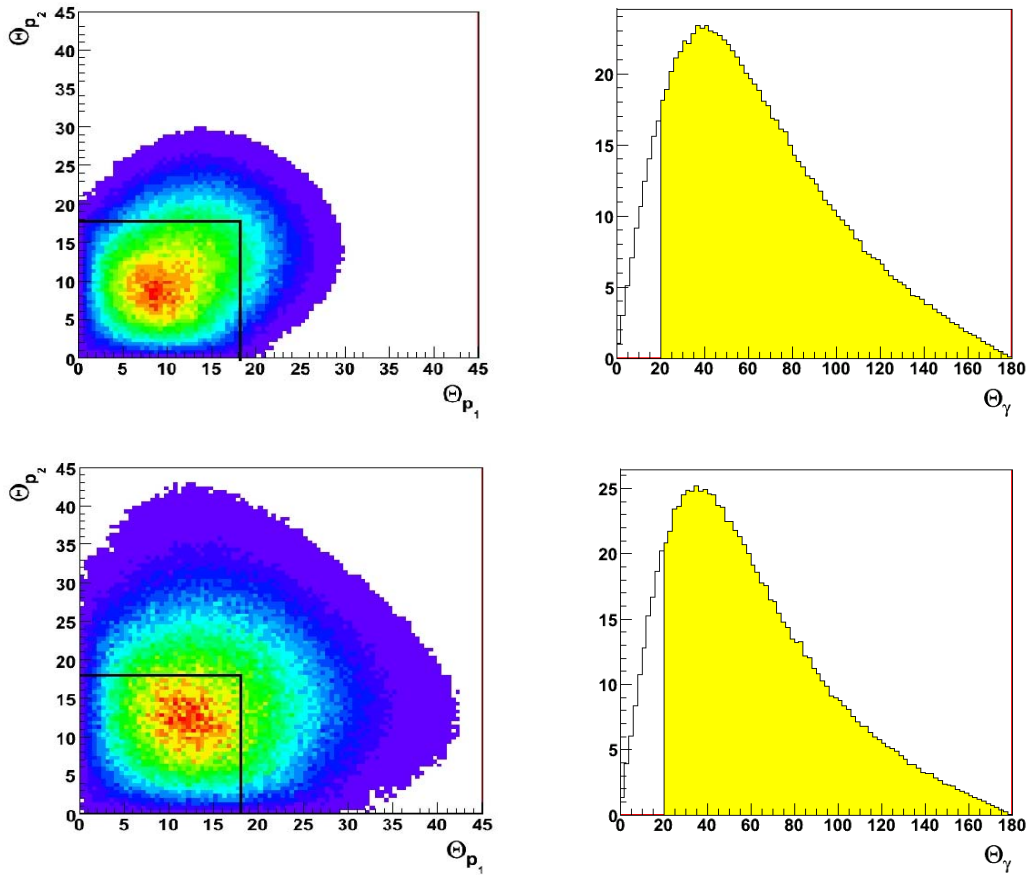
Figure 3.7 *Plots of the phase space simulation of the pp→ppπ⁰π⁰ reaction. Left:
the azimuthal angle* Θ_{p_1} *of one proton versus the azimuthal angle* Θ_{p_2} *of the
second one in the laboratory system. Black lines mark the FD geometrical
acceptance. Right: the azimuthal angle* Θ_γ *of gammas from* $2\pi^0$ *decay in the
laboratory system. The yellow area shows the CD geometrical acceptance. Top
row is for beam energy of 0.775 GeV and bottom one is for beam energy of 1.1
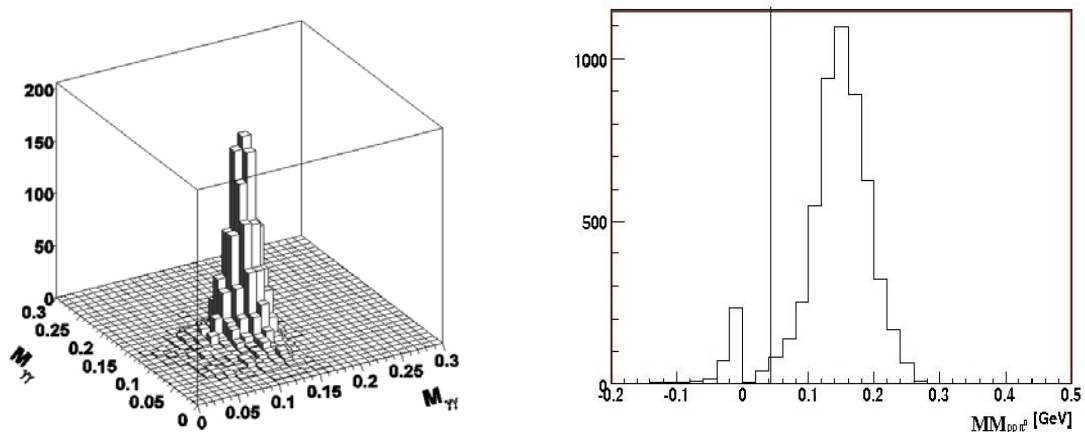GeV.*

Figure 3.8 *Left: invariant mass of one gamma pair versus the other at T_p=0.775
GeV. Right: missing mass* $M_{pp\pi^0}$ *. The vertical solid line shows the minimum
missing mass value allowed for selected events.*

3.3.4 Selection of pp→ppπ^0 events

Since this reaction could be selected with the same triggers as the $\pi^0\pi^0$ production reaction, we decided to use the known $pp{\to}pp\pi^0$ total cross section for normalization of the $pp\pi^0\pi^0$ cross section. That way we could avoid the problem of trigger efficiency.

In addition, we obtained that the $pp{\to}pp\pi^0$ reaction measured at a beam energy 0.895 GeV can be rather well described by only the Δ^+ excitation. Thus this reaction, collected with two different triggers, could be used to understand the energy trigger behavior and to find the algorithm to simulate it properly.

This reaction was selected as two protons and no neutral tracks in FD together with two gammas and no charged tracks in CD. Two gammas had to give a invariant mass in the range from 0.09 to 0.165 GeV. With such a selection the $pp{\to}pp\pi^0$ reaction at beam energies of 0.9 GeV and higher has less than 8% of events with two protons in FD, but the rather big cross section (~4mb) accompanied with almost no background at such a selection have allowed us to collect sufficiently good statistics. The cuts for $M_{p\pi}$ and $M_{\pi\pi}$ missing masses were applied to select events properly reconstructed in energy.

3.3.5 Selection of pp→pnπ$^+$ events

Originally this reaction has been chosen to check the efficiency of the neutron registration in FD. In order to favour the kinematics with neutrons flying in forward direction, the pions and protons were selected in CD. The choice of having one charged particle registered in the forward part of CD (CDF) and another one in the central part (CDC) has been preferential for the kinematics with two charged particles in CD (Fig. 3.9). This choice totally coincided with the elastic trigger demand, hence we have used this trigger for the selection.

The reactions $pp{\to}pp_{el}$ and $pp{\to}pp\pi^0$ were selected by the elastic trigger simultaneously with the reaction $pp{\to}pn\pi^+$ as background. Since all three reactions have similar cross sections, the number of events selected by the elastic trigger mainly depends on the reaction kinematics. For estimations we have assumed that the registration efficiency for FD, CD charged particles and for CD neutral ones is close to unity. The efficiency estimated from MC gammas registration in FD [24] was obtained as 0.5. As shown in Tab. 3.1, the $pp{\to}pn\pi^+$ reaction has the largest geometrical acceptance with respect to the background reactions for the selection with one charged particle in CDF and one in CDC.

In the offline analysis additional requirements has been applied: only events having no neutral tracks in CD were selected. This requirement has reduced practically totally the contribution from the $pp{\to}pp\pi^0$ reactions. To separate protons and pions in CD the information from MDC, deposited energy in PSB and CsI crystals were used. In the selected events protons and pions must

correspond to the proper particle type in all three identification methods (Fig. 3.3-3.5). In spite of the such rather strong selection criteria the accepted events have had some admixture from the $pp{\rightarrow}pp_{el}$ reaction (Fig. 3.10). These misidentified events have been removed using the correlations in opening and planarity angles between two charged particles. In case of the $pp{\rightarrow}pp_{el}$ events this correlation is strongly located at the opening angle of about 90^0 and the planarity angle of about 180^0.

Later, during the reconstruction of the $pp{\rightarrow}pn\pi^+$ reaction we have realized that this channel is particular suitable for studying the Roper excitation, for extracting its properties from the decay $N^*{\rightarrow}n\pi^+$ (see chapter 4.2.2).

To cover a larger kinematical phase space we have expanded the selection conditions: we have used again two charged tracks in CD, but now additionally also one charged in FD and one charged in CD. No hard requirements for neutral tracks have been applied for both choices: either no single neutral track, or a single one in any detector, but with angle not more than 55^0 with respect to the beam axis (kinematical limit for neutron angle at beam energy 1.3 GeV). In both cases we have used elastic trigger for the selection, since the requirements established by this trigger gave the maximum number of selected $pp{\rightarrow}pn\pi^+$ events. We have not tried to select the protons in FD and pions in CDF since without use of MDC we could not reconstruct the pion energy and with use of MDC this choice has not given a real increase in the statistics due to the low MDC efficiency in this detector part.
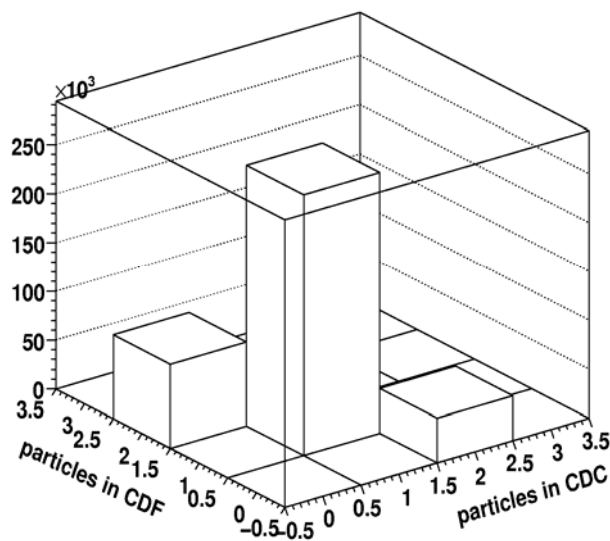

Figure 3.9 *Number of charged particles in the central part of CD (CDC) versus number of particles in the forward part of CD (CDF) in the reaction pp→pnπ⁺, when proton and pion from MC data are registered in CD.*

For events selected as two charged particles in CD we demanded the presence of the information in the MDC, PSB and the calorimeter for each track. Having protons and pions in CD, especially in the forward part of CD where both protons

and pions mostly punch through, the MDC information was necessary for energy reconstruction.
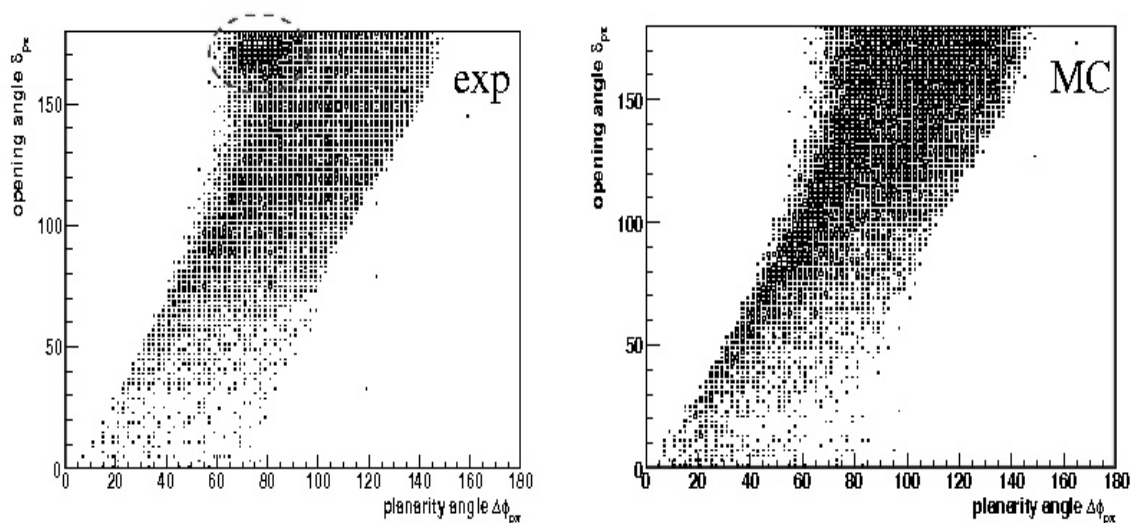

Figure 3.10 *Opening angle between the proton and pion versus planarity angle in laboratory system. Left: selected experimental data, where the dashed line marks the enhancement corresponding to pp_{el} events. Right: MC data of the $pp \rightarrow pn\pi^+$ reaction.*

selection conditions	$pp \rightarrow pn\pi^+$	$pp \rightarrow pp_{el}$	$pp \rightarrow pp\pi^0$
1CDF, 1CDC	0.26	0.06	0.08
1CDF, 1CDC, 0CDN	0.13	0.06	< 0.001
1CDF, 1CDC, 0/1 neutral track with azimuth. angle $< 55^0$	0.26	0.06	0.012
1FDC, 1CDC	0.28	0.64	0.15
1FDC, 1CDC, 0/1 neutral track with azimuth. angle $< 55^0$	0.28	0.64	0.017

Table 3.1 *Geometrical acceptance for different selection conditions. CDF is charged track in forward part of CD, CDC – charged track in central part of CD, FDC – charged track in FD, FDN – neutral track in FD.*

For events selected as one charged particle in FD and one charged in CD the reaction $pp \rightarrow pp_{el}$ has become the dominant part (Tab. 3.1).

We have not used the MDC information for identification, since in this time period the MDC gas system and reconstruction procedure was not adjusted properly, so the MDC has had a low efficiency. For the discussed beam time the real MDC efficiency was three times worse than obtained by the MC data. The requirement to have information in MDC has decreased the statistics by one order of magnitude in comparison to the selection without MDC. And with a big contribution from pp_{el} we could lose all advantages from the new selection

because of the modest final collected statistics. In this sample pp_{el} events were recognized by their clear signature in the angular correlations. For particle identification the information in PSB and calorimeter was used (ΔE-E method).

3.3.6 Selection of $pp{\rightarrow}nn\pi^+\pi^+$ events

With this reaction we first intended to check the possibility to observe Bose-Einstein correlations (BEC) in the case where two identical bosons ($\pi^+\pi^+$) were produced in the final state. The $pp{\rightarrow}nn\pi^+\pi^+$ reaction has been selected at a beam energy of 1.1 GeV.

This reaction is difficult to reconstruct, since for neutrons one can only approximately reconstruct the angle and energy by registering the angle and energy of the rescattering proton. Furthermore, one can easily include some garbage neutral hits from secondary interactions as a possible signal from neutrons. Nevertheless, there is one clear signature, which can be used for selection - these are two π^+ in the final state.

We could not use FD for pion identification since at a beam energy 1.1 GeV only 3% of the events had both pions flying in FD and among them only a quarter of the events had both pions stopped in FD. The pions had to stop in FD to be identified by the delayed pulse method. The fast punch through pions give almost the same signals in FD planes as fast protons. So protons from the reaction $pp{\rightarrow}pp\pi^0$ could be easily misidentified as pions.

Thus we have decided to select only events with two charged particles in central part of CD (CDC). At such azimutal angles neither pp_{el} nor $pp\pi^0$ can contribute by kinematics. Only $pp{\rightarrow}pn\pi^+$ events remain as a significant and dangerous background. To reduce the contribution from the $pp{\rightarrow}pn\pi^+$ reaction we used the trigger, which demanded, except for two charged tracks in CDC, also two segments in FD with a deposited energy higher than some threshold. By MC estimations this requirement could decrease the background from the $pp{\rightarrow}pn\pi^+$ by more than 100 times. The information from MDC, PSB, and calorimeter was used for particle identification in CD.

Since neutral tracks in FD do have neither FPC information nor hits in FHD the polar and azimutal angles of neutral tracks are known only with big uncertainty. Therefore we used the information from FRI for the angle reconstruction, if a track had hits in this detector.

3.4 Triggers

In the experiments described in this work, two different kinds of triggers were used for selection of $\pi^0\pi^0$ production events: cluster and energy trigger. Both triggers were organized in two levels. The first level trigger got the signal from

the fast plastic FHD scintillator and started the data acquisition system [15]. The second level trigger got an additional signal from the slower CD detector. This additional cluster multiplicity or deposited energy sum requirement helped to reduce the background events contribution.

The first level triggers were identical in case of cluster and energy ones and required two hits in FWH and two hits in first FRH plan. But the second level set different conditions: the cluster trigger required a coincidence between one/or more clusters in the first seven layers of CD and one/or more clusters in the next seven layers. The energy trigger established a threshold for a total deposited energy in the calorimeter.

Three different energy triggers were installed during the experiment: the first one set the threshold for the energy sum in the central part of CD, the second one set the threshold for the energy sum in the forward part of CD, and in addition, there was the trigger which set the threshold for the combined energy sum signal from forward and central parts. The last trigger had to compensate the possible loss of events which have not had enough energy to satisfy the first or second trigger. The main physical background collected with these triggers should have been from single π^0 production.

For the selection of $nn\pi^+\pi^+$ production events we have used the segment energy trigger, which has required two hits in the central PSB and two segments in FRH with deposited energy higher than some threshold. The segment was created by the four following detector elements (of the four FRH plans), which are aligned at identical azimutal angle range. There were 24 such segments in FRH.

3.4.1 Trigger simulation

Since one of the trigger aims is to reduce background contributions as much as possible, the trigger requirements can cut also some part of the desired events. To simulate the trigger behavior correctly in MC it is very important to understand their action on the data.

The cluster trigger was simulated in MC by the requirement of two charged tracks in FD and by the coincidence of at least one gamma from π^0 decay registered in the first seven layers of CD with at least one gamma in the next seven layers. No additional threshold conditions for the cluster energy have been included in the cluster trigger for the experiment.

In case of the energy trigger the requirements for FD were the same in MC - two charged tracks. To simulate the trigger behavior in CD first one needed to define the energy threshold from experimental data. In Fig. 3.11 (left) the experimental energy sum distribution is shown. The data were collected with a trigger for the threshold in the central part of CD, only hits in a 'good' time window were summed. The experimental distribution shows no threshold in the summed energy.

One needs to remember that in reality the energy threshold in the trigger is represented by a threshold in voltage, which was applied to the sum of signals from photomultipliers tubes (PMT)

There is no possibility in the trigger to compensate for variations in the gain of individual PMT. The only way is to try to adjust the high voltage so that they produce as much as possible an equal signal for the same deposited energy. Some work along this task was done, but still some variations were left [26].

Furthermore, because the time gate for information collection is rather long for CD, the real data have had 'garbage' hits, i.e. hits which were out of the event time but contributed to the energy sum. Due to these reasons the experimental distribution for the energy sum in CD has not had a clear threshold. The Fig. 3.11 (right) shows the sum energy distribution for all hits registered in the CD independently of the time. The data were collected with trigger for the threshold in central part of CD. In this distribution a smooth threshold between 1600 and 2300 channels can be observed. One can assume that in the case, when all hits are included in the energy sum, only a variation in the gain of the PMT could wash out the threshold. When in the energy sum only hits with good time were included, selected data become sensitive to contribution from 'garbage' hits in the total energy.
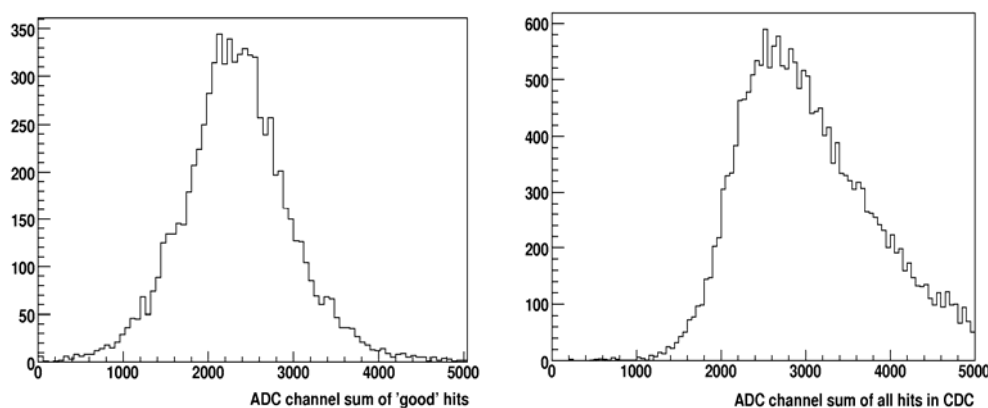

Figure 3.11 Left: *ADC channel sum of hits with 'good' time in CDC. Right: ADC channel sum of all hits in CDC. Data were collected with the energy trigger applied for CDC at beam energy 1 GeV.*

To understand the triggers behavior selected events have been analyzed separately for each energy trigger.

We made the following assumption: if the deposited energy from "good" hits is higher than some value A_{sum}^{ch}, the conditions for passing the threshold does not depend any more on the contribution from 'garbage' hits. These events have to be registered and this means, that the right side of the channel sum distribution for "good" hits has to coincide with the MC sum distribution.

One possible solution to select the MC and experimental data in the same way (to introduce properly the trigger requirement and to exclude the background contribution) was to cut the events in MC and in experimental data with the energy sum less than A_{sum}^{ch}. But such a solution had two main disadvantages: first,

the loss in statistics and second, the additional cut reduced the detector acceptance and made the data more sensitive to the model corrections.

To reproduce the trigger threshold, which has been smeared by 'garbage' hits we tried to correct MC data by introducing an additional weight for events with channel sum less than A_{sum}^{ch}. The trigger simulation procedure for one trigger has consisted from four steps:

• First, hit energy information for MC data was transferred from eV to channels using calibration constants. Channel sum distributions for MC and real data were created (Fig. 3.12 (left)).

• Second, MC data were normalized at the right side of channel sum distribution to coincide with the experimental one (Fig. 3.12 (middle)).

• Then, the additional weight was calculated by dividing the experimental distribution by the MC one. For events with channel sum more than A_{sum}^{ch} this weight was equal to unity (Fig. 3.12 (right)).

• The last step consisted of the multiplication of the MC data by this weight.

For the energy trigger in the central part of CD only the channel sum in the central detector was used for the calculation of the additional MC weight.
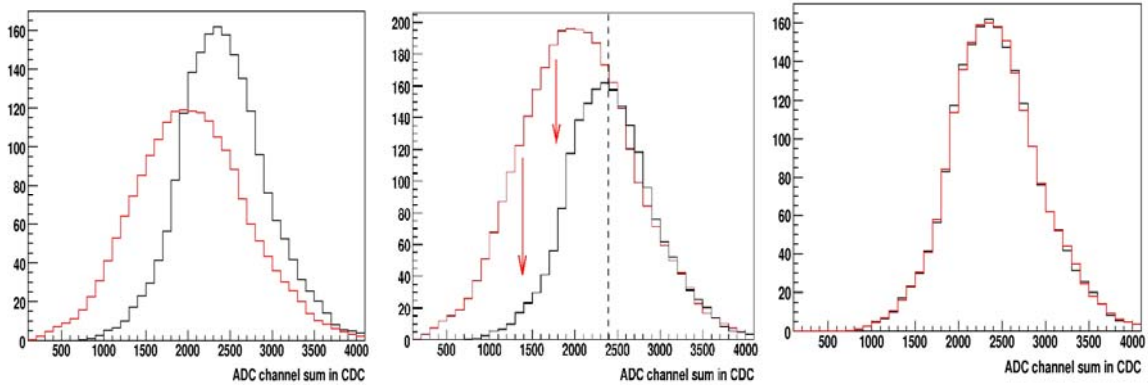

Figure 3.12 *Left: the ADC channel sum in the central part of CD for MC (red histogram) and real data (black histogram), normalized to the same number; Middle: the same channel sums, but MC distribution is normalized in such a way that the right distribution side coincides with the right side of the experimental distribution; Right: the channel sums after correction of MC by the calculated weights.*

Correspondingly for the energy trigger in the forward part of CD the channel sum in the forward part was used. For the combined trigger a special cut in the two-dimensional plot for channel sum in central and forward parts was applied (Fig. 3.14). It was assumed that the threshold in one part of CD could not influence the other one in the sense that the trigger did not insert any additional threshold for tracks in another detector part. This can be seen in fig. 3.13, where the channel sums in the forward part of CD for MC and real data, collected by central part energy trigger, are presented. Fig. 3.13 (left) shows the original channel sums and in Fig. 3.13 (right) that MC data were corrected by weight calculated from channels sums in the central part of CD.
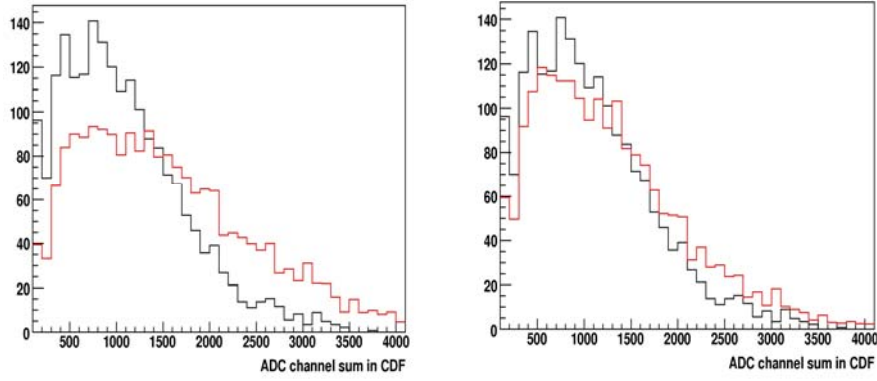
Figure 3.13 *Left: the ADC channel sums in the forward part of CD for MC (red histogram) and real data (black histogram). Right: the same channel sum, but MC distribution corrected by a weight calculated from the channel sum in central part.*
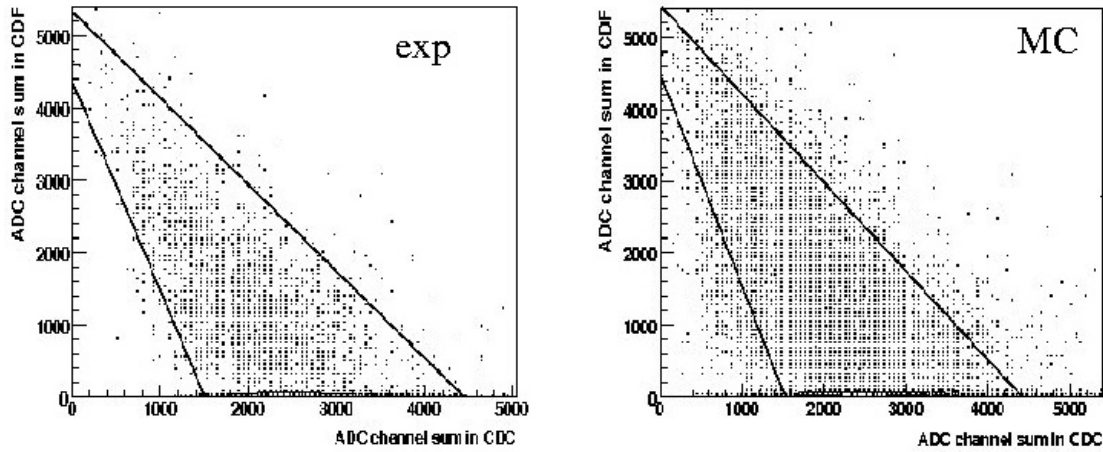

Figure 3.14 *ADC channel sum in CDC versus ADC channel sum in FCD. Left: experimental data collected by the combined trigger; Right: MC data. Solid lines show the applied cuts.*

The events selected by the energy trigger in the central part of CD were divided by two sub-samples: the events with gammas only in the central part and events with gammas in the full CD. It is obvious, that events with all gammas in central part of CD were less sensitive to the garbage hit contribution. These two sub samples were analyzed separately.

After correction for acceptance and efficiency the data were collected in one sample as weighted average with weights inversely proportional to the squared errors obtained after corrections.

To check the correctness of the above-described trigger simulation method we compared the data for the $pp{\rightarrow}pp\pi^0$ reaction collected with two different triggers: cluster and energy trigger.

The $pp{\rightarrow}pp\pi^0$ events obtained with cluster trigger were reasonably described by the phemenologycal model including the Δ^+ excitation as a main π^0 production mechanism (see Appendix I).

After acceptance and efficiency corrections the $pp \rightarrow pp\pi^0$ data selected with energy trigger showed good agreement with data obtained with cluster trigger (Fig. 3.15).

For the $nn\pi^+\pi^+$ events selection we used the energy segment trigger, which established the threshold for deposited energy in FD segments and required at least two segments with deposited energy higher than some threshold. Simultaneously, this trigger demanded two charged tracks in the central part of CD. One segment consisted of four subsequent elements from different planes of FRH, lying in the same range of polar angle. To simulate the trigger behavior the FRH has been divided into 24 segments. For each segment the energy sum threshold was defined from experimental data as the sum of deposited energies in each segment element. This threshold has changed from 0.032 up to 0.04 GeV (Fig 3.16). In MC only events with two charged tracks in central part of CD and with at least two segments with deposited sum energy higher that this threshold have been selected.
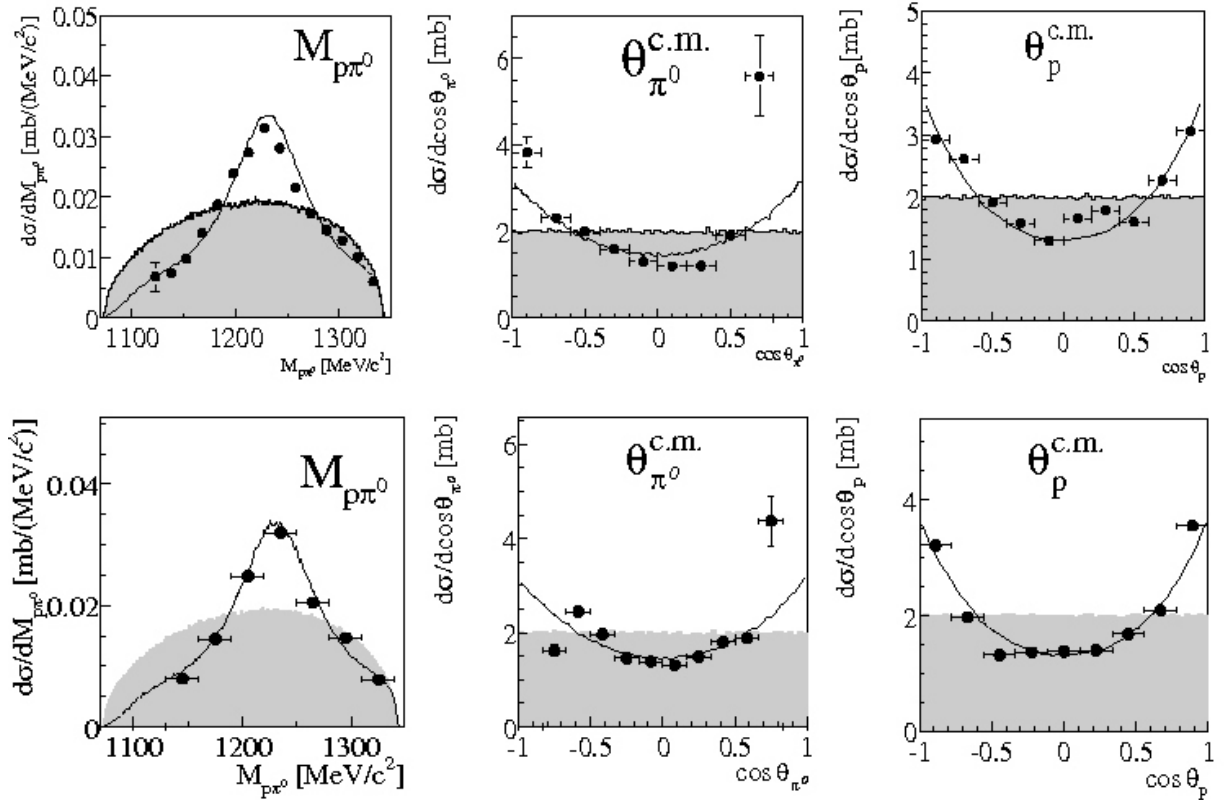

Figure 3.15 *Invariant mass* $M_{p\pi^0}$ *and polar angles of* π^0 *and protons in cm system at* T_p=0.895 GeV. *Top row is the* $pp \rightarrow pp\pi^0$ *data collected with the cluster trigger; bottom one is the* $pp \rightarrow pp\pi^0$ *data collected with the energy trigger. Solid lines are calculations for the phemenologycal model (6.1) (Appendix I).*
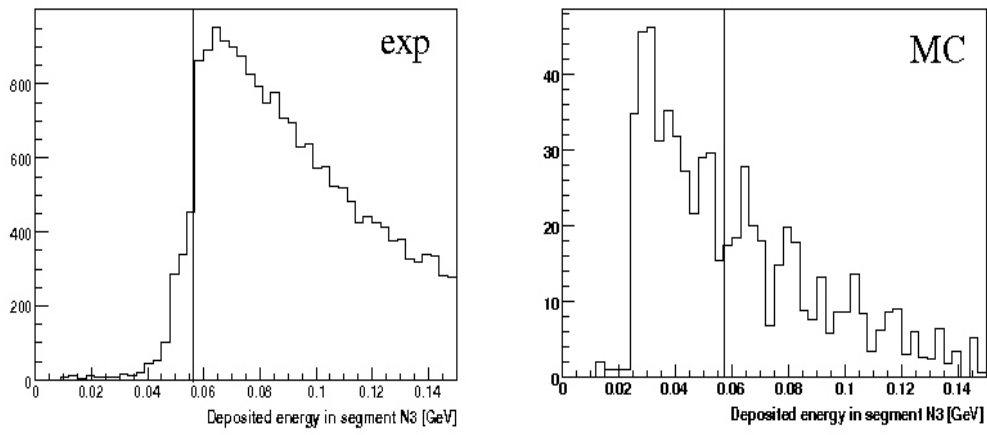
Figure 3.16 *The deposited energy in the third FD segment. Left is data collected by the energy segment trigger, right is MC data. Solid lines show the threshold deposited energy value for the event selection.*

4 Results and discussions

4.1 Integral cross sections

The integral cross section (σ) can be calculated by:

$$\sigma = \frac{N_{\exp} \cdot f_{prescaling}}{\int Ldt \cdot \varepsilon_{acc} \cdot \varepsilon_{dac} \cdot \varepsilon_{trig}} \qquad\qquad 4.1$$

where $N_{\exp}$ is the number reconstructed events, $f_{prescaling}$ is the pre-scaling factor, which was used to reduce trigger rate due to limited readout rate of the DAQ. $\int Ldt$ denotes integrated beam luminosity, ε_{acc} is the detector acceptance and efficiency, ε_{trig} is the trigger efficiency and ε_{dac} is the data acquisition life time. ε_{acc} is usually obtained from the comparison of MC data generated for full solid angle and the same MC data passed through the detector and then selected and reconstructed with same criteria as a real data. ε_{trig} can be estimated as the ratio of events collected with selected trigger to the events selected without any trigger. In order to calculate the integrated luminosity usually one measures as reference a well-known reaction, for example $pp{\to}pp_{el}$. Since the reference reaction is measured simultaneously at the same beam time, the value of $\int Ldt \cdot \varepsilon_{dac}$ can be thus determined.

For beam energies of 0.775, 0.895 and 1 GeV the reaction $pp{\to}pp\pi^{0}$ was chosen as reference in order to avoid in addition an explicit determination of ε_{trig} by use of the same trigger. For the same reason at the beam energy of 1.3 GeV the $pp{\to}pp\eta$ reaction was used. For the beam energies 1.1 and 1.2 GeV the reaction $pp{\to}pp_{el}$ was used for the determination of $\int Ldt \cdot \varepsilon_{dac}$.

The total error in cross section is composed of statistical and systematic errors, where the statistical one is given by the inverse square root of the event number and the systematic error includes contributions from errors in the luminosity, in the calculated detector acceptance and in the trigger efficiency. The systematic error in the detector acceptance is due to the fact that different models give different energy and angle particle distributions, according to the production mechanism, thus the number of reconstructed events can change after applied cuts for different models. This error slightly increases with energy from 0.8% at beam energy of 0.775 GeV up to 2% at 1.3 GeV. The error in the trigger efficiency was estimated to be 4% and the error in luminosity, when reactions $pp{\to}pp\pi^{0}$ and $pp{\to}pp\eta$ were used for calculations, mostly was given by the known uncertainties of about 10% in the total reference cross sections [26, 27]. The error in the $pp{\to}pp_{el}$ cross section has been estimated to be about 4 % from the data presented in SAID database.

The cross sections obtained in the present work are given in Tab. 4.1 for the reaction $pp{\rightarrow}pp\pi^0\pi^0$ and for the reaction $pp{\rightarrow}nn\pi^+\pi^+$ in Tab. 4.2

energy [GeV]	cross section [μb]	error [μb]
0.775	1.62	± 0.04(stat) ± 0.17
0.895	9.1	± 0.2(stat) ± 1.0
1.0	19.0	± 0.3(stat) ± 2.0
1.1	28.0	± 0.4(stat) ± 3.0
1.2	32.0	± 0.3(stat) ± 3.5
1.3	102.0	± 0.7(stat) ± 11.2

Table 4.1 *The total cross section for the reaction $pp{\rightarrow}pp\pi^0\pi^0$*

energy [GeV]	cross section [μb]	error [μb]
1.1	34.0	± 3.2(stat)± 2.3

Table 4.2 *The total cross section for the reaction $pp{\rightarrow}nn\pi^+\pi^+$*

4.2 pp → ppπ⁰π⁰ reaction

The $\pi^0\pi^0$ production measurements and analyses constitute a natural continuation of the $pp{\rightarrow}pp\pi^+\pi^-$ investigations started at PROMICE/WASA. Since the $\pi^0\pi^0$ are identical bosons, only even angular momenta are allowed between them and therefore also the isospin of the pair can only be $I = 0$ or 2. At low energy the contribution from the isotensor part should be small due to the lack of appropriate resonance contributions and the $\pi^0\pi^0$ system should predominantly be scalar-isoscalar. In this case the reaction $pp{\rightarrow}pp\pi^0\pi^0$ could be in particular suitable to investigate the dominant contribution from the Roper excitation in the $(\pi\pi)_{I=0}$ production [8].

Furthermore, $\pi^0\pi^0$ production reactions have been measured at seven incident energies from 0.775 GeV to 1.3 GeV. These data allow to check systematically the Valencia model prediction for reaction mechanisms over a wide energy range.

Since at low incident energies the $\pi^+\pi^-$ data have been successfully described by the Roper ansatz based on the assumption that the Roper resonance excitation and its decay are the main reaction mechanism [5], we have tried at first to compare the obtained $\pi^0\pi^0$ data with the Roper ansatz predictions. As in the case of $\pi^+\pi^-$ production the Roper decay amplitude has the form

$$A \sim 1 + c\vec{k}_1 \cdot \vec{k}_2 (D_{\Delta^+} + D_{\Delta^+}) \qquad \qquad 4.2$$

In the full reaction amplitude this amplitude A has been complemented by the propagators for σ exchange and N^* excitation as well as by the expression for final state interaction (FSI) between two outgoing protons in relative s-wave. The constant 1 stands for the process $N^* \to N\sigma \to N\pi\pi$ and the scalar product $\vec{k}_1 \cdot \vec{k}_2$ of the pion momenta $\vec{k}_1$ and $\vec{k}_2$ in overall cm system describes the double p-wave decay of the route $N^* \to \Delta\pi \to N\pi\pi$. D_{Δ^+} defines the Δ^+ propagator. As in the previous analysis [5] the constant c, which gives the relative strength between two Roper decay routes, has been adjusted to the data at the lowest incident energy 0.775 GeV (appendix A). Simply by changing the incoming energy in the calculations, this Roper ansatz for $\pi^0\pi^0$ production describes almost all $\pi^0\pi^0$ spectra also at the beam energy of 0.895 GeV (appendix B).

However, at incident energies above 1.0 GeV we observe striking changes in the behavior of data. At energies around 1.0 - 1.1 GeV we expected still to find good agreement between data and Roper ansatz, since these energies correspond to the Roper excitation close to the pole position and only at energies above 1.2 GeV the $\Delta\Delta$ mechanism should take over. According to the Valencia model predictions this new reaction mechanism should be seen e.g. in $M_{\pi\pi}$ as a double-hump structure. On the contrary the experimental $M_{\pi\pi}$ spectra get close to phase space at incident energies above 1.0 GeV both in $\pi^0\pi^0$ and in $\pi^+\pi^-$ channels. Also the $M_{\pi^0\pi^0}$ spectra exhibit systematically a small low-mass enhancement due to pions which preferentially fly in parallel (Fig. 4.1). Furthermore, the $\pi^0\pi^0$ production total cross sections at energies up to 0.9 GeV agree rather well with the Valencia model predictions. But with further energy increase the data show more and more discrepancies to the calculations, attaining a maximum difference at the energies 1.1 - 1.2 GeV (Fig. 4.2). These drastic changes in the behavior of the data relative to the VM predictions separate the discussion of the data in two parts: two pion production at incident energies up to 1.0 GeV and above 1.0 GeV.

4.2.1 $\pi^0\pi^0$ production at T_p < 1.0 GeV

At energies close to threshold the data on the $pp\pi^0\pi^0$ channel show features, which basically are similar to those in the $\pi^+\pi^-$ channel as expected from isospin invariance, if $I = 1$ contributions to the latter channel are small. The $\pi^0\pi^0$ production at low energies has been compared with the Roper ansatz calculations step by step as it had been done in [5].

The not-flat proton angular distribution, which we obtained for $\pi^0\pi^0$ data, was described by including in the reaction amplitude the σ-exchange propagator with the same σ mass as in [5] (Fig. 4.3).
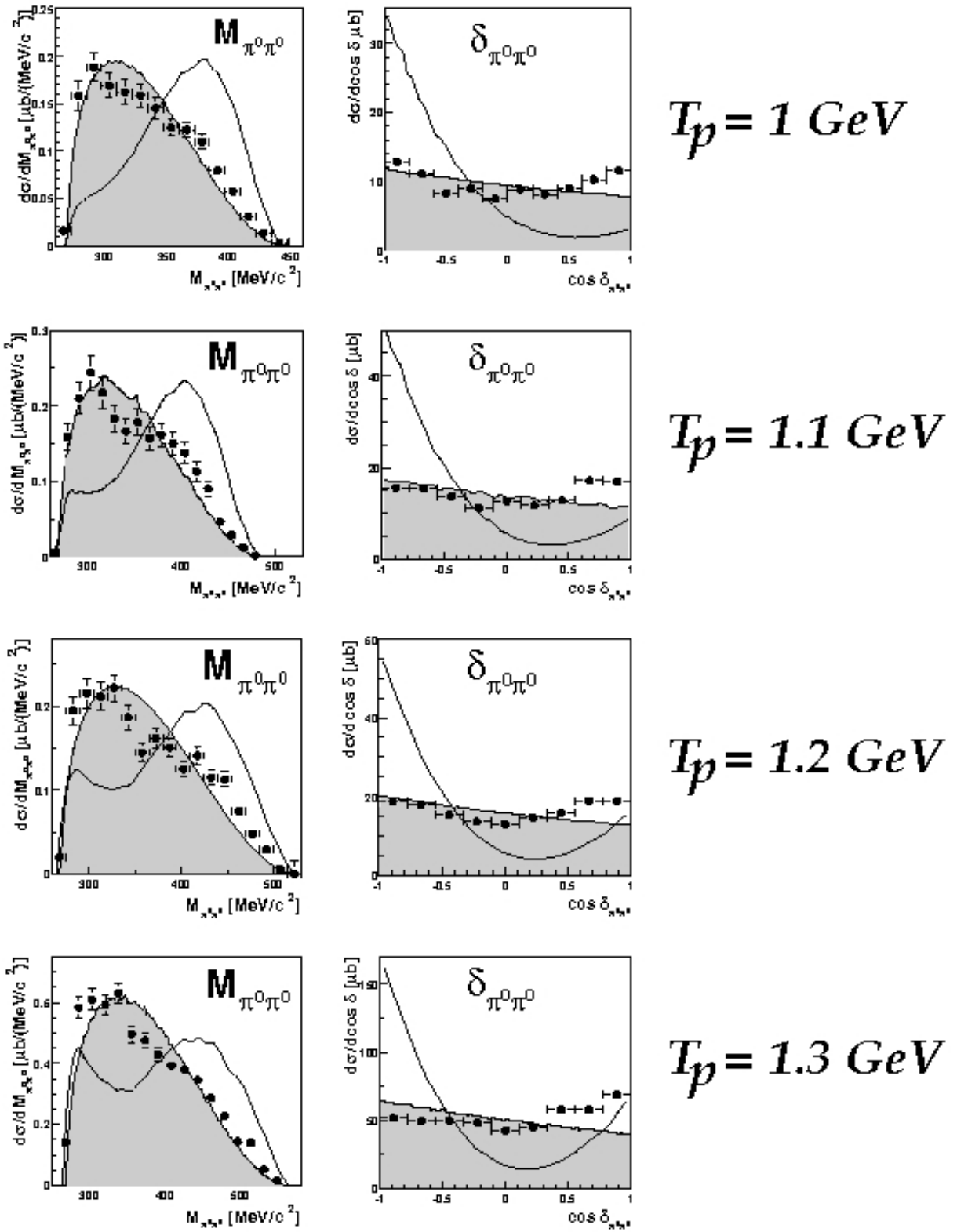
Figure 4.1 *Two pion invariant mass* $M_{\pi^0\pi^0}$ *and opening angle* $\delta_{\pi^0\pi^0}$ *between two pions of the* $pp \rightarrow pp\pi^0\pi^0$ *reaction at* T_p *1.0, 1.1, 1.2 and 1.3 GeV. Phase space is shown as grey area, solid lines are original VM calculations. The data are acceptance and efficiency corrected by the* $(\Delta\Delta)_{o+}$ *model (see chapter 4.2.3). All theoretical curves are normalized in area to the data.*
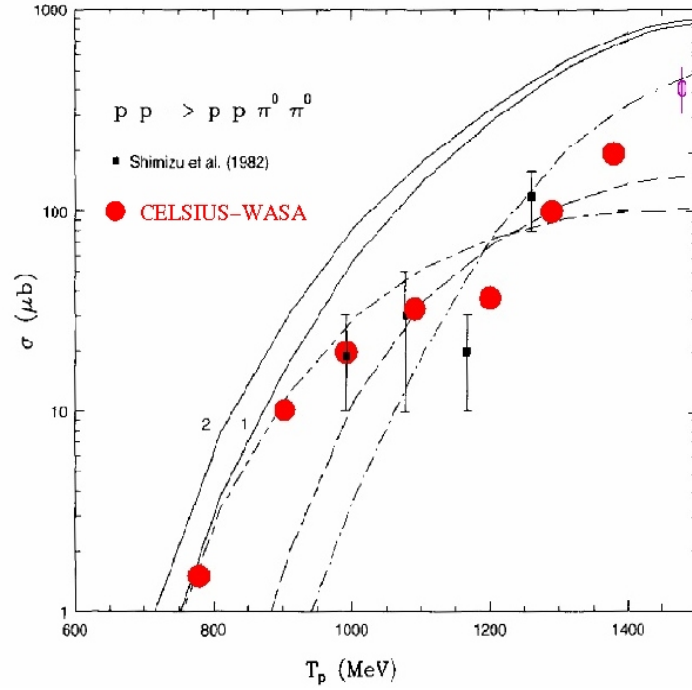
Figure 4.2 *Total cross section of the pp→ppπ⁰π⁰ reaction as a function of proton kinetic energy beam in the laboratory frame. The black lines are taken from [8]: solid covers are full calculations of the Valencia model for two different parameter sets, long-short-dashed line represents the decay $N^* \rightarrow N(\pi\pi)^{I=0}_{S-vawe}$; long-dashed line is the $N^* \rightarrow \Delta\pi$; dash-dotted line is the $\Delta\Delta$ excitation mechanisms; short-dashed line is a contribution of the non-resonant terms.*

T_p=775 MeV T_p=895 MeV
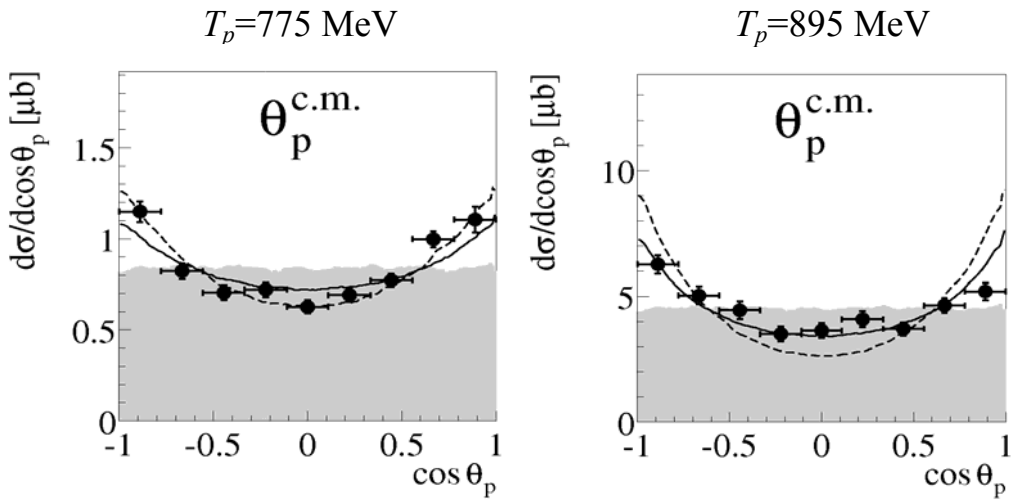
Fig. 4.3 *Distribution for the proton scattering angle in the overall cm system at T_p= 0.775 (left) and 0.895 GeV (right). The solid lines denote the Roper ansatz calculations with only σ exchange, the dashed ones the Valencia model calculations with σ and π-ρ exchanges. All theoretical curves are normalized in area to the data.*

The $\pi^+\pi^-$ analysis at near-threshold energies [5] showed that the data are strongly enhanced towards low proton-proton invariant masses. This behaviour has been explained by a strong proton-proton final state interaction (FSI). We find that the $\pi^0\pi^0$ data do not require such a strong FSI (Fig. 4.4). In the Watson-Migdal parametrisation for the proton-proton FSI [9] the size parameter R, which defines the interaction strength, is a single parameter adjusted to the $\pi\pi$ production data. In the case of the $\pi^+\pi^-$ data obtained at T_p=0.775 GeV its value was found to be $R_{\pi^+\pi^-}$ =2.75 fm. In the case of the $\pi^0\pi^0$ data at the same beam energy a value of $R_{\pi^0\pi^0}$ =3.5 fm is needed to describe the data.

In the framework of the Roper ansatz the most significant difference between the descriptions of the $\pi^+\pi^-$ and $\pi^0\pi^0$ channels consists in the value of the adjusted constant c in formula (4.2). This constant defines the strength of decay route $N^*\rightarrow\Delta\pi\rightarrow N\pi\pi$ relative to the Roper decay $N^*\rightarrow N\sigma\rightarrow N\pi\pi$. In the case of $\pi^0\pi^0$ production this constant c gives a twice weaker $N^*\rightarrow\Delta\pi$ decay contribution in the total reaction amplitude than has been found in [5] (Fig. 4.5).
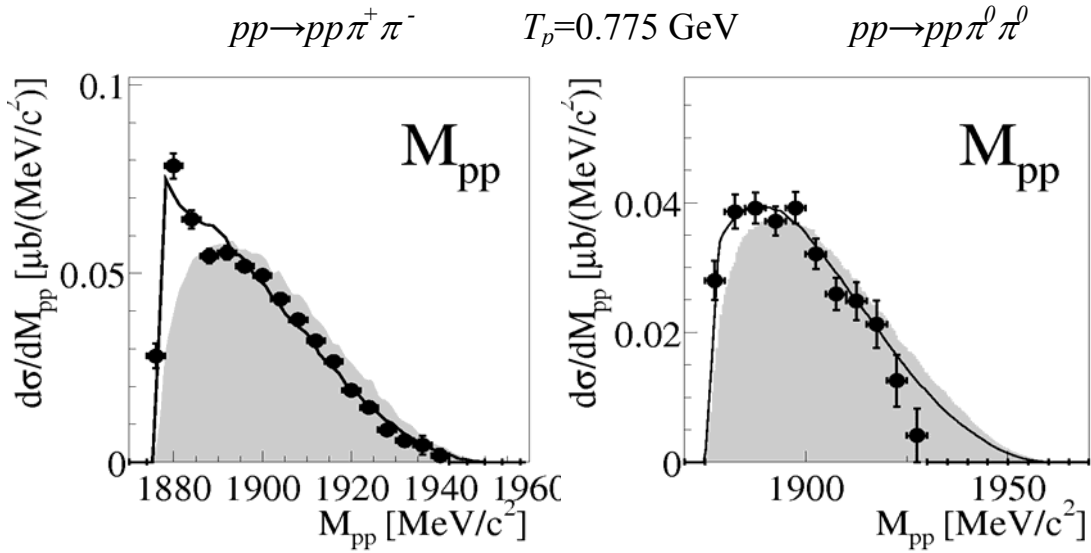

Figure 4.4 *Distribution of the invariant masses M_{pp} at T_p=0.775 GeV. Left: $\pi^+\pi^-$ channel, right: $\pi^0\pi^0$ channel. Black lines give Roper ansatz calculations with the FSI adjusted to data. The grey area denotes the phase space. All theoretical curves are normalized in area to the data.*

The invariant mass of two pions $M_{\pi\pi}$ and opening angle $\delta_{\pi\pi}$ are the most sensitive observables to the mixing of the two Roper decay routes. The opening angle between two pions $\delta_{\pi\pi}$ reflects the squared decay amplitude (4.2) averaged over all possible pion momenta at given opening angle $\delta_{\pi\pi}$:

$$\sigma(\delta_{\pi\pi}) \sim (1 + a\cos\delta_{\pi\pi})^2 \qquad\qquad 4.3$$
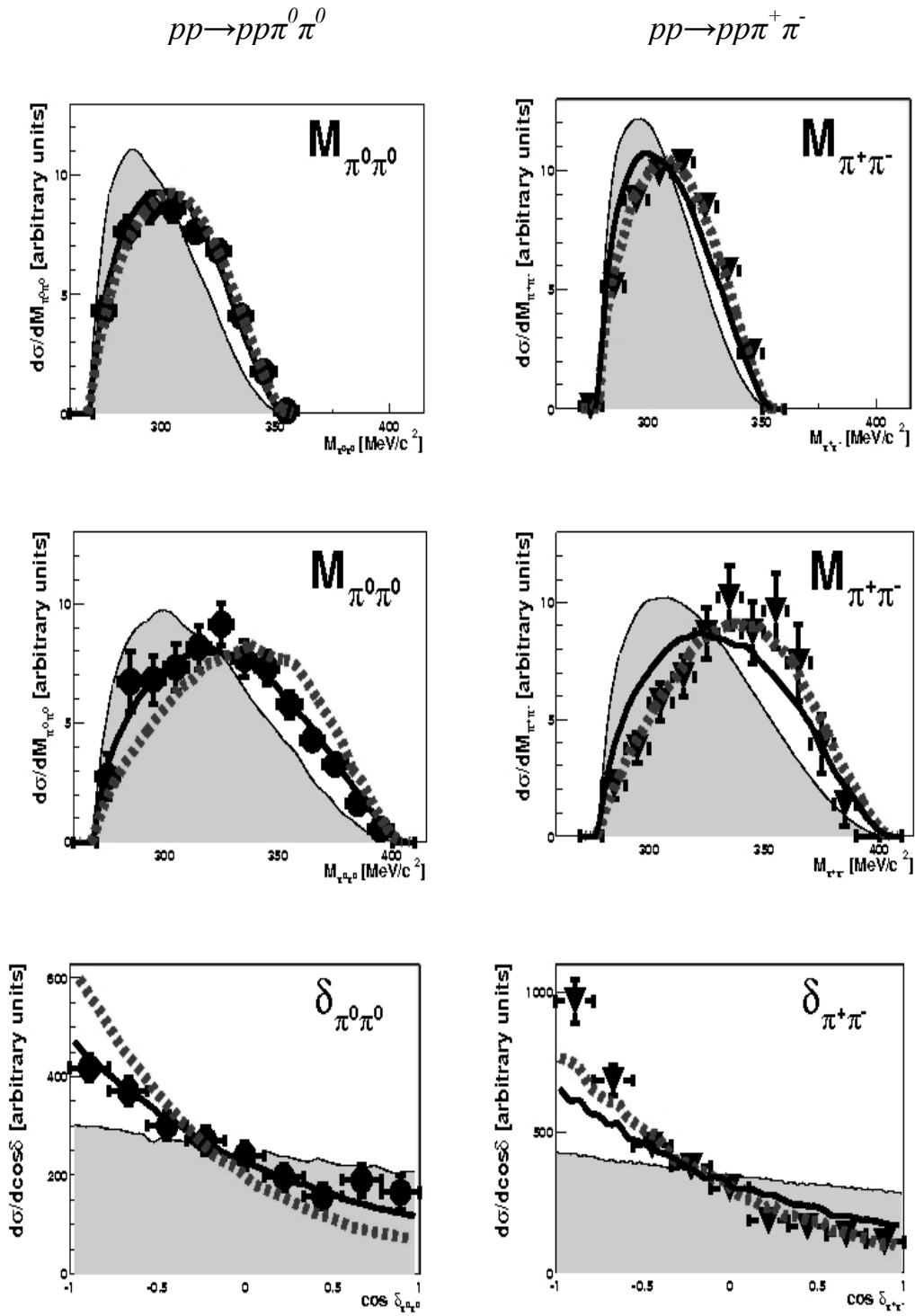
Figure 4.5 *Distributions of invariant masses and opening angles between two pions for $\pi^0\pi^0$ (left column) and $\pi^+\pi^-$ (right column) channels. Top row is data at $T_p=0.775$ GeV, middle and bottom ones are data at $T_p=0.895$ GeV. Black lines are the Roper ansatz calculations with parameters adjusted to $\pi^0\pi^0$ data, dotted lines are the Roper ansatz calculations with parameters adjusted to $\pi^+\pi^-$ data [9, 42].*

with $a = c\langle k_1 k_2 \rangle$, where $\langle k_1 k_2 \rangle$ denote the average over all possible momenta combinations. Since the decay route $N^* \rightarrow N\sigma$ gives a behavior close to phase

space, a larger parameter c gives a larger difference between the predicted behavior and phase space. In Fig. 4.5 one can see, that the Roper ansatz calculation with the c parameter adjusted to the $\pi^+\pi^-$ channel differs from the calculation, where c is adjusted to the $\pi^0\pi^0$ channel. In the latter case $M_{\pi\pi}$ and $\delta_{\pi\pi}$ have less deviations from phase space, i.e. the total amplitude includes less contribution from the decay route $N^* \rightarrow \Delta\pi$. This difference is small at the beam energy 0.775 GeV, but it becomes clearly visible at the incident energy 0.895 GeV.

The reason for this discrepancy is presently not clear. The new COSY-TOF data for the $\pi^+\pi^-$ production at T_p=0.8 GeV are in full agreement with the small value of c as obtained from the analysis of the $\pi^0\pi^0$ data [28]. This points to a need for a more careful reanalysis of the $\pi^+\pi^-$ data at least at T_p=0.9 GeV.
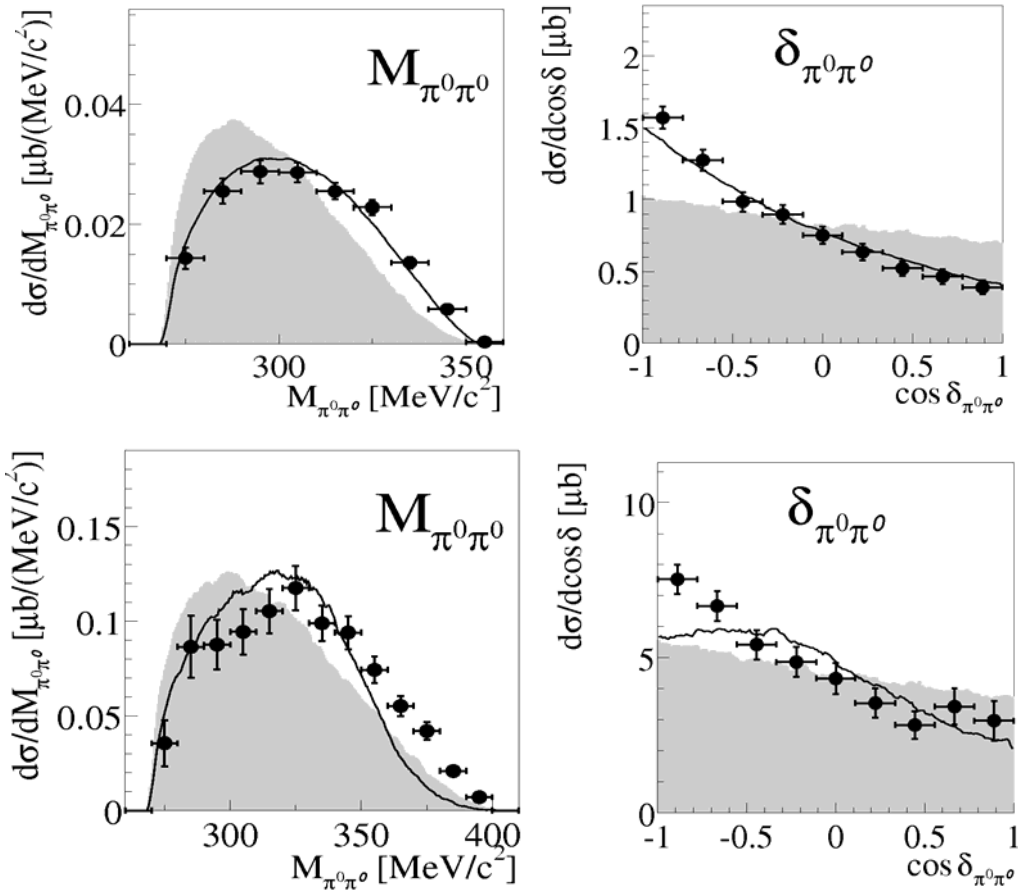
Figure 4.6 *Invariant mass and opening angle between two π^0 at T_p=0.775 GeV (top) and T_p=0.895 GeV (bottom). Phase space is shown as grey area, black lines are calculation from [11] including dynamical $\pi\pi$ rescattering in the final state.*

Since the $\pi^+\pi^-$ data have also been reasonably well described by calculations based on the dynamical $\pi\pi$ rescattering in final state [11], we also confront these calculations with the $\pi^0\pi^0$ data obtained at beam energies of 0.775 and 0.895 GeV (fig. 4.6). One can see that the calculations give a reasonable data description at 0.775 GeV, but fail at 0.895 GeV. Furthermore, these calculations give predictions for the total cross sections, but they need one experimental point for

normalisation (Fig. 4.7). Thus, in agreement with data $\pi\pi$ rescattering may have some contribution in the reaction dynamics at threshold energies, but with increasing energy the $\pi\pi$ production can not be described without an explicit inclusion of resonances.
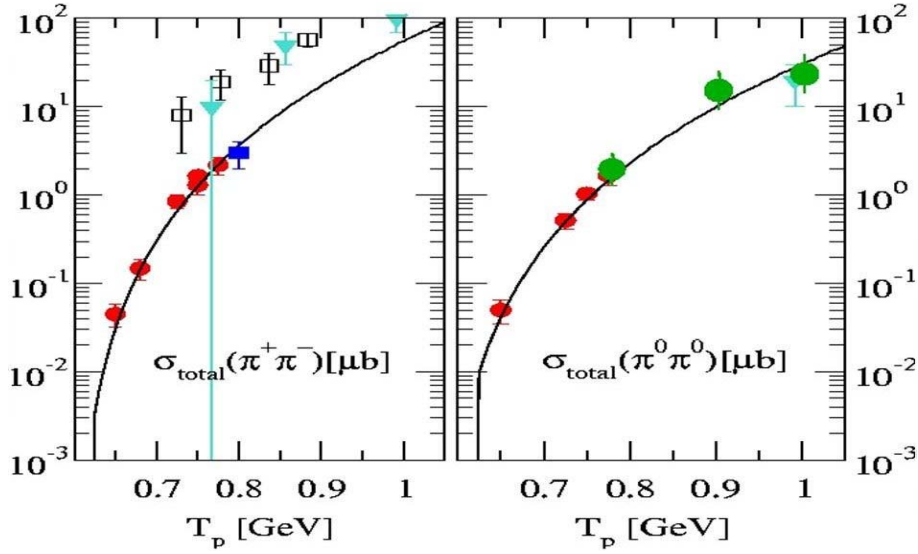

Figure 4.7 *Total cross section reaction as a function of proton kinetic energy beam in the laboratory frame. Left: $pp{\to}pp\pi^{+}\pi^{-}$ channel, right: $pp{\to}pp\pi^{0}\pi^{0}$ channel. The red points are PROMICE/WASA data [9,29], the green ones are CELSIUS-WASA data (this work), the open squares and blue triangles are bubble-chamber data [3], the dark-blue square denotes a COSY-TOF data [28]. The solid lines are calculations for the model from Ref. [11].*

Next we compare the $\pi\pi$ production data with the original Valencia model predictions. Since even at low energies the Valencia Model calculations include in their total reaction amplitude not only the contribution from the Roper excitation, but also from other mechanisms, we wanted to check both the $\pi^{+}\pi^{-}$ and the $\pi^{0}\pi^{0}$ channels, if the interference of small amplitudes with the large Roper amplitude is able to give a significant contribution to the differential cross sections.

For the $\pi^{+}\pi^{-}$ channel at beam energies of 0.75 and 0.775 GeV the Valencia model describes the data similarly well as the Roper ansatz. However, though the Valencia model calculations include terms with the Δ excitation, the model can not describe properly the invariant masses $M_{p\pi^{+}}$ and $M_{pp\pi^{-}}$. Note also that the

Valencia calculations do not reproduce the observed analyzing power [28]. In Fig. 4.8 one can see the comparison of the experimental data for the $pp{\to}pp\pi^{0}\pi^{0}$ reaction at beam energies 0.775 and 0.895 GeV with the Valencia calculations. The Valencia predictions based on the branchings from PDG (25% for $\Delta\pi$ branch and 7.5% for $N\sigma$ branch) are shown by the dashed lines. They obviously, especially at beam energy of 0.895 GeV, show excessive shifts in the invariant-mass spectra and much too steep angular distributions in the opening angle spectra in comparison to the data. The solid lines on the other hand, which represent the

Valencia calculations, but with half the amplitude for the $\Delta\pi$ decay branch, are in a good agreement with the experimental data (Appendix A, B).
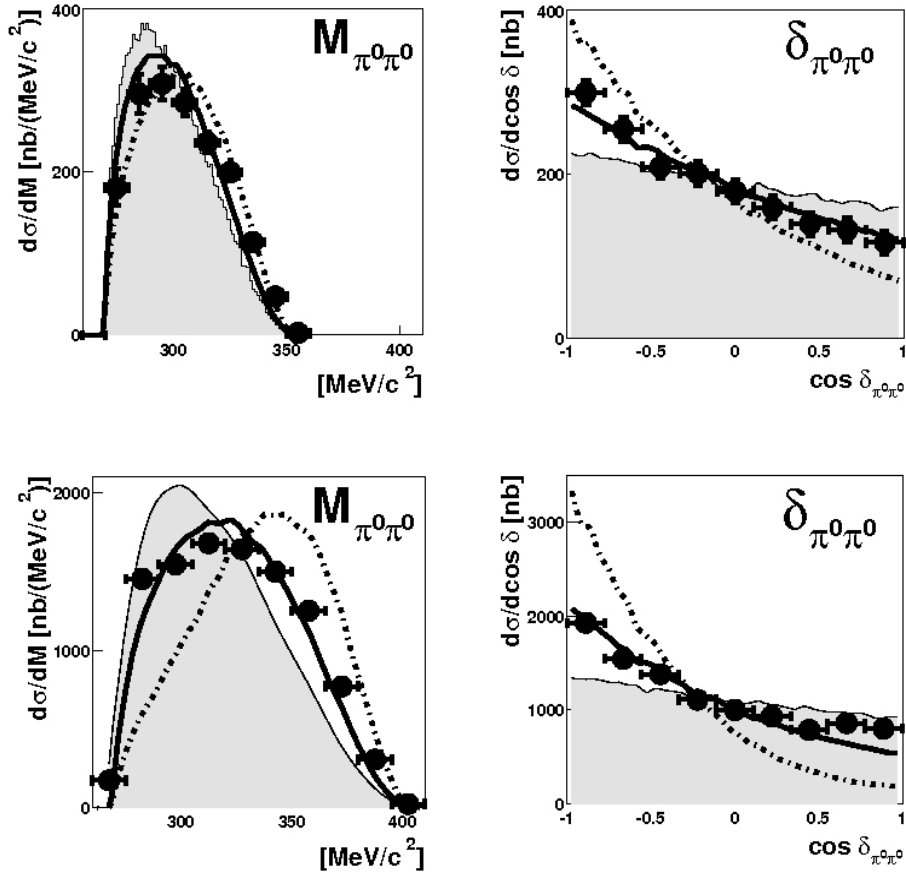

Figure 4.8 *Spectra of invariant mass $M_{\pi\pi}$ and opening angle $\delta_{\pi\pi}$ for the $pp \to pp\pi^0\pi^0$ reaction at $T_p = 0.775$ GeV (top) and 0.895 GeV (bottom). The grey areas denote the phase space distribution. Dotted lines are original Valencia model predictions, solid ones are the calculations, if the amplitude for the decay $N^* \to \Delta\pi$ is reduced by factor of two.*

A similar result has been obtained in [28] for $\pi^+\pi^-$ production at an incident energy of 0.8 GeV. These data are also in favour of a Roper decay $N^* \to \Delta\pi$ being smaller by a factor of two in amplitude than assumed in the VM calculations.

The decay branchings of a resonance depend also on the assumed mass of resonance, since partial decay widths depend on the available decay phase space. In Ref. [5] it has been calculated that with a Roper mass of about 1370 MeV the partial decay width for the branch $N^* \to \Delta\pi \to N\pi\pi$ becomes compatible with the partial decay width for the branch $N^* \to N\sigma \to N\pi\pi$, whereas at a Roper mass of about 1440 MeV the partial decay width $N^* \to \Delta\pi$ is by a factor of 4 bigger than partial decay width $N^* \to N\sigma$. Thus as discussed in detail in Ref. [30] we obtain the following results for the branching ratios of the $\pi\pi$-decays of the Roper resonance, which are shown in Tab. 4.3

With data obtained at CELSIUS-WASA we try now in the following to check, which mass of the Roper resonance is the proper one.

N^* mass (MeV)	1358	1371	1440
CELSIUS-WASA [30]	0.22(2)	0.29(3)	1.0(1)
PDG [35]			4(2)
Bonn-Gatchina [42]			0.9(1)[a]

[a] At 1436 MeV

Table 4.3 *Ratio R = Γ(N*→Δπ→Nππ)/Γ(N*→Nσ→Nππ) of the partial decay widths for the decay of the Roper resonance. The ratio is quoted for various effective N* masses, which mark either pole positions obtained from recent partial-wave analyses [36, 42] or the conventional Breit-Wigner mass of 1440 MeV.*

4.2.2 Roper resonance

Up to now the first excited state of the nucleon, known as the Roper resonance, remains one of the most controversial resonances in baryon spectroscopy. Up to now its theoretical description causes severe problems, in particular its excitation energy. In several models the Roper resonance is described as a 3-quark state [31], in Ref. [32] it is generated dynamically, in bag [33] and in Skyme models [34] the Roper resonance is interpreted as a surface oscillation. Furthermore, properties obtained from different experimental observables are not consistent, the resonance parameters mass M and width $Γ$ have rather large uncertainties.

From its discovery in the phase shift analysis the Roper resonance appeared not as the Breit-Wigner-like (BW) resonance. As an example of the difference between the Roper and an usual BW resonance *N(1520)* πN phase shifts and inelasticities for partial waves P_{11} and D_{13} are presented in Fig. 4.9. In the case of the partial wave D_{13} the phase shift changes sharply from 0^0 to 180 crossing 90^0 at about 1520 MeV. 1520 MeV is also exactly the value at which the inelasticity has its maximum decreasing afterwards back to almost zero. In the case of the partial wave P_{11} the situation is totally different. The phase shift changes slowly corresponding to a very broad resonance, but the inelasticity increases very fast remaining afterwards close to the maximum value.

Mass and width of a resonance can be derived from partial wave amplitudes by BW fits or by a pole analysis. Usually both methods give very similar results. The Roper resonance again is exceptional – with a large difference between BW and pole results. The PDG value [35] as well as the value from the SAID analysis (πN data [36]) and from Bonn-Gatchina (πN and γN data [42]) are given in Tab. 4.4. In spite of significant attempts to see the Roper resonance directly in the measured spectra, only two experiments could claim so far that they observed a resonance-like structure associated with the Roper resonance. In both

experiments the Roper resonance has been observed at a mass less than the nominal value of 1440 MeV.
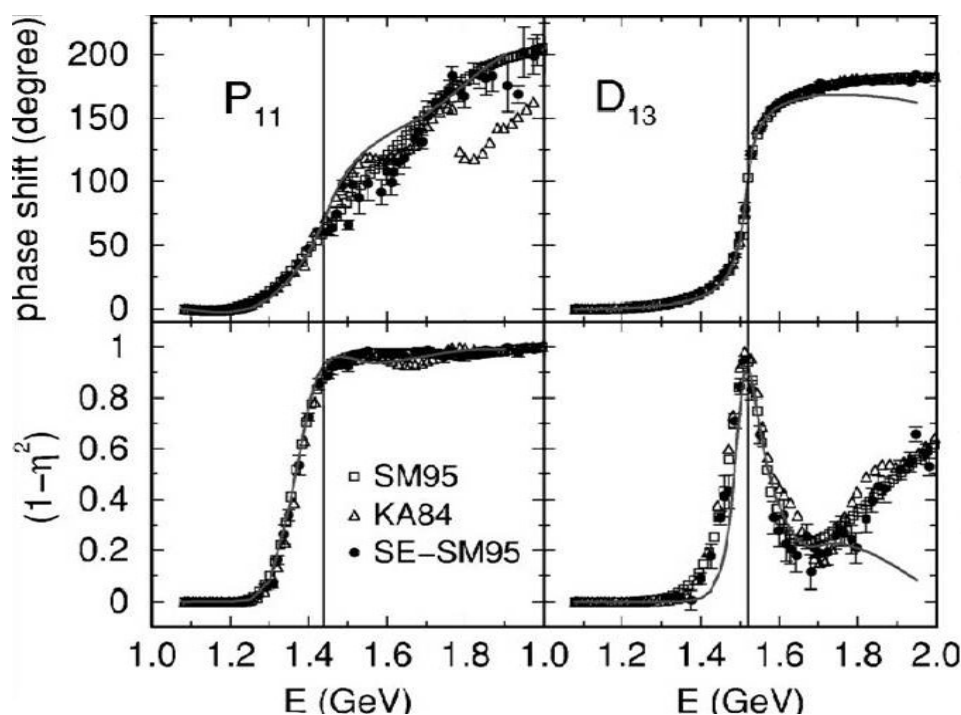

Figure 4.9 *Phase shift and inelasticity in the πN partial waves P_{11} and D_{13}. The vertical lines are drawn at E=1440 MeV (P_{11}) and E=1520 MeV (D_{13}) and correspond to the suggested values (PDG) for the resonance masses. The figure is taken from [32].*

	BW		pole	
	M [MeV]	Γ [MeV]	M [MeV]	Γ [MeV]
PDG	1440	300	1365	190
SAID	1468	360	1357	160
Bonn-Gatchina	1436	335	1371	192

Tab. 4.4 *The mass and the width of the Roper resonance obtained in Ref. [35, 36, 42]*

The first experiment (Fig. 4.10) was performed at Saturne [37] as rescattering of α-particles on a hydrogen target at an α-beam energy of 4.2 GeV. In this experiment both target and projectile could be exited, but in the target only the Roper excitation is allowed due to isospin conservation. In the projectile the largest contribution should be from the delta resonance since there are no withstanding selection rules. The contribution from the Roper resonance was calculated to originate from a Breit-Wigner resonance with a mass of M=1390 and a width of Γ=190 MeV. Later these data were reanalyzed by the Valencia group [38] and they came to the conclusion, that between Delta and Roper an

interference occurs, which results in such a way that the spectrum can be described by conventional BW parameters of the Roper resonane. But in any case, this experiment was the first one, where the Roper was observed directly. From the Saturne data Morsch et al. [37] concluded that, since the Roper has the same quantum numbers as a nucleon, it is a monopole excitation of the nucleon and hence it could be exited better by the scalar probe.
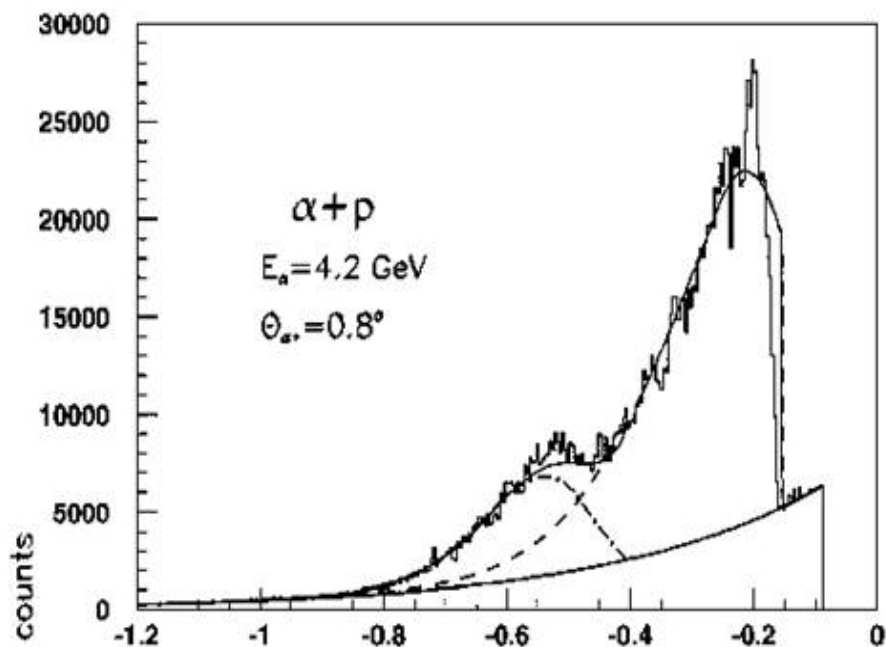

Figure 4.10 *Missing energy spectrum of the rescattered α particles in the inclusive reaction α+p→α+X. Solid line is the full theoretical description including the contribution from the Δ (dashed line) and the Roper resonances (dot-dashed line). The figure is taken from Ref. [37].*

The second experiment was recently performed by the BES collaboration [39]. They studied the decay of J/ψ into nucleon and antinucleon. Since J/ψ is scalar, the $N\overline{N}$ system has to be scalar, too. Therefore only the excitation in resonances with isospin $I=\dfrac{1}{2}$ is allowed in this case. The BES collaboration observes in the $M_{p\pi^-}$ and $M_{\overline{p}\pi^+}$ spectra (Fig. 4.11) a resonance structure, which can be described by a Breit-Wigner resonance with mass $M=1358$ MeV and width $\Gamma=160$ MeV. This structure has been associated with the Roper resonance by the BES collaboration.
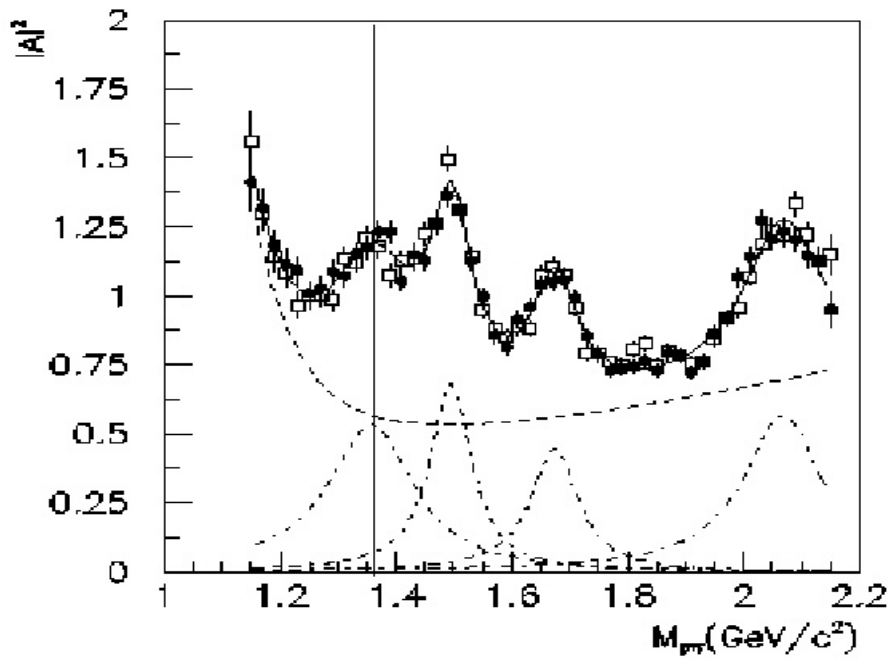
Figure 4.11 *Invariant mass* $M_{p\pi}$ *spectrum divided by Monte Carlo phase space. Solid squares are data for* $J/\psi \rightarrow p\pi^-\bar{n}$, *open squares are data for* $J/\psi \rightarrow \bar{p}\pi^+n$. *The solid line is a fit where contributions from each resonance are shown by the dot-dashed lines. The dashed line is the fitted contribution of background. The vertical line is drawn at* $M_{p\pi}$ = 1360 MeV. *The figure is taken from Ref. [39].*

4.2.2.1 pp → pnπ⁺ reaction

Originally, the reaction $pp \rightarrow pn\pi^+$ has been chosen to estimate the neutron registration efficiency in FD. The data analysis at a beam energy of 1.1 GeV shows a clear Δ^{++} excitation in the $M_{p\pi^+}$ spectra and also an unexpected structure at high invariant masses $M_{n\pi^+}$, which could not be reproduced in simulations with solely Δ^{++} excitation. We realized that at this relatively low beam energy in addition to the Δ only the Roper resonance could be excited. Indeed, the $pp \rightarrow pn\pi^+$ reaction around $T_p \approx 1.2 \div 1.4$ GeV is well suited for the Roper excitation study, since:

• due to isospin coupling the Roper resonance decay into nπ⁺ or pπ⁻ subsystems is preferred;

• the rather low beam energy allows to excite only the Δ and the Roper resonances;

• the Δ^{++} can be excited only in the pπ⁺ subsystem. In the nπ⁺ subsystem the Δ^+ and the Roper can be excited, but the Δ^+ is isospin-suppressed by a factor of nine in intensity relative to the Δ^{++} excitation;

- the possibility to observe the Roper excitation in proton-proton collisions has been proved in $(\pi\pi)_{I=0}$ production at low energies. The data analysis shows a good agreement with the Valencia calculation predicting the main reaction mechanism to be the Roper excitation initiated by σ-exchange.

The $pp \to pn\pi^+$ data have been analyzed at T_p=1.3 GeV. This energy allows to observe the $M_{n\pi^+}$ spectrum beyond the pole position of the Roper resonance. Unfortunately, since the idea to analyze the Roper excitation in this channel has arisen only after data collection, we had no specially prepared triggers but just the ones installed for other reactions. This is the main reason, why both obtained data samples, especially selected with one charged track in FD and the other charged one in CD, have low acceptance in the region, where the signal from the Roper excitation is expected to be largest (Fig. 4.12).

Since data selections were done at two different triggers (with different prescalar factors) and at different requirements for MDC, they have been analyzed separately. After efficiency and acceptance corrections they were joined as a weighted average with weights inversely proportional to the squared statistical error obtained after corrections.
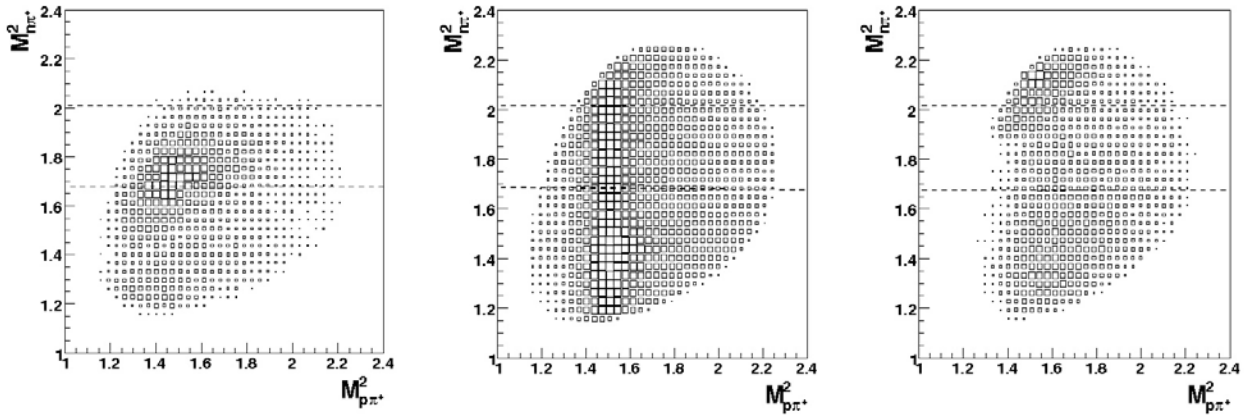
Figure 4.12 *Scatterplot of $M_{p\pi^+}^2$ versus $M_{n\pi^+}^2$ for MC calculations including Δ^{++}, Δ^+ and Roper resonances. Left: reconstructed MC data after selection with two charged tracks in CD (2DC). Right: reconstructed MC data after selection with one charged track in FD and one charged in CD (FDCCDC). Middle: MC data for full phase space. Dashed lines show the region where the Roper signal is expected to be observed.*

We describe the obtained data by a toy-model, in which the reaction amplitude has been written as:

$$A^2 \sim D_\pi^2 \mid A_{\Delta^{++}} - \frac{1}{3} e^{i\varphi} A_{\Delta^+} \mid^2 + \frac{8}{9} \mid a D_\sigma \cdot A_{Roper} + b D_\pi A_{N^*(1520)} \mid^2 \qquad 4.4$$

with the amplitudes A_Δ, A_{Roper} and $A_{N^*(1520)}$ [40,41]:

$$A_{\Delta} = \frac{(\sigma\vec{q})(S\vec{q})(S\vec{k})}{M_{p\pi} - M_{\Delta} + i\Gamma(\vec{k})/2} FF_1 \ ,$$

$$A_{Roper} = \frac{(\sigma\vec{k})}{M_{n\pi} - M_{Roper} + i\Gamma(\vec{k})/2} FF_2 \ ,$$

$$A_{N^*(1520)} = \frac{(\sigma\vec{q})(\sigma\vec{q})(\sigma\vec{k})}{M_{n\pi} - M_{N(1520)} + i\Gamma(\vec{k})/2}$$

with

$$FF_1 = \frac{\Lambda_1^2 - m_\pi^2}{\Lambda_1^2 - q^2} \ , \quad FF_2 = \frac{\Lambda_2^2 - m_\sigma^2}{\Lambda_2^2 - q^2} \ ,$$

$$(S\vec{q})(S\vec{k}) = |\vec{q}| \cdot |\vec{k}| (2\cos\vec{q}\vec{k} - i\sigma\sin\vec{q}\vec{k}) \ ,$$

$$(\sigma\vec{q})(\sigma\vec{k}) = |\vec{q}| \cdot |\vec{k}| (\cos\vec{q}\vec{k} + i\sigma\sin\vec{q}\vec{k}) \ ,$$

$$\Gamma(k) = \Gamma_0 \frac{k}{k_{resonance}} Z(k) \ , \quad Z(k) = \frac{k_{resonance}^2 + \alpha^2}{k^2 + \alpha^2}$$

We used $\Gamma_0 = 90\,\text{MeV}$ for the Δ, $\Gamma_0 = 150$ MeV for the Roper and $\Gamma_0 = 110$ MeV for $N^*(1520)$. Here k is the pion momentum in the $N\pi$ rest frame, q is the transfer momentum in the overall center mass frame, $k_{resonance}$ denotes the decay momentum in the resonance rest frame. The function $Z(k)$ has been inserted in [41] as a phenomenological form factor to reduce the width with increasing energy with $\alpha = 200$ MeV for the Δ resonance and $\alpha = 300$ MeV for the Roper . FF_i are form factors which account for the finite size of the mesons [8]. The cutoff parameter Λ has been chosen as 1200 MeV for the Δ and 1700 MeV for the Roper [8]. We did not introduce any form factor for the $N^*(1520)$, because we can assume that at our energy it has to be close to 1. D_π and D_σ denote π- and σ-propagators correspondingly, the factors $\frac{1}{3}$ and $\frac{8}{9}$ are due to isospin coupling.

The parameters a and b have been adjusted to the data and used to estimate the Roper and the $N^*(1520)$ contribution. $e^{i\varphi}$ denotes the phase between the Δ^{++} and Δ^+ which we included in order to describe better our data. The best agreement with data was found for $\varphi = 3/4\,\pi$.

In Fig. 4.13-4.15 the data are compared to three different toy-models:
- figure 4.13 –only Δ^{++} and Δ^+ excitations included in calculations;
- figure 4.14 - Δ^{++}, Δ^+ and $N^*(1520)$ excitations included;
- figure 4.15 - Δ^{++}, Δ^+ and Roper excitations included.

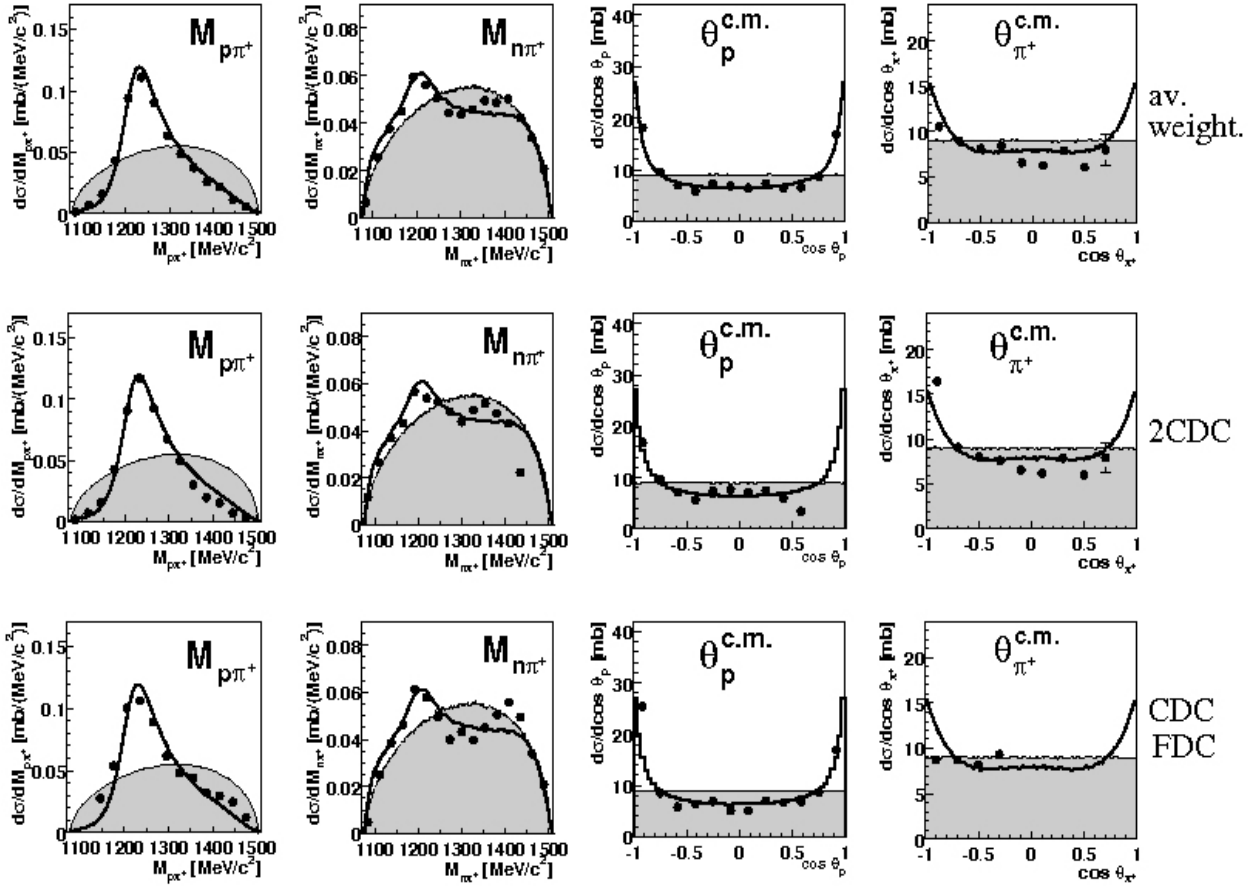In each case we have used the tested model for the acceptance and efficiency corrections.

Figure 4.13 *Invariant masses $M_{p\pi}$ and $M_{n\pi}$ as well as proton and pion opening angles in the overall central mass frame. Top row is the average weighted result, obtained from data shown in middle row (2CDC selection) and from data shown in bottom row (FDCCDC selection). The grey area denotes phase space, the solid lines show the calculation for the toy-model including only the Δ^{++} and Δ^{+} excitations.*
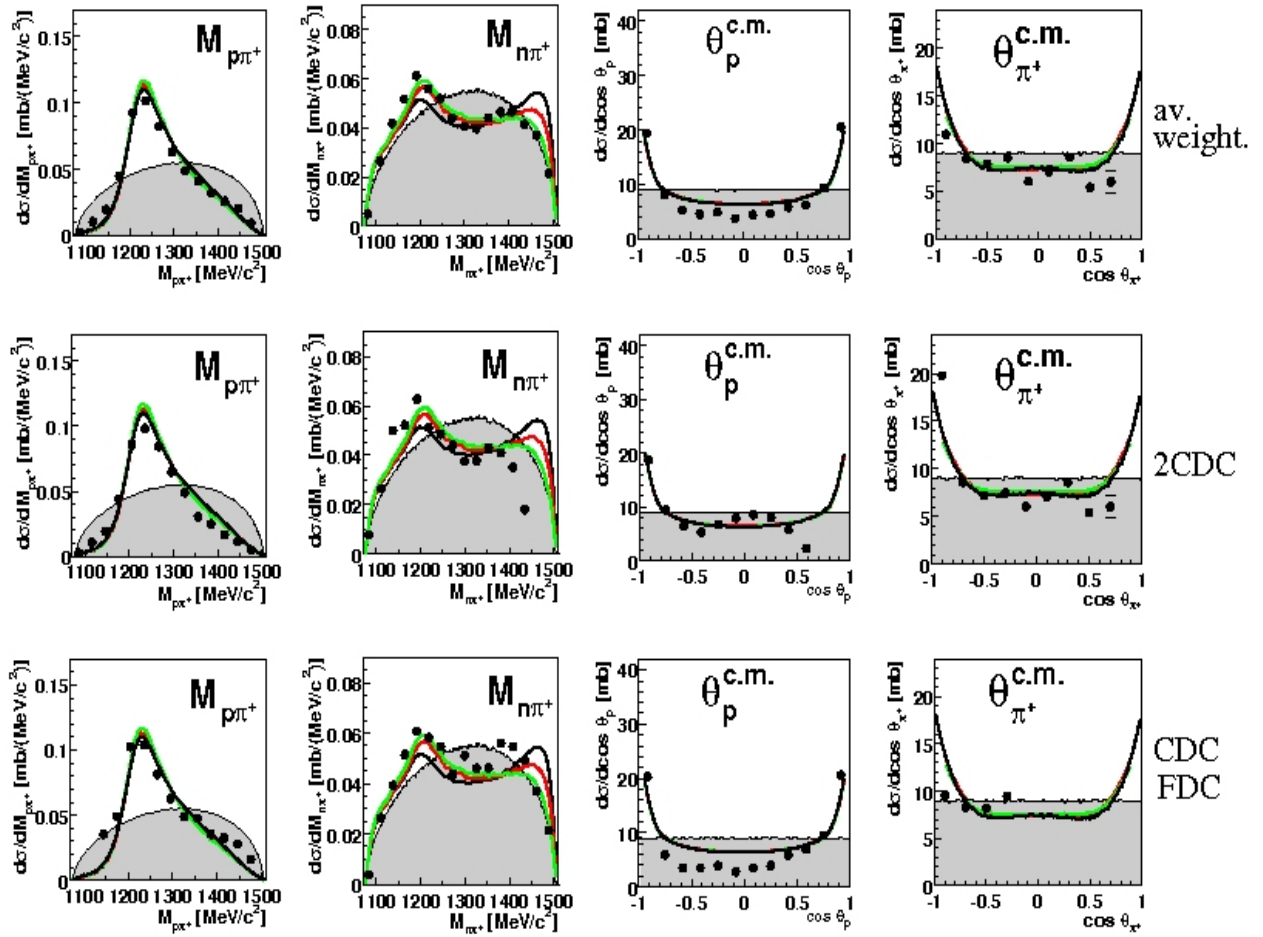
Figure 4.14 *Same as Fig. 4.13 except for the color lines, which represent the toy-model including the Δ^{++}, Δ^{+} and $N^{*}(1520)$ excitations. Green line is the $N^{*}(1520)$ contribution with strength b=0.5; the red one corresponds the $N^{*}(1520)$ contribution with strength b=0.8; the solid one is the $N^{*}(1520)$ contribution with strength b=1. Data have been acceptance and efficiency corrected using the toy-model calculated for the $N^{*}(1520)$ contribution with strength b=1.*
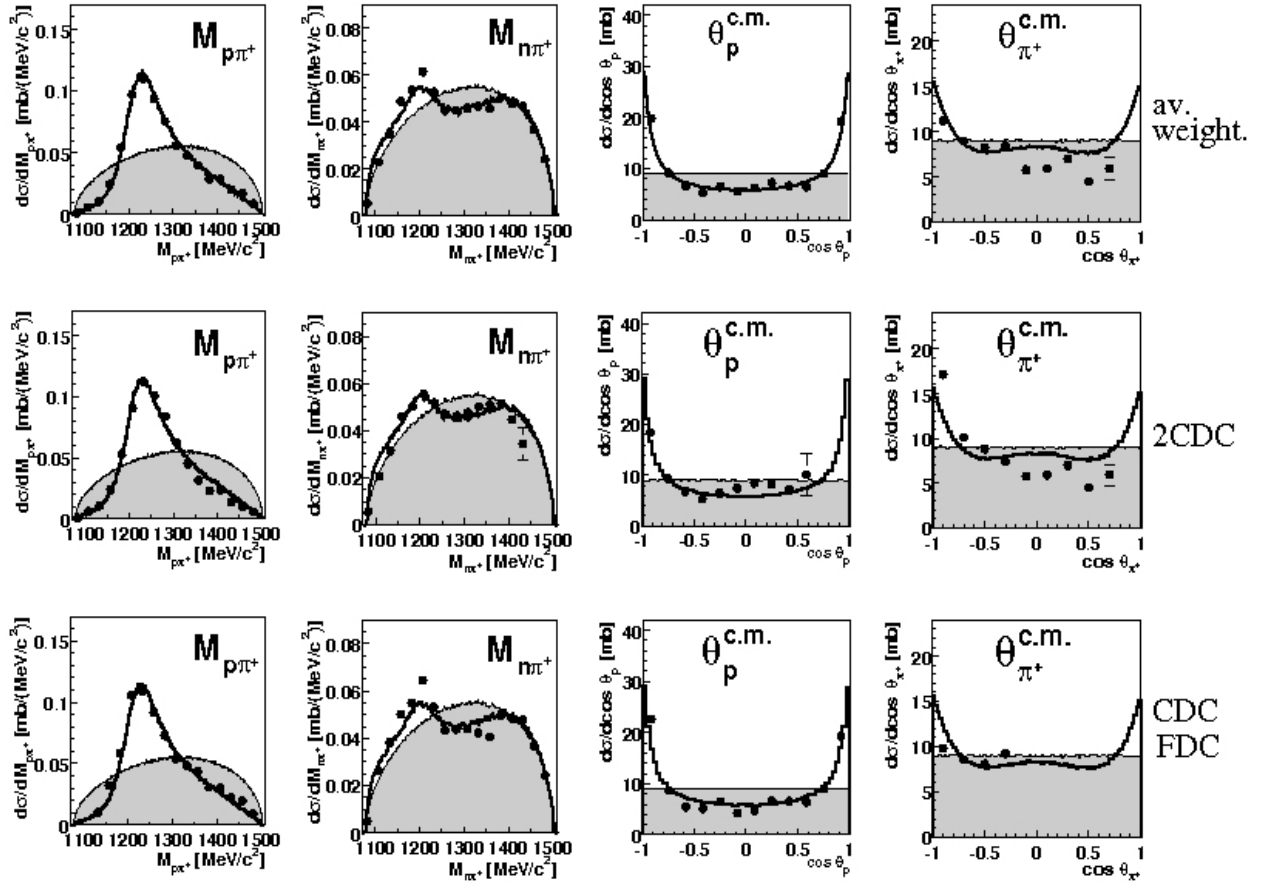
Figure 4.15. *Same as Fig. 4.13 except for the solid curves which represent the toy-model including the Δ^{++}, Δ^{+} and the Roper excitations, the later with strength a=0.2 and mass M=1400 MeV .*

One can see that the corrected data slightly depend on the used model but all data clearly show the Δ^{++} excitation in the $M_{p\pi}$ invariant mass and the Δ^{+} excitation at low $M_{n\pi}$ invariant mass. Also one can see an enhancement at high $M_{n\pi}$ invariant mass. This is not reproduced by the toy-models, neither as a kinematical reflection of the Δ excitation, nor as tail of the $N^{*}(1520)$ resonance. However, it is reproduced by a contribution from the Roper excitation with strength a=0.2. Since in our toy-model we have an arbitrary absolute normalization, the value of the parameter *a* can be understood from formula (4.5) as the contribution from the Roper excitation relative to the Δ amplitude, i.e. (Fig. 4.16):

$$a = 0.2 \approx \frac{g_{\sigma NN^{*}} \cdot g_{\sigma NN} \cdot g_{\pi NN^{*}}}{g^{2}_{\pi N\Delta} \cdot g_{\pi NN}} = 0.165 \qquad 4.5$$

For the numerical value we here adopted the coupling constants from [41].

The Feynman diagrams show the Δ and Roper excitations with coupling constants $g_{\pi N\Delta}$, $g_{\pi NN}$ for the Δ excitation (left) and $g_{\sigma NN^*}$, $g_{\pi NN^*}$, $g_{\sigma NN}$ for the Roper excitation (right).

$$A_\Delta = g_{\pi NN}\, g_{\pi N\Delta}\, g_{\pi N\Delta}\, D_\pi D_\Delta$$

$$A_{Roper} = g_{\sigma NN}\, g_{\sigma NN^*}\, g_{\pi NN^*}\, D_\sigma D_{Roper}$$
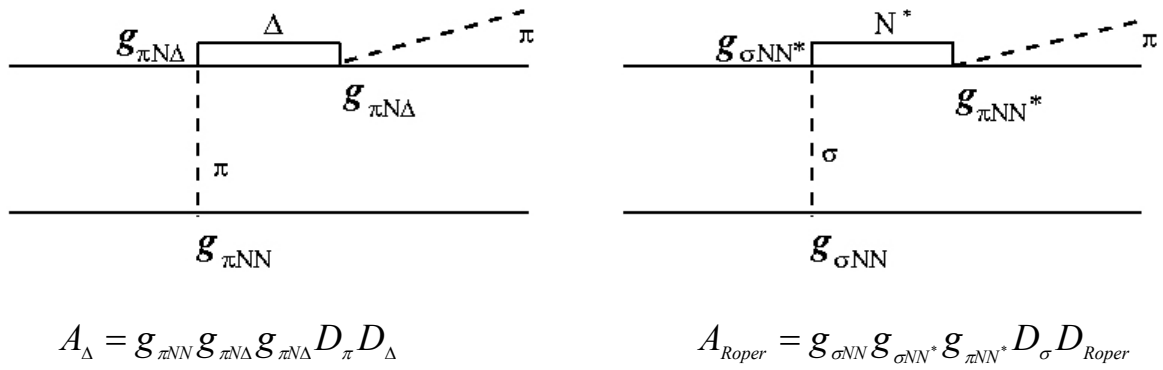
Figure 4.16. *The Feynman diagrams of the Δ and Roper excitations.*

In Fig. 4.17 we give a comparison between the Dalitz plots for experimental data and MC data. For the MC data the toy-model including the Δ^{++}, Δ^+ and Roper excitations has been chosen. The experimental data have been corrected using this model. In this comparison both MC and experimental data were collected in one sample before correction. The data selected as 2CDC tracks got an additional weight, taking in account the different trigger prescale factors and MDC efficiency. The weight due to the MDC efficiency has been calculated as a ratio of the pp_{el} events, selected in the same angle with and without MDC separately for MC and real data. The reaction $pp{\rightarrow}pp_{el}$ has been chosen due to its simple identification by the angular correlations between two protons. We found good agreement between the experimental and MC data.

Unfortunately, we could not extract the Roper mass accurately since the data obtained at 2CDC selection agree better with calculation with a Roper mass of about 1360 MeV, whereas the data obtained at the FDCCDC selection require a higher mass of about 1400-1420 MeV (fig. 4.18). For the combined data we obtained M=1380 MeV and Γ=180 MeV.

As discussed above, with a Roper mass less than the nominal value of 1440 MeV we could naturally explain the observed weaker contribution of the Roper decay branch $N^*{\rightarrow}\Delta\pi$ in the $\pi^0\pi^0$ production. Recently new results of a combined partial-wave analysis of pion- and photo-induced reactions have been published [42]. This work is focused on the Roper resonance properties and the most interesting conclusion concerns the Roper partial decay widths for $N^*{\rightarrow}\Delta\pi$ and $N^*{\rightarrow}N\sigma$ branches. Whereas the branching ratio $\Gamma_{\Delta\pi}/\Gamma_{tot}$=0.176±0.20 obtained in that work is not in conflict with the PDG value (20-30%), the branching ratio $\Gamma_{N\sigma}/\Gamma_{tot}$=0.212±0.30 is much bigger than the PDG value (5-10%) and - more essential - even bigger than the $\Gamma_{\Delta\pi}/\Gamma_{tot}$ ratio. The finding in Ref. [42] is in good agreement with our results for the decay branching, see Tab. 4.3
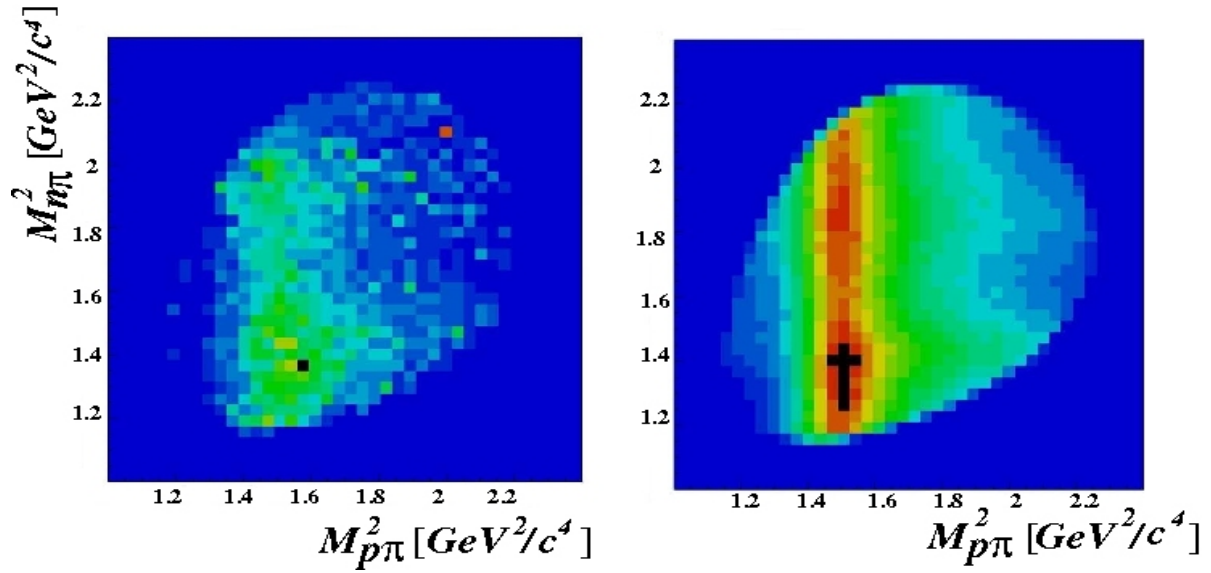
Figure 4.17 *Scatter plot of $M_{p\pi^+}^2$ versus $M_{n\pi^+}^2$. Left: the experimental data corrected using a model including Δ^{++}, Δ^+ and the Roper excitations with a Roper mass of M=1390 MeV and a relative strength a=0.15. Right: 4π MC data, representing the model used for the corrections.*
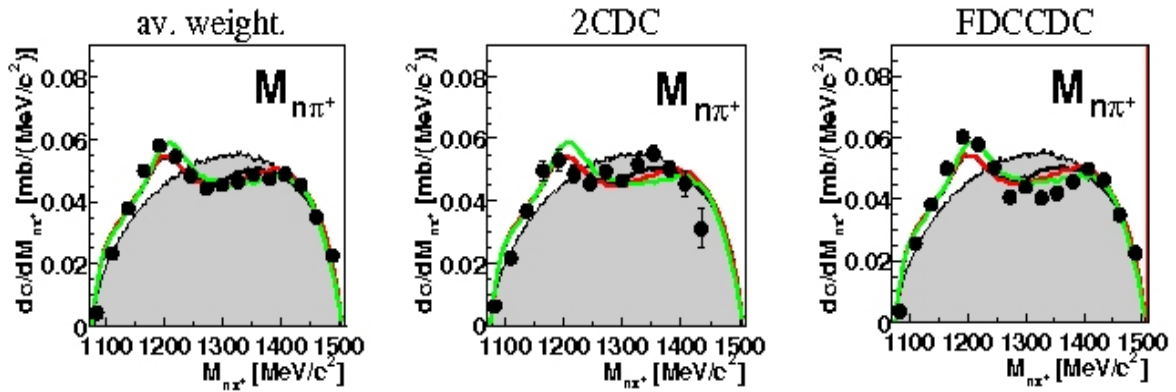

Figure 4.18 *$M_{n\pi^+}$ spectra. Left: average weighted data combined from data selected as 2CDC tracks (middle) with data selected as FDCCDC tracks (right). The grey area denotes phase space. The black solid line is the toy-model calculation with the Roper mass M=1360 MeV, the red one is the same calculation with the Roper mass M=1400 MeV and the green line is the calculation with the Roper mass M=1440 MeV. For the corrections the toy-model with M=1360 MeV has been chosen.*

4.2.3 $\pi^0\pi^0$ production at $T_p > 1.0$ GeV

With increasing incident energy above 1.0 GeV both $\pi^+\pi^-$ and $\pi^0\pi^0$ production data get into increasing contradiction to the Valencia calculations:

• At $T_p \sim 1.0\text{-}1.1$ GeV, where the model predicts still pronounced structures in $M_{\pi\pi}$ and $\delta_{\pi\pi}$ distributions due to the Roper decay branch $N^* \to \Delta\pi$, the data are close to phase space distributions for these observables (Fig. 4.1), in particular the $\pi^+\pi^-$ data [43].

• At $T_p \sim 1.2$ GeV and at higher energies the $M_{p\pi}$ spectra show a clear appearance of the $\Delta\Delta$ excitation as expected from the Valencia predictions. In Fig. 4.19 the $M_{p\pi^+}$ and $M_{p\pi^-}$ spectra for the $\pi^+\pi^-$ production data at $T_p=1.36$ GeV show that the Δ^{++} and Δ^+ have been excited simultaneously: both distributions have the same strength and the same maximum position. However, the Valencia calculations predict a double–hump structure in $M_{\pi\pi}$, since the $\Delta\Delta$ system is assumed to couple to all possible spin-parity combinations. Contrary to these expectations the measured $M_{\pi\pi}$ spectra are phase-space like (Fig. 4.19). Also the $\pi^\pm$ angular distribution stay flat [43] – again in contrast to the Valencia predictions. One possible explanation for this phase-space like behaviour of $M_{\pi\pi}$ and Θ_π spectra is that the $\Delta\Delta$ configuration is coupled to the specific configuration $(I, J^p)=(1, 0^+)$, which is equivalent to selecting the $^1S_0$ partial wave in the incident channel. Indeed, NN scattering calculations show that $^1S_0$ partial wave has a strong overlap with the $\Delta\Delta$ configuration [44].
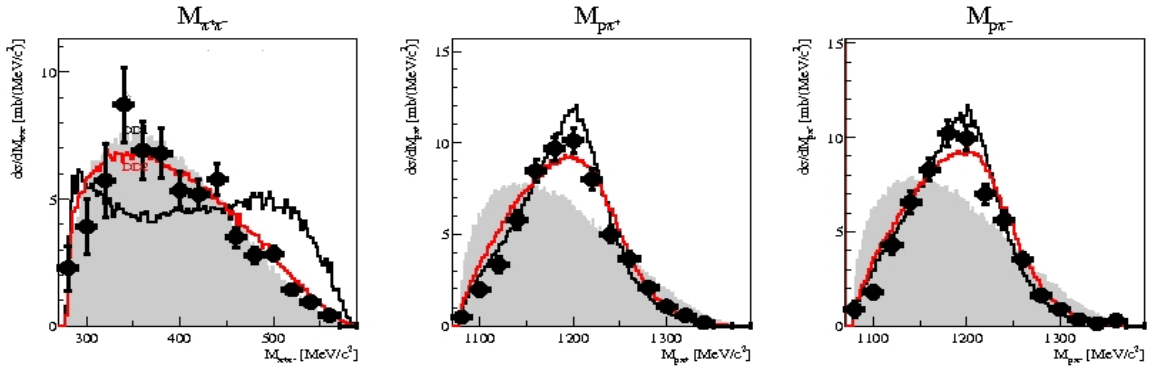

Figure 4.19 *Invariant masses from the $pp \to pp\pi^+\pi^-$ reaction at $T_p=1.36$ GeV. The grey area denotes phase space, the black lines show Valencia calculations, which include all possible $\Delta\Delta$ spin-parity combinations. The red lines correspond to calculations including only two Breit-Wigner terms for the $\Delta\Delta$ excitation [43].*

• For the $\pi^0\pi^0$ production data at energies above 1 GeV we systematically find an enhancement at low $M_{\pi\pi}$ masses, which is correlated with pion pairs flying in parallel (Fig. 4.20). Since only phase space corrected $\pi^+\pi^-$ data are available for a comparison, the $\pi^0\pi^0$ data in Fig. 4.20 are presented also acceptance and efficiency corrected by the phase space.
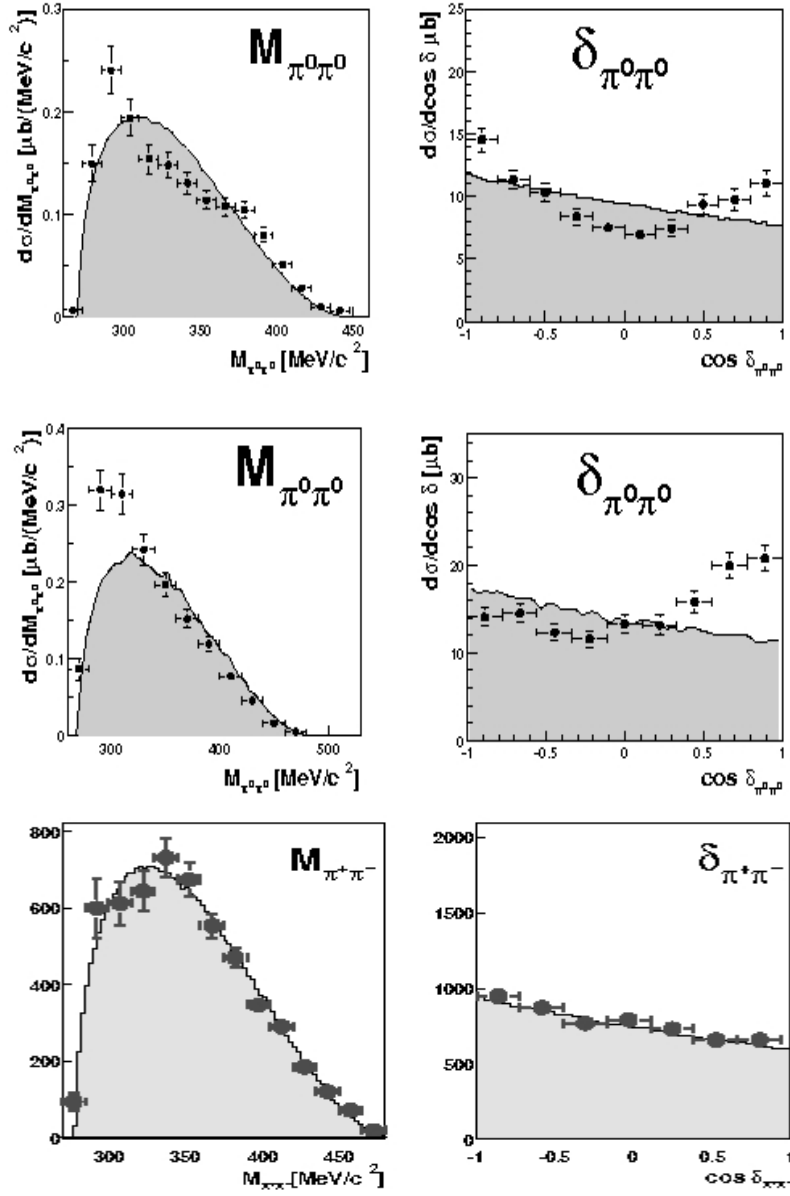
4.20 *Top and middle rows - invariant mass $M_{\pi\pi}$ and opening angle $\delta_{\pi\pi}$ from $pp{\to}pp\pi^0\pi^0$ reaction at $T_p=1$ GeV (top) and 1.1 GeV (middle). Bottom row - invariant mass $M_{\pi\pi}$ and opening angle $\delta_{\pi\pi}$ from $pp{\to}pp\pi^+\pi^-$ reaction at $T_p=1.1$ GeV [45]. The grey area denotes phase space. $\pi^0\pi^0$ and $\pi^+\pi^-$ data are acceptance and efficiency corrected by phase space.*

Since the enhancement at low $M_{\pi^0\pi^0}$ masses is practically the only discrepancy between the differential distributions of the $\pi^0\pi^0$ and $\pi^+\pi^-$ production data, we first checked, whether this enhancement can be due to an analysis error. In order to check energy and angle distributions in the laboratory frame we compared the experimental data with MC simulations, which included only two Breit-Wigner propagators for Δs. We did not find any essential difference between MC and experimental data. But unfortunately, in the region of low $M_{\pi^0\pi^0}$ we had a lower acceptance. Therefore any insignificant difference between MC and experimental data after correction could be strongly magnified.

We could not reproduce the enhancement by an admixture of single π^0 events assuming that in these events each cluster originating from a single gamma was wrongly reconstructed as two clusters. Such events did not pass the kinematical constraints applied for the $\pi^0\pi^0$ selection. We also tested the hypothesis, in which we assumed a shift in the vertex position for real data and another one, in which we investigated the possibility to lose in real data more protons in FD than in MC due to an underestimation of hadronic interactions in the simulations. Both hypotheses could not describe the observed enhancement.

Since we could not find errors in the selection and reconstruction procedure, we have tried to understand the physics hidden behind this behaviour in the data.

4.2.4 Bose-Einstein correlations

There is one difference between charged and neutral pions, which otherwise have to behave identical in strong interactions: $\pi^0\pi^0$ are identical bosons in contrast to $\pi^+\pi^-$.

The correlations between identical pions, known as identical pion interferomentry, have been used extensively in relativistic nucleon-nucleon collisions for studying the coherence and the dimensions of boson emitting sources [46].

The boson interferometry method is analogous to that proposed by Hanbury-Brown and Twiss in astronomy to determine the angular size of stars from the second-order interference of light [47]. Pion correlations appear as a consequence of pions obeying Bose-Einstein statistics: the wave function of identical bosons is symmetric with respect to particle exchange and this symmetrization requirement results in an interference term. Experimentally this is reflected in an enhanced production of pion pairs of the same charge, closely emitted in the phase space, as compared to the pairs with opposite charge. The width of this enhancement is used to estimate the spatial dimensions of the pion emitting region and the height of the interference peak is believed to reflect the degree of coherence of the pion source. This height is usually decreased by resonance production (when identical pions are produced as a decay product of the same resonance), strong final-state interactions, Coulomb repulsion etc [48].

In order to study the probability for emission of the two identical bosons, one usually defines a correlation function $C_2(Q)$:

$$C_2(Q) = \frac{\rho_{iden}(Q)}{\rho_{not}(Q)} \qquad\qquad 4.6$$

with $\quad \rho(Q) = \frac{1}{N_{event}}\frac{dN_{pairs}}{dQ}, \qquad Q = \sqrt{-(p_1 - p_2)^2} = \sqrt{M_{\pi\pi}^2 - 4m_\pi^2}$

where p_1 and p_2 denote the four-momenta of the two pions. The coefficient $\frac{1}{N_{event}}$ is a normalization factor. It is chosen to provide a value of unity for the correlation function at high invariant mass $M_{\pi\pi}$. One can see that the $\rho(Q)$ distribution practically equivalent to the invariant mass $M_{\pi\pi}$ distributions shifted by the mass of two pions.

Since the enhancement at low invariant masses $M_{\pi^0\pi^0}$ is correlated with pion pairs emitted at very similar angles, we investigated whether it could be an indication for Bose-Einstein correlations (BEC in the minimal system with solely two identical produced pions.

The major problem in this kind of study is to find an appropriate reference sample in order to create the correlation function. In our experiment we fortunately have the data for both identical ($\pi^0\pi^0$) and not identical ($\pi^+\pi^-$) pion production. We construct the correlation function $R(M_{\pi^0\pi^0})$ by dividing the observed $M_{\pi^0\pi^0}$ spectrum by that expected from the observed $M_{\pi^+\pi^-}$ spectrum in the following way: due to the $\pi^0/\pi^\pm$ mass difference $\pi^0\pi^0$ and $\pi^+\pi^-$ thresholds differ by as much as 9 MeV. Hence we cannot simply divide $\pi^0\pi^0$ and $\pi^+\pi^{--}$ spectra by each other, but rather have to account properly for the pion mass differences. Since for $T_p > 1.0$ GeV the $M_{\pi^+\pi^-}$ data are compatible with phase space, we obtain $R(M_{\pi^0\pi^0})$ just by dividing the $M_{\pi^0\pi^0}$ data by the phase-space distribution for this spectrum. The normalization of $R(M_{\pi^0\pi^0})$ is chosen such as to have unity for large $M_{\pi^0\pi^0}$ values. With this construction we assume the $\pi\pi$ spectra to be of isoscalar nature. Indeed, according to the isospin decomposition [49] of the $NN\pi\pi$ production cross sections, the contribution from $I_{\pi\pi}=2$ is strongly suppressed already by isospin coupling. The observed flat $\pi^\pm$ angular distributions exclude any major p-wave contribution between pions, which would be a consequence of $I_{\pi^+\pi^-}=1$. Also the $\Delta\Delta$ excitation mechanism, which dominates for $T_p > 1.0$ GeV, does not contribute to the isovector $\pi\pi$ channel.

Fig. 4.21 shows the correlation function $R(M_{\pi^0\pi^0})$ obtained for $T_p=1.1$ GeV. It exhibits some enhancement near $M_{\pi^0\pi^0}=2m_{\pi^0}$ and decreases to unity within the following 30-40 MeV. This behaviour resembles very much that known from Bose-Einstein correlations for identical bosons.

The enhancement factor of 1.8 at $M_{\pi\pi}=2m_{\pi^0}$ is below the maximum BEC enhancement of two and may mean that the two π^0 were emitted mainly incoherently. From a Gaussian fit to $R(M_{\pi^0\pi^0})$ we obtain a source size of

$$r_0 \cong \frac{h}{2\pi Q_0} \approx 2 \text{ fm},$$ where Q_0 denotes the FWHM value of the enhancement in $R(M_{\pi^0\pi^0})$. This value is very reasonable for the $\Delta\Delta$ system, but a rather short

distance could permit two Δs to be at least partially within their interaction range during their decay.

Since a BEC only occurs, if identical bosons are emitted from a chaotic source, i.e., with no phase relation between the emitted bosons, we have to ask, whether such a minimal system in a well-defined quantum mechanical state principally can meet the requirements for BEC.
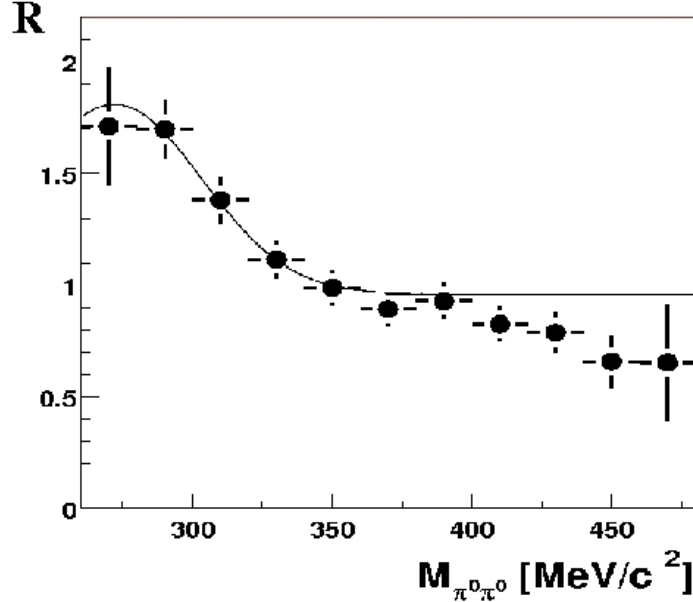

Figure 4.21 *Correlation function* $R(M_{\pi^0\pi^0})$ *deduced from the data at* $T_p=1.1$ GeV *for* $\pi^0\pi^0$ *and* $\pi^+\pi^-$ *channels assuming* $I_{\pi\pi}=0$. *The solid line gives a Gaussian fit to the correlation function with* $\chi^2/N_{freedom}=1.8$

4.2.4.1 pp→nnπ⁺π⁺ reaction

The $pp{\rightarrow}nn\pi^+\pi^+$ reaction appears to be very well suited to settle the question whether the two Δs decay independently, since:
- in the final state two identical bosons are produced, two π^+;
- if the Valencia predictions are correct, this reaction proceeds via the same intermediate ΔΔ configuration as the $pp\pi^0\pi^0$ channel (Fig. 4.22) Although two π^+ have the same electric charge and hence feel a long range repulsion, the BEC is affected only slightly [50] decreasing the value of BEC enhancement factor by about 10%. Hence, we should again observe the enhancement in the $M_{\pi^+\pi^+}$ spectrum. Indeed, almost all results about correlation functions obtained in nucleon-nucleon collision analyses have been obtained with charged pions [NA44, E877].
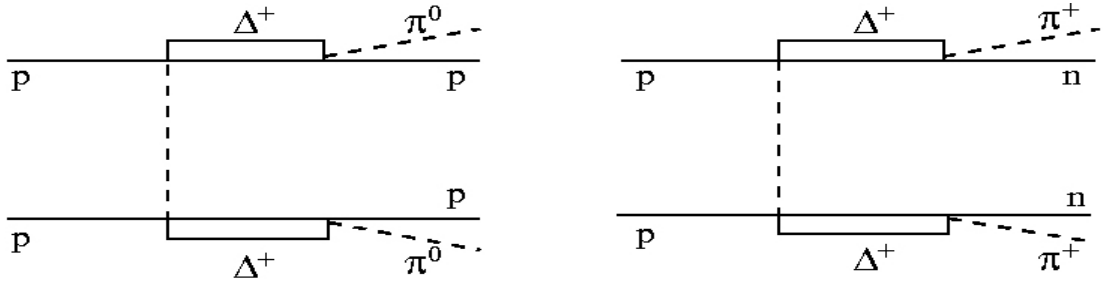
Figure 4.22 *Feynman diagrams of the pp→ ppπ⁰π⁰ reaction (left) and the pp→nnπ⁺π⁺ reaction (right), describing ππ production via two Δs.*

Fig. 4.23 depicts differential spectra obtained for the $pp{\rightarrow}nn\pi^+\pi^+$ reaction at T_p=1.1 GeV. Since this channel is very difficult to access experimentally, we got only rather poor statistics of the reconstructed events. However, our result is statistically meaningful to demonstrate that there is no particular low-mass enhancement in the $M_{\pi^+\pi^+}$ spectrum.
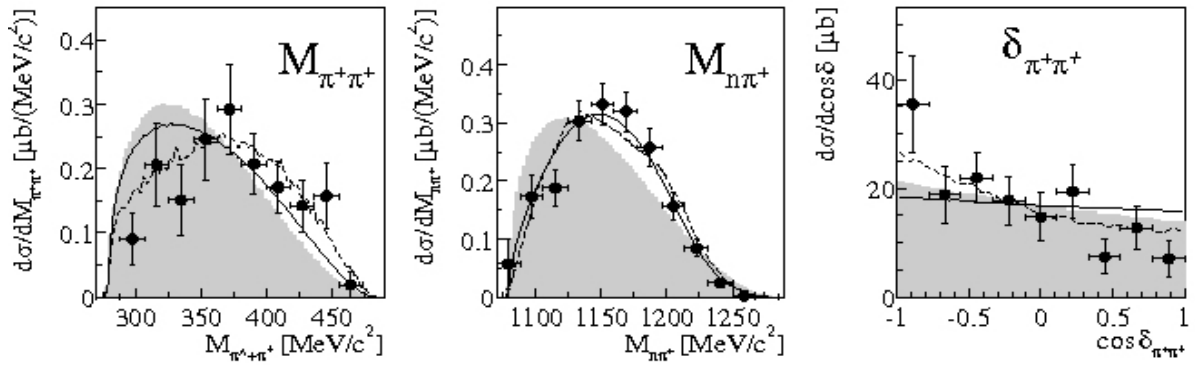
Figure 4.23 *Invariant masses $M_{\pi^+\pi^+}$ and $M_{n\pi^+}$ as well as opening angle $\delta_{\pi^+\pi^+}$ from the pp→nnπ⁺π⁺ reaction at T_p=1.1 GeV. The grey area denotes phase space, the solid lines show calculations for a ΔΔ configuration in a 0⁺ state, the dashed lines denote calculations, which in addition to the Valencia calculation include the Δ(1600) excitation (see chapter 4.2.6).*

We obtained a several time larger total cross section for this channel than predicted by the Valencia calculations. If the excitation of two Δs is the main reaction mechanism for $\pi^+\pi^+$ production, then due to isospin coupling the total cross section for the $pp{\rightarrow}nn\pi^+\pi^+$ channel should be four times less than the total cross section for the $pp{\rightarrow}pp\pi^0\pi^0$ reaction. However, we obtained in our experiment the total cross section for the $\pi^+\pi^+$ production even larger than that for $\pi^0\pi^0$ production at the same beam energy of 1.1 GeV. Our values for the total cross sections, however, agree well with bubble-chamber results. Therefore, we have to conclude that the $\pi^+\pi^+$ production must involve a rather strong contribution from another resonance with I=3/2 (see chapter 4.2.6) in addition to the ΔΔ excitation. From the PDG-compilation we see that a possible resonance candidate is Δ(1600) (Fig. 4.24).
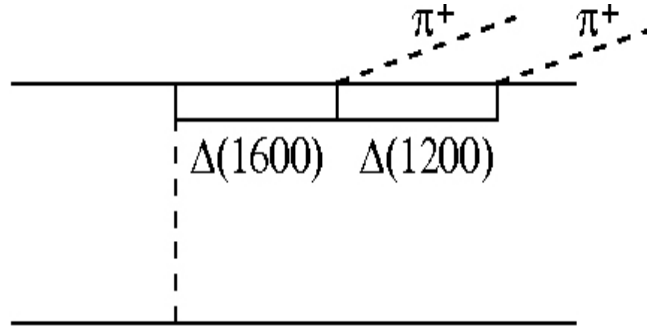
Figure 4.24 *Feynman diagram for the $pp \to nn\pi^+\pi^+$ channel describing $\pi\pi$ production via the excitation of the $\Delta(1600)$ and its decay into $\Delta(1600) \to \Delta(1232)\pi \to N\pi\pi$.*

Although we observe no enhancement at low invariant mass $M_{\pi^+\pi^+}$, this observation unfortunately can not be an unambiguous proof against Bose-Einstein correlation in $\pi^0\pi^0$ production. Nevertheless, there are at least two arguments, which are against independent decays of Δs excited in the $pp \to pp\pi^0\pi^0$ reaction:

• In the $pp \to nn\pi^+\pi^+$ reaction two π^+ are dominantly produced in successive decays of $\Delta(1600)$ and $\Delta(1232)$ excited from the same nucleon. Since we did not observe a signature of BEC, we concluded, that there was some correlation between these two decays. Indeed, as soon as $\Delta(1600)$ decayed and the first π^+ carried away some energy, the energy allowed for $\Delta(1232)$ is determined. In the case of $\pi^0\pi^0$ production two Δs are excited in each of the two nucleons simultaneously. As soon as the first Δ has decayed, the energy, which is available in the decay of the second one, is determined. Since two pion sources are produced in this reaction, due to conservation laws always strong energy-momentum correlations between both decays are established.

• The enhancement, observed at low invariant mass $M_{\pi^0\pi^0}$ looks very similar to the enhancement at low invariant mass $M_{\pi^0\pi^0}$, which has been observed in the reactions $pn \to d\pi^0\pi^0$ and $pd \to {}^3He\pi^0\pi^0$ and is known as the ABC effect. The data analyses [51, 55] show that the ABC effect is associated with $\Delta\Delta$ production and the description of the data requires a strong $\Delta\Delta$ interaction in the intermediate state.

4.2.5 ABC effect in proton-proton interaction

The ABC effect historically stands for a strong enhancement at low invariant masses $M_{\pi\pi}$ in the double-pionic fusion of deuterons and protons to ${}^3He$. Later on this effect was also observed in the fusion processes leading to d and ${}^4He$, if the pion pair was in an isoscalar state [52]. Since the effect showed up always at

beam energies corresponding to the excitation of two Δs, the ABC effect was interpreted by *t*-channel ΔΔ excitation, which should lead to both a low-mass and a high-mass enhancement in isoscalar $M_{\pi\pi}$ spectra [53]. In fact, the missing momentum spectra from inclusive measurements have been in support of such a prediction. New exclusive data obtained at CELSIUS-WASA [54] show that the conventional ΔΔ explanation can not describe the experimental data. The data require a very strong ΔΔ interaction, parameterised as a quasi-bound ΔΔ state [51, 54].

Fig. 4.25 presents the $M_{\pi\pi}$ invariant mass spectra for three reactions: $pp{\rightarrow}pp\pi^0\pi^0$, $pn{\rightarrow}d\pi^0\pi^0$ and $pd{\rightarrow}{}^3He\pi^0\pi^0$. The last two are reactions, where the ABC effect has been observed. The enhancement obtained for the $pp{\rightarrow}pp\pi^0\pi^0$ reaction is much smaller than in the double-pion fusion reactions. Nevertheless we observe a similar tendency in shape.

Fig. 4.26 shows the comparison of $pp{\rightarrow}pp\pi^0\pi^0$ data with a model including the ΔΔ excitation with the same interaction strength between the two Δs, as it has been adjusted to describe double-pionic fusion data [51].
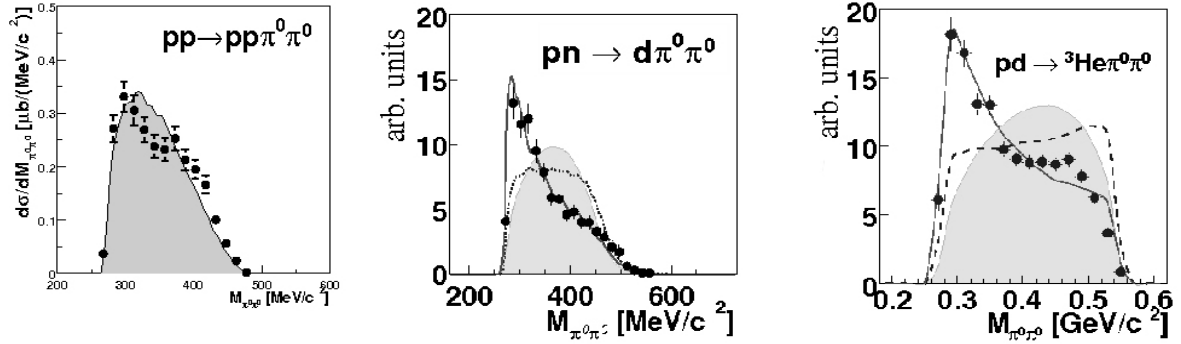
Figure 4.25 *Invariant mass $M_{\pi\pi}$ for $pp{\rightarrow}pp\pi^0\pi^0$ (T_p=1.1 GeV, left), $pn{\rightarrow}d\pi^0\pi^0$ (T_p=1.03 GeV, middle) and $pd{\rightarrow}{}^3He\pi^0\pi^0$ (T_p=0.9 GeV, right) in the region of the ΔΔ excitation. The grey area denotes phase space, the lines denote calculations of ΔΔ excitation in the intermediate state with (solid) and without (dashed) a strong interaction between the two Δs.*

The model with a quasi-bound ΔΔ state describes very well the isoscalar two-pion production in cases, where bound nuclear systems are formed in the final state. As we see from Fig. 4.26 it fails, however, to describe the isoscalar two-pion production in the 'free' case, when the two nucleons remain unbound. This result can be easily understood, if we look on the formula, which has been used for the quasi-bound ΔΔ system:

$$A \sim F(q_{\Delta\Delta})D_{\Delta_1}D_{\Delta_2} \qquad\qquad 4.7$$

where D_{Δ_1} and D_{Δ_2} are two Δ propagators, describing the ΔΔ excitation. These two terms create both low- and high-invariant mass enhancements. Since in the

exclusive ABC data the high-mass enhancement is absent, i.e. the configuration with the two pions moving with big relative momenta is suppressed, the form factor $F(q_{\Delta\Delta})$ has been inserted to reproduce this behaviour. $F(q_{\Delta\Delta})$ was chosen to be of monopole type and depends on the relative momentum $q_{\Delta\Delta}$ between two Δs. Since the two nucleons of the two Δs are confined by the nuclear bound state condition, we have $q_{\Delta\Delta} \approx q_{\pi\pi}$ and the two pions are forced to have small relative momentum. Thus, this form factor is reflected directly in $M_{\pi\pi}$ spectra and causes there the ABC effect by suppressing of the high-mass region.
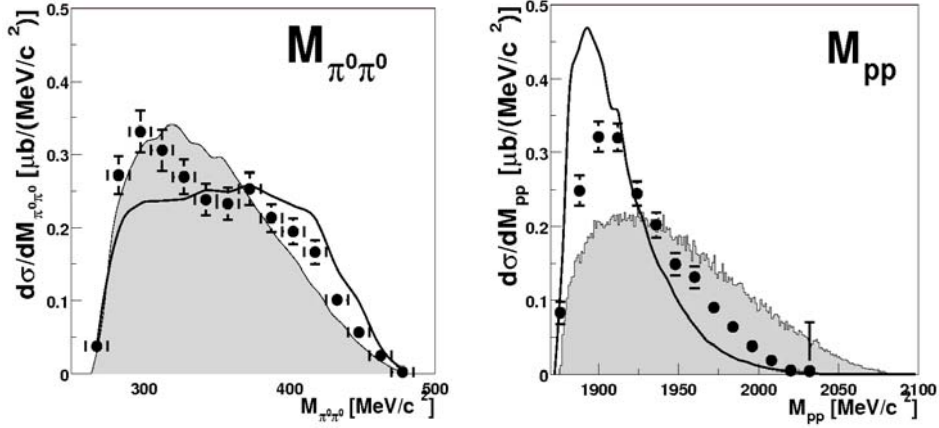
Figure 4.26 *Invariant masses $M_{\pi\pi}$ and M_{pp} for $pp \to pp\pi^0\pi^0$ at $T_p=1.1$ GeV. The grey area denotes phase space. Solid lines are calculations of $\Delta\Delta$ excitation in the intermediate state with an interaction between the two Δs as used in Ref. [51] for the explanation of the ABC effect.*

In case of the $pp \to \Delta\Delta \to pp\pi^0\pi^0$ reaction two nucleons in the final state are not bound and they carry the main Δ-momentum, therefore the form factor $F(q_{\Delta\Delta})$ influences mostly the nucleon-pair, enhancing the proton-pair with small relative momentum, i.e. with low invariant mass.

4.2.6 Isospin decomposition

The Valencia model calculations describe $\pi^+\pi^-$ and $2\pi^0$ production data at low energy ($T_p \leq 0.9$ GeV) quite well both in total and differential cross sections, but discrepancies increase with increasing energy. Particular problems constitute:
• the shape of the total $pp\pi^0\pi^0$ cross section (Fig 4.27, top right);

• the big ratios $\dfrac{\sigma(pp\pi^+\pi^-)}{\sigma(pp\pi^0\pi^0)}$ up to 10 at energies more than 1 GeV (fig 4.27);

• differential cross sections of the reaction $pp\pi^0\pi^0$ at energies more than 1 GeV, especially $M_{\pi\pi}$ and $\delta_{\pi\pi}$ distributions (Fig 4.1);

- the big discrepancy in calculated and measured total cross sections for the reaction $nn\pi^+\pi^+$ (Fig 4.27, bottom left).
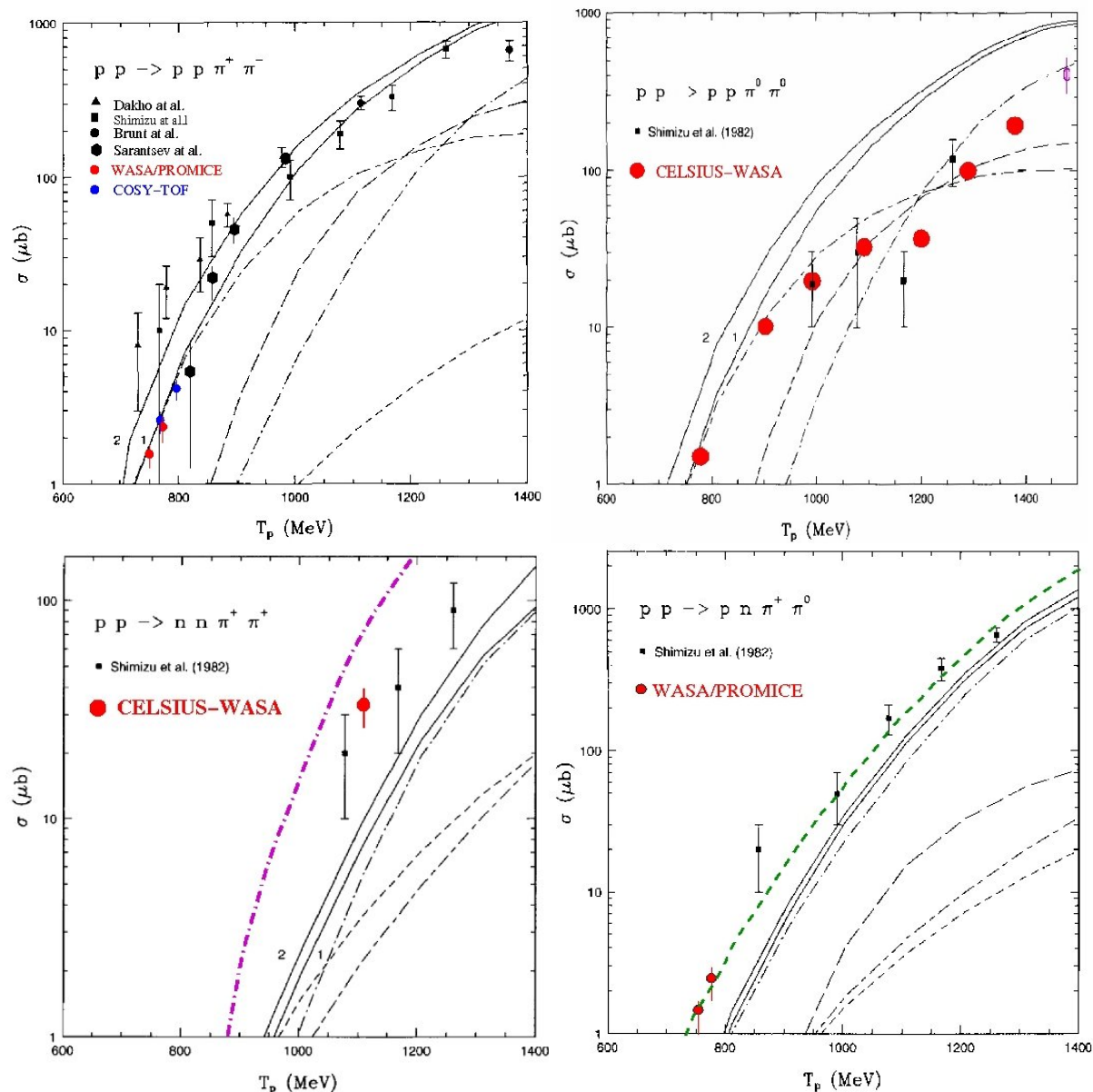

Figure 4.27 *Total cross section as a function of proton kinetic beam energy in the laboratory frame. The black line definitions are taken from [8]: solid are full calculations of the Valencia model, long-short-dashed line is decay $N^* \rightarrow N(\pi\pi)^{I=0}_{S-vawe}$; long-dashed line is $N^* \rightarrow \Delta\pi$; dash-dotted line is $\Delta\Delta$ excitation mechanisms; short-dashed line is a contribution of the non-resonant terms. The green shot-dashed line in (bottom right) is our estimation of the total cross section of the reaction $pp \rightarrow pn\pi^+\pi^0$ which includes the contribution from the decay of $\Delta(1600)$. The magenta dash-dotted line in (bottom left) is our estimation of the contribution of the decay $\Delta(1600)$.*

As a next attempt to understand our data we made an isospin decomposition analysis and compared the different isospin contributions with the Valencia model predictions.

The isospin decomposition is a model-independent method - it does not depend on the reaction dynamics, but only on isospin combinations of the initial and final states of the system. The total cross sections for the different two pion reaction channels can be expressed in terms of the isospin matrix elements $M_{I_f I_{\pi\pi} I_i}$, where I_i denotes the initial isospin of the two protons, I_f denotes the final isospin of two nucleons and $I_{\pi\pi}$ denotes the isospin of the produced pion pair. Unfortunately all two-pion production reactions possible in proton-proton and proton-neutron collisions lead to only six independent total cross sections with seven unknowns [56]. In Ref. [49] one has tried to make an isospin decomposition by fitting data for three reactions measured at several energies. Since the prediction obtained in Ref. [49] for total cross section of the reaction $pp\pi^0\pi^0$ does not agree with the our measurements, we have repeated the isospin decomposition using our new data as well as previous data from [3] and taking in account the relations between isospin amplitudes in case of specific resonance excitations. We started out with considering the following three reactions:

$$pp \rightarrow nn\pi^+\pi^+$$
$$pp \rightarrow pp\pi^0\pi^0$$
$$pp \rightarrow pp\pi^+\pi^-$$
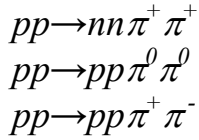
and used the reaction $pp \rightarrow pn\pi^+\pi^0$ for check/prediction. The total cross sections for these reactions can be written as:

$$\sigma_{nn\pi^+\pi^+} = \frac{3}{20}|M_{121}|^2 \tag{4.8}$$

$$\sigma_{pp\pi^0\pi^0} = \frac{1}{60}|M_{121} - \sqrt{5}M_{101}|^2 = \frac{1}{60}|M_{121}|^2 + \frac{1}{12}|M_{101}|^2 - \frac{1}{\sqrt{180}}|M_{121}||M_{101}|\cos\varphi \tag{4.9}$$

$$\sigma_{pp\pi^+\pi^-} = \frac{1}{120}|M_{121} + 2\sqrt{5}M_{101}|^2 + \frac{1}{8}|M_{111}|^2 = \frac{1}{120}|M_{121}|^2 + \frac{1}{6}|M_{101}|^2 + \frac{1}{8}|M_{111}|^2 + \frac{1}{\sqrt{180}}|M_{101}||M_{121}|\cos\varphi \tag{4.10}$$

In this decomposition all matrix elements are complex numbers. However, only the two amplitudes M_{101} and M_{121} can interfere with a relative phase φ, otherwise only the moduli of the matrix elements enter in formulas (4.9) and (4.10). We see that there are two possibilities to obtain a large difference in the total cross sections of $pp \rightarrow pp\pi^+\pi^-$ and $pp \rightarrow pp\pi^0\pi^0$ channels:
first, by a large $|M_{111}|$ contribution. But in the framework of the Valencia model there is no source for a big M_{111} amplitude, since the Roper excitation, which is the leading process in the near-threshold region [5, 8] contributes only a tiny

fraction of its strength to $|M_{111}|$ and the $\Delta\Delta$ process, which is the leading process at higher energies does not contribute at all to $|M_{111}|$.

Another possibility to increase the difference between cross section (4.9) and (4.10) is a constructive interference for the $pp\pi^+\pi^-$ channel and a destructive for $pp\pi^0\pi^0$. In this case $\cos\varphi$ has to be positive and in order to obtain the maximum in this difference $\cos\varphi$ has to be equal 1. This assumption means that M_{121} and M_{101} amplitudes are in phase.

As pointed out above, the Valencia model largely underestimates the total cross section for the reaction $pp\rightarrow nn\pi^+\pi^+$. From the experimental data the matrix element M_{121} can be easily calculated from the total cross section of this reaction. Using then the deduced $|M_{121}|$ and $\cos\varphi=+1$ one can deduce the value of the matrix element M_{101} (Fig 4.28) from the experimental results for the reaction $pp\rightarrow pp\pi^0\pi^0$.
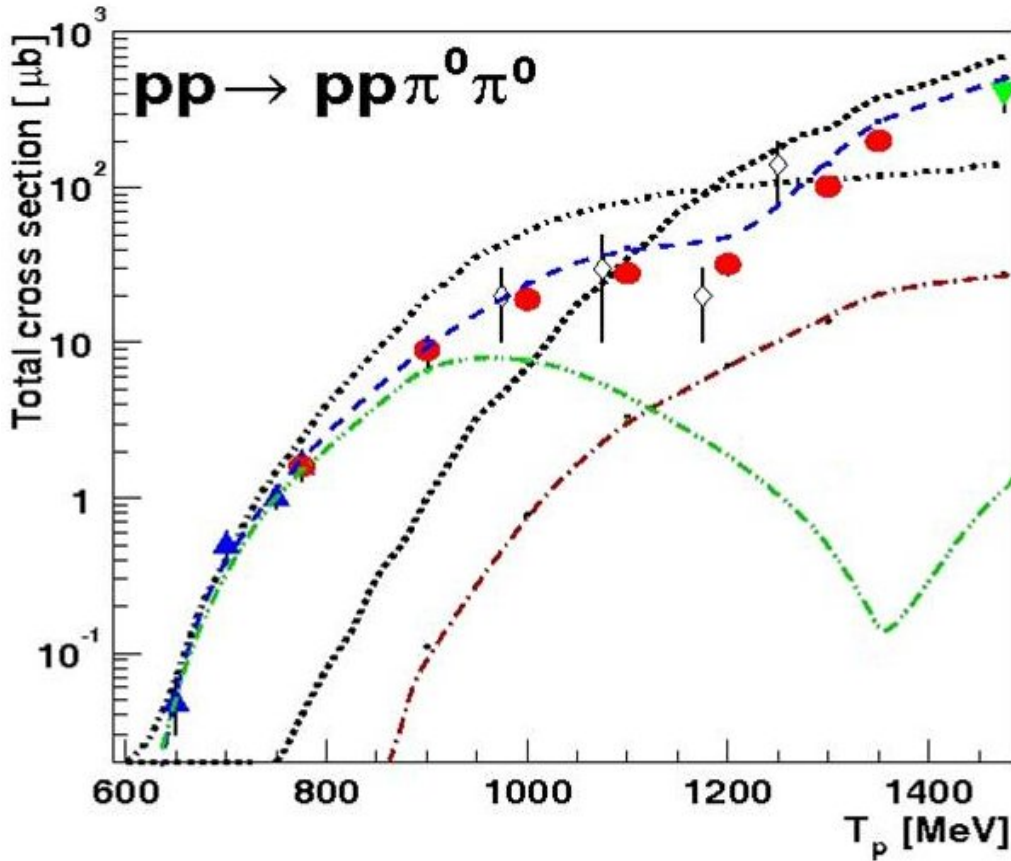
Figure 4.28 *Total cross section as a function of the energy: the black short-dashed-dotted line is a Valencia model calculations for Roper excitation; the black short-dashed line is a Valencia model calculations for two delta excitations; the blue dashed line is a cross section due to matrix element M_{101} from isospin decomposition; the brown dash-dotted line is a cross section due to matrix element M_{121} from isospin decomposition; the green dash-two-dotted line is a cross section due to N^*(the Roper and D_{13}) excitation from isospin decomposition.*

Next we investigated, which resonances may contribute to the matrix element M_{101}. Only Roper, $\Delta\Delta$ and $D_{13}(1520)$ excitation have isoscalar amplitudes. But $D_{13}(1520)$ has a rather high mass and a narrow width, therefore it can contribute significantly only at energies above 1.3 GeV. So we have assumed that the matrix element M_{101} has contributions for our energy range only from the matrix element M_{101}^{Roper} from Roper excitation and the matrix element $M_{101}^{\Delta\Delta}$ from $\Delta\Delta$-excitation.

Our most crucial assumption concerns the absolute value of matrix element $M_{101}^{\Delta\Delta}$. One can see that Valencia calculations for $\Delta\Delta$ are very close to the data at energies more than 1.2 GeV (Fig. 4.27, top right), therefore we have assumed that these calculations are correct at least with regard to the energy dependence. Next step was to understand, which relative phase can be between M_{101}^{Roper} and $M_{101}^{\Delta\Delta}$.

To answer this question we decided to compare the differential cross sections with the calculations for two limiting cases:

- M_{101}^{Roper} and $M_{101}^{\Delta\Delta}$ have the same phase and
- the relative phase between M_{101}^{Roper} and $M_{101}^{\Delta\Delta}$ is 180^0.

As a check the data at 0.895 GeV were chosen, since at this energy the contribution from the matrix element M_{121} is still tiny. As one can see in Fig. 4.29, the data clearly prefer M_{101}^{Roper} and $M_{101}^{\Delta\Delta}$ to be in phase.
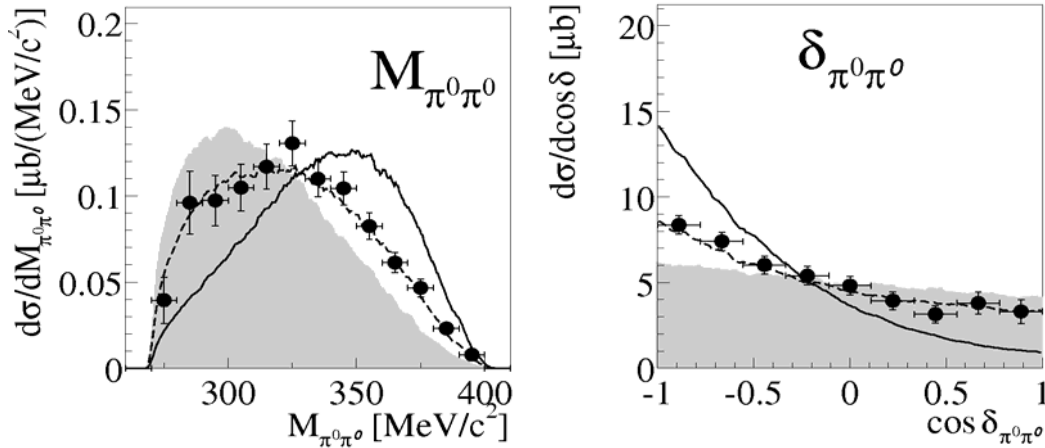
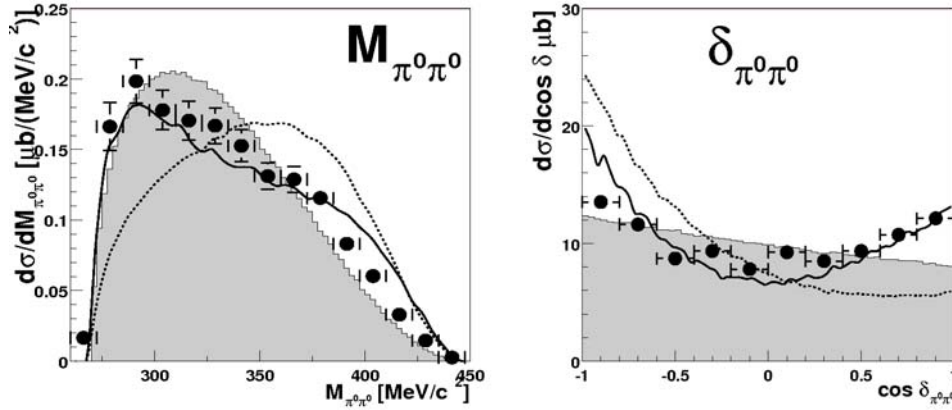Figure 4.29 *Invariant mass and opening angle between two pions in cm system at $T_p=0.895$ GeV. The solid line corresponds to calculations in which the Roper and $\Delta\Delta$ excitation matrix elements have the relative phase 180^0; short-dashed one corresponds to calculations in which the Roper and $\Delta\Delta$ matrix elements have the same phase.*

In Fig. 4.28 the green dashed line represents the cross section $\sigma_{101}^{N^*}$ deduced from the σ_{101}^{tot} and $\sigma_{101}^{\Delta\Delta}$ as obtained by isospin decomposition. At low energy this cross section presumably corresponds to the Roper excitation. However, in contrast to the Valencia model prediction, it does not rise permanently, but only up to some

maximum value at about 1 GeV and then it decreases. At energies above 1.3 GeV a rise of the cross section is likely to be due to the $D_{13}(1520)$ excitation.

To check this solution for further consistency we have considered the data at the energies 1 and 1.1 GeV, since at these energies already a significant difference appears between Valencia calculations and data. At the same time the contribution in total cross section from the matrix element M_{121} is still relatively small. In Fig. 4.30 and 4.31 one can see that the isospin decomposition gives a solution for the absolute contribution from Roper resonance in total cross section, which is much closer to the data.
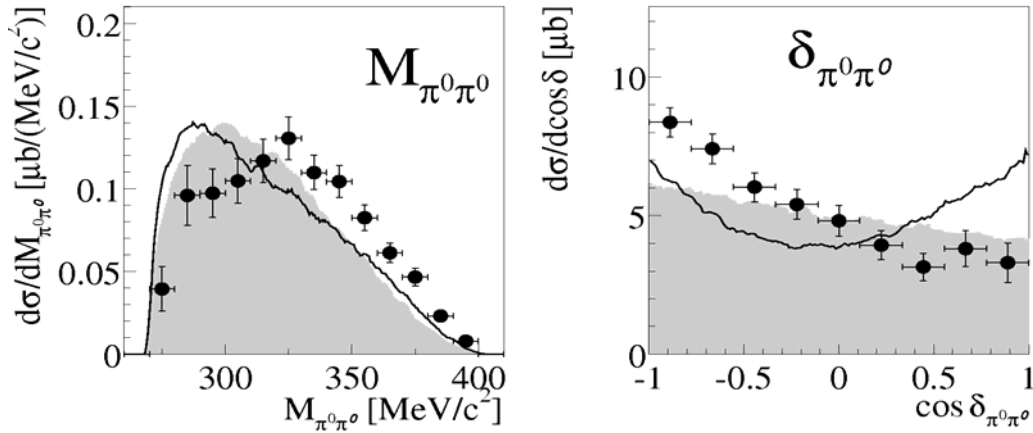

Figure 4.30 *Invariant mass and opening angle between two pions in cm system at T_p= 1.0 GeV. The dotted line corresponds to the calculations of the original Valencia model; the solid one corresponds to the calculation 'modified' Valencia model in which the contribution from the Roper excitation was decreased according to the isospin decomposition in Fig. 4.28.*
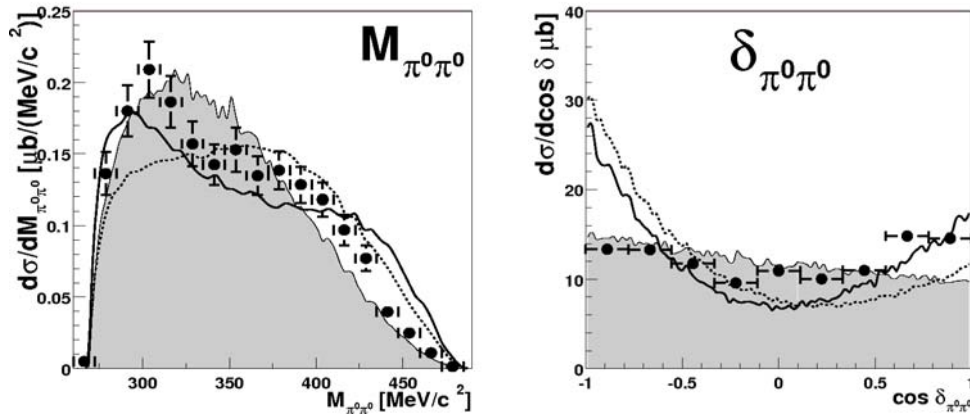
Figure 4.31 *The same as Fig. 4.30, but for T_p= 1.1 GeV.*

After we have convinced ourselves that we have now the proper solution for the Roper and $\Delta\Delta$ contributions, we try now to understand which reaction mechanisms could increase $|M_{121}|$ in order to reproduce the experimental $\pi^+\pi^+$

total cross section. First of all, only resonances with isospin 3/2 can give contributions to M_{121}. Hence we have considered three hypotheses:

- $M_{121} = M_{121}^{\Delta\Delta}$, i.e. the main contribution comes from $\Delta\Delta$ and the Valencia model has simply underestimated it by factor 4,

- $|M_{121}| = |\sum M_{121}(I = 3/2)|$, i.e. the main contribution is not from $\Delta\Delta$, but from the excitation of other resonances with isospin 3/2, which are not included in the Valencia model,

- $|M_{121}| = |M_{121}^{\Delta\Delta} + \sum M_{121}(I = 3/2)|$, at least two production mechanisms contribute in the total matrix element: the excitation of $\Delta\Delta$ and excitation of other resonances with isospin 3/2.

If the first hypothesis is correct, then the total contribution from $\Delta\Delta$ has to be increased by a factor of 4 in all cross sections, since the isospin decomposed matrix element of one specific resonance excitation are strictly correlated by isospin coupling coefficients. E.g., for the relation $M_{101}^{\Delta\Delta}$ and $M_{121}^{\Delta\Delta}$ we have [57]:

$$M_{101}^{\Delta\Delta} = -\sqrt{5}M_{121}^{\Delta\Delta}$$
4.11

In order to keep the total $\pi^0\pi^0$ cross section at the experimental value in this case, one needs to decrease the contribution from the Roper correspondingly. One can see that the data at 0.895 GeV no longer agree with the calculations for this hypothesis (Fig. 4.32).

Figure 4.32 *Invariant mass and opening angle between two pions in cm system at T_p=0.895 GeV. The solid line corresponds to calculations in which the contribution from $\Delta\Delta$ excitation was increased according to the total cross section of the reaction $pp\rightarrow nn\pi^+\pi^+$.*

In the second hypothesis, again taking into account the relation (4.11), we would not see any contribution from two deltas at high energy. But we are sure, that in the reaction $pp\rightarrow pp\pi^+\pi^-$ at 1.36 GeV we see simultaneously two deltas in the invariant mass spectra of π^+p and π^-p (Fig. 4.19)

So only the third hypothesis is left, i.e. we have to understand which additional resonance with isospin 3/2 can contribute. According to the Valencia model calculation the decay $\Delta(1232) \rightarrow \Delta(1232)\pi$ has a tiny amplitude due to the small phase space allowed for this decay, so we have to reject the $\Delta(1232)$ as the major source for M_{121}. The next resonance with isospin 3/2 is the $\Delta(1600)$. From our point of view it is a very promising candidate:
- the fraction of the decay $\Delta(1600) \rightarrow \Delta(1232)\pi$ is 30-60% (PDG),
- the $\Delta(1600)$ has a very large width of ≈ 350 MeV, so it can contribute already at incoming energies of 1.1-1.2 GeV.

We also see that $M_{121}^{\Delta\Delta}$ and $M_{121}^{\Delta(1600)}$ have to be in antiphase to each other, since:
- the relative phase between $M_{121}^{\Delta\Delta}$ and $M_{101}^{\Delta\Delta}$ is 180^0, see (4.11),
- the matrix elements $M_{101}^{\Delta\Delta}$ and M_{101}^{Roper} have the same phase, so since the relative phase is $\varphi = 0$, the total M_{101} amplitude has a relative phase 180^0 with $M_{121}^{\Delta\Delta}$,
- the total matrix element M_{101} has the same phase as the total matrix element M_{121}. Hence the total M_{121} has the relative phase 180^0 with the matrix element $M_{121}^{\Delta\Delta}$.

Therefore, only one solution can satisfy these requirements:

$$| M_{121} |=| M_{121}^{\Delta(1600)} | - | M_{121}^{\Delta\Delta} | \qquad 4.12$$

Fig 4.27 (bottom left) exhibits the thus deduced $nn\pi^+\pi^+$ cross section due to the $\Delta(1600)$ excitation (magenta dash-dotted line). Next we check this assumption by comparing differential cross sections for the reaction $pp \rightarrow nn\pi^+\pi^+$ with a calculation, where we have substituted in graph (9) of Ref. [8] the decay amplitude $\Delta(1232) \rightarrow \Delta(1232)\pi$ with mass and width of the first $\Delta(1232)$ by the mass and width of the $\Delta(1600)$ calculating thus the decay $\Delta(1600) \rightarrow \Delta(1232)\pi$. This amplitude has been also complemented by a normalizing factor in order to reproduce the experimental total cross section. Though the statistics collected for the reaction $pp \rightarrow nn\pi^+\pi^+$ does not yet allow to confirm confidently our conclusion about a significant contribution of the $\Delta(1600)$, the data are certainly in favor of this solution (see Appendix G).

There is a further possibility to check the correctness of including $\Delta(1600)$ in the set of the main two-pion production mechanisms: the study of the reaction $pp \rightarrow pn\pi^+\pi^0$. The calculations of the Valencia model give much lower total cross sections than obtained in the experiment. This problem can be solved by including the $\Delta(1600)$ as a further contribution to the matrix elements M_{121}, M_{111} and M_{110} (see Fig. 4.27, bottom right and Ref. [57]).

5 Summary and outlook

The first exclusive measurements of the $pp \to pp\pi^0\pi^0$ reaction in the energy range from threshold up to 1.3 GeV and of the $pp \to nn\pi^+\pi^+$ reaction at T_p=1.1 GeV have been performed at CELSIUS-WASA. In the energy range from 1 GeV to 1.3 GeV the total cross sections of our data are in good agreement with previous bubble-chamber data, which however are of low statistics.

The data have been compared with the Valencia model calculations, which up to present constitute the state-of-the-art calculations for the two-pion production in nucleon-nucleon collisions. From this comparison the following conclusions are obtained:

• At low energies up to T_p=0.9 GeV the $\pi^0\pi^0$ data both in the total cross sections and in the differential ones confirm the Valencia model predictions that the main contribution to the reaction results from the Roper resonance excited by σ-exchange in the NN collision process.

• The analysis of the near-threshold $\pi^0\pi^0$ production, where the differential observables are exceptional sensitive to the interference between the two Roper decay branches, provides a ratio of approximately 4:1 for the decay branching into $N\sigma$ and $\Delta\pi$ channels at a pole mass of 1371 MeV – in favor of a monopole mode interpretation of the Roper excitation. Our branching ratio at the Breit-Wigner mass of 1440 MeV (PDG nominal value) is 1:1 – in very good agreement with the value in Ref. [42], but a factor of 4 smaller than quoted in PDG [35].

• According to the isospin decomposition analysis of the $\pi^0\pi^0$ data the energy dependence of the Roper total cross sections correspond more to a s-channel excitation (increasing and then decreasing again with increasing energy) than to a t-channel excitation mechanism (slowly rising with increasing energy).

• At energies 1.2 GeV and higher, where both collision partners are expected to be excited to the Δ state, indeed, the invariant mass $M_{p\pi^0}$ spectra show clearly the Δ excitation. But in contrast to the Valencia model calculations, which assume the ΔΔ configuration in all possible spin-parity combinations, the experimental data at these energies favor the special configuration $(\Delta\Delta)_{0^+}$.

• At energies above 1 GeV the data for the $\pi^0\pi^0$ channel exhibit systematically a low-mass enhancement in the $\pi^0\pi^0$ invariant mass spectrum, which can not be explained by a high attraction in the ΔΔ system as an ABC effect, but can be reproduced by interference between the Roper and the ΔΔ excitations, if the contribution from the Roper excitation is taken from the isospin decomposition and not as obtained in the genuine Valencia calculations.

• The analysis of the $\pi^+\pi^+$ production at T_p=1.1 GeV does agree neither in the value of the total cross section nor in the shape of the differential cross sections with the Valencia model assuming a dominance of the ΔΔ excitation in the production mechanism. In order to describe the data and to explain the experimental ratio of $\dfrac{\sigma(\pi^+\pi^+)}{\sigma(\pi^0\pi^0)} \geq 1$ at beam energies above 1.1 GeV the excitation

of another resonance with isospin I=3/2 has to be included in the set of contributing $\pi\pi$ production mechanisms. We find that a good candidate for such a resonance is the $\Delta(1600)$.

Outlook

After the shutdown of CELSIUS in 2005 the WASA detector was moved to COSY (Cooler Synchrotron) in Jülich. The COSY beam energy range, the cooling and the availability of (polarized) proton and deuteron beams provide unique scientific possibilities for research in hadron physics. Very recently new data of the reaction $pn{\to}d\pi^0\pi^0$ have been taken at WASA-at-COSY with high statistics. Obtained at several energies measurements cover the full ABC resonance region. An analysis of these data undoubtedly will shed more light on this issue. Nevertheless, the ABC effect cannot be understood without the detailed analysis of the basic reaction $pn{\to}pn\pi^0\pi^0$.

Sine baryon spectroscopy is one of the key research areas at WASA-at-COSY, the investigation of the Roper resonance and its decay channels remains an interesting task, which can be performed at COSY with the close-to-4π WASA detector.

6 Appendix

In Fig. 6.1 the definitions of the different scattering angles are explained. For simplification, the example is given for the case of two particles (p_1,p_2) resulting from the reaction in the overall centre of mass system (c.m.) [9]:

- Θ_{p_1} and Θ_{p_2} are the scattering angles in the overall center of mass system;

- $\Theta_{p_1p_2}$ is the scattering angle of the centre of mass motion of both particle p_1 and p_2 in the overall centre of mass system;

- $\Theta_{p_1}^{p_1p_2}$ is the scattering angle of p_1 in the rest frame of p_1 and p_2 with respect to the beam axis (Jackson frame);

- $\hat{\Theta}_{p_1}^{p_1p_2}$ is the scattering angle of p_1 in the rest frame of p_1 and p_2 with respect to the sum momentum of p_1 and p_2 in the overall center of mass system.

Additional, we have used $\delta_{p_1p_2}$ - opening angle between p_1 and p_2 and the angle $\Delta\varphi_{p_1p_2}$ - planarity angle.
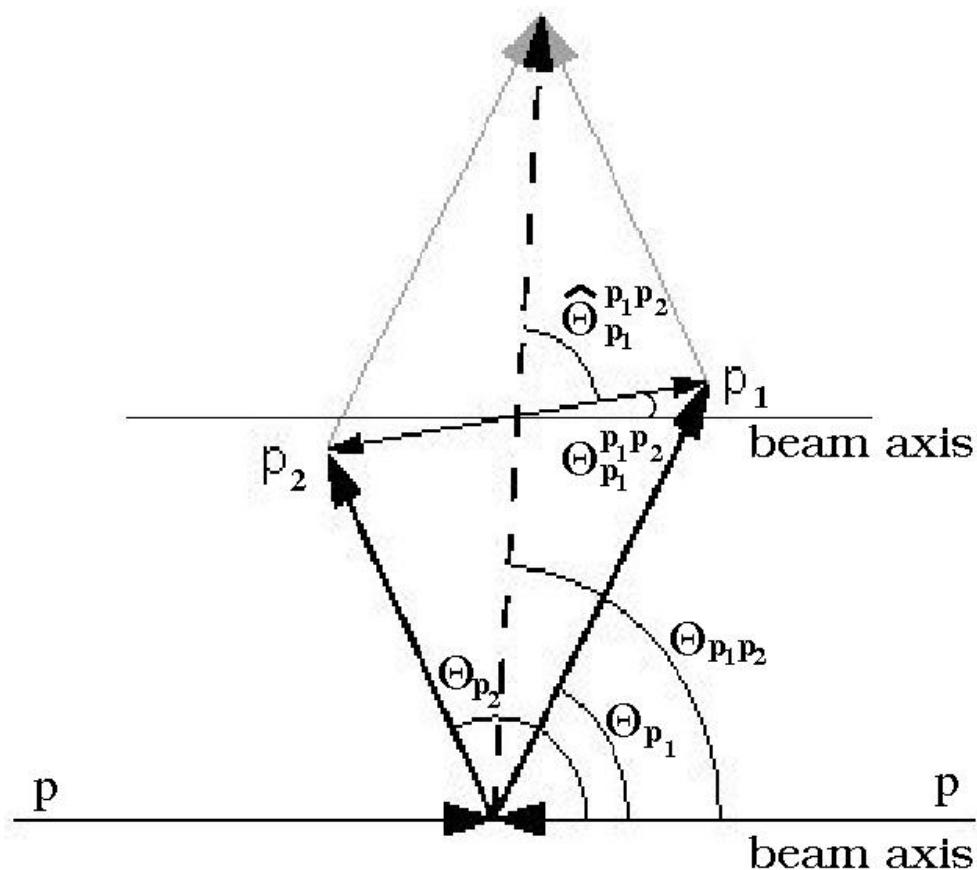
Figure 6.1 *Definition of the different scattering angles.*

Appendix A: reaction pp→ppπ⁰π⁰ at T_p=0.775 GeV

In Fig. 6.2 the grey area denotes phase space, green lines are Roper ansatz calculations (formula 4.2), the black ones are the original Valencia model calculations, the red curves are the Valencia calculations with contribution from the Roper decay branch $N^* \to \Delta\pi$ reduced by a factor of two in the amplitude. In the latter calculations the Roper mass is M=1380 MeV and the width is Γ=180 MeV. The data have been acceptance and efficiency corrected by the Roper ansatz. All theoretical curves are normalized in area to the data.
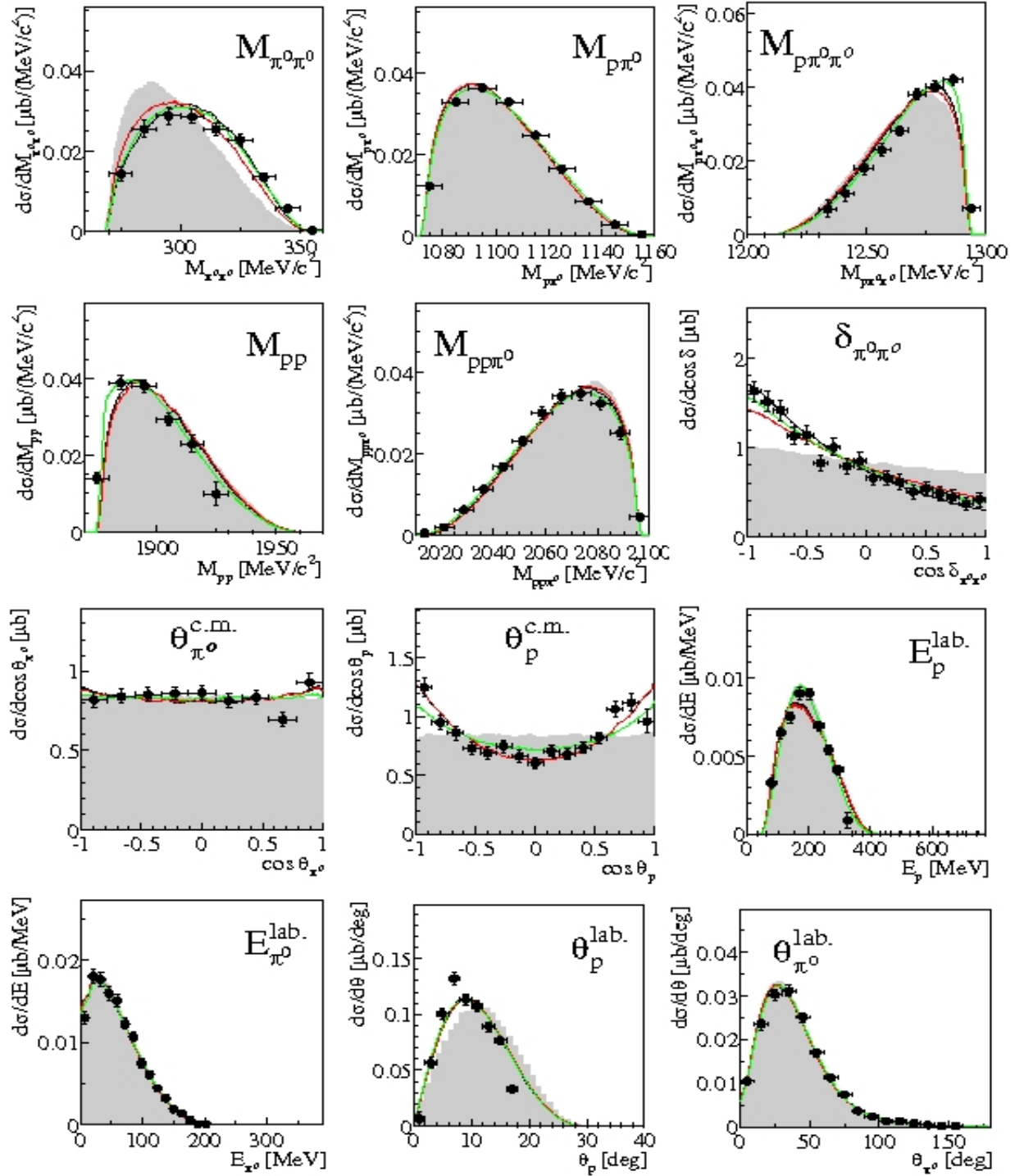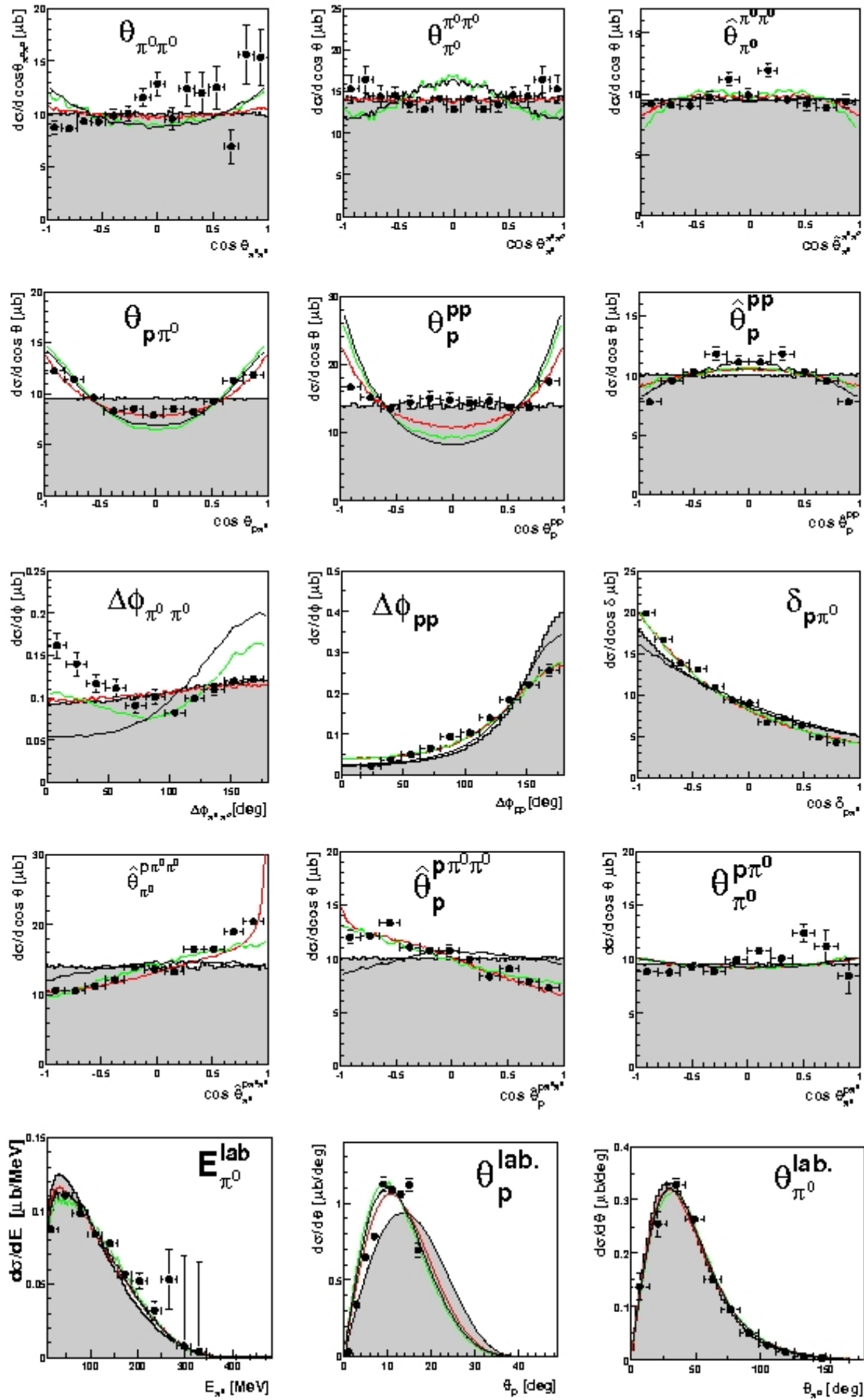

Figure 6.2
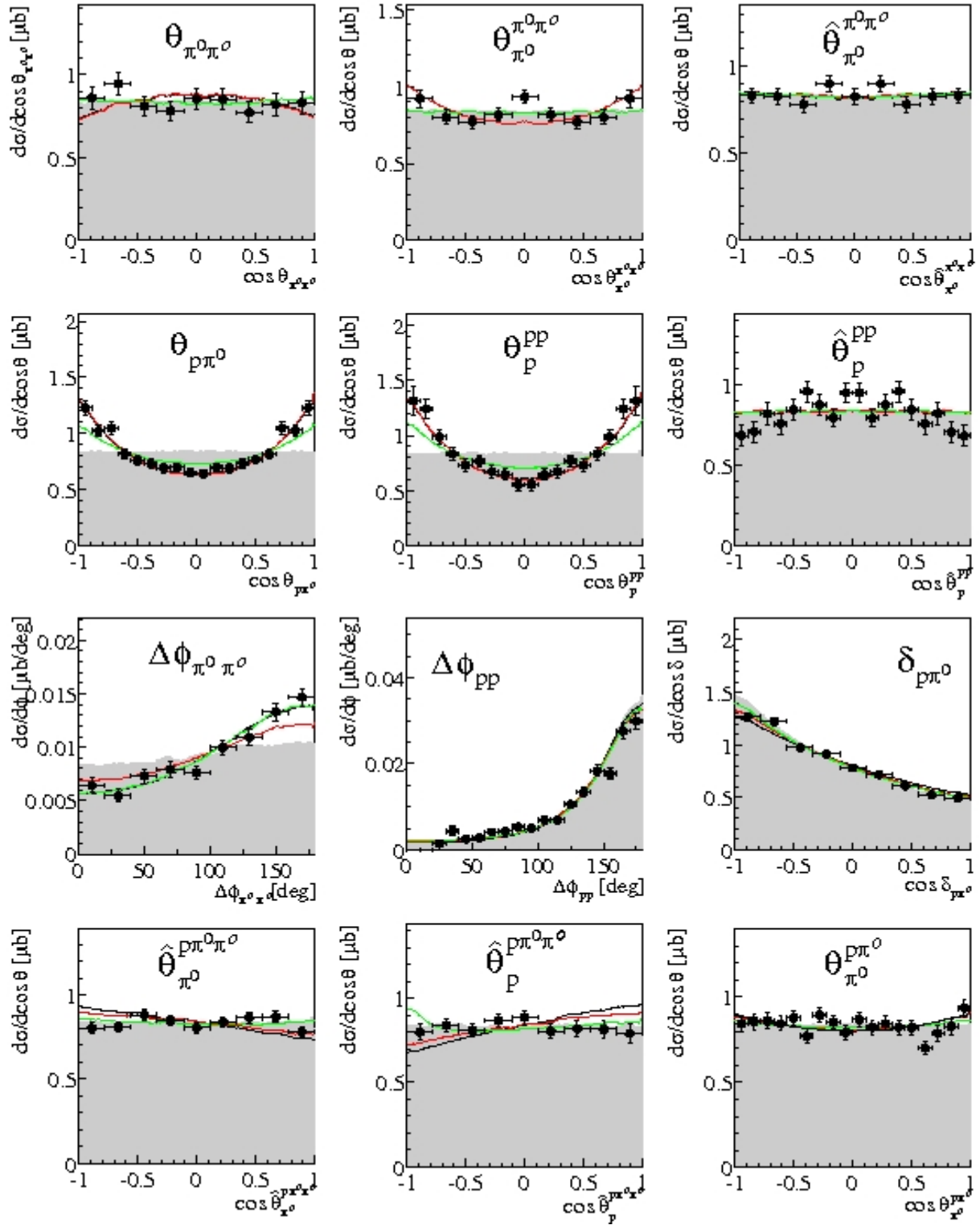
Figure 6.2 *continued*

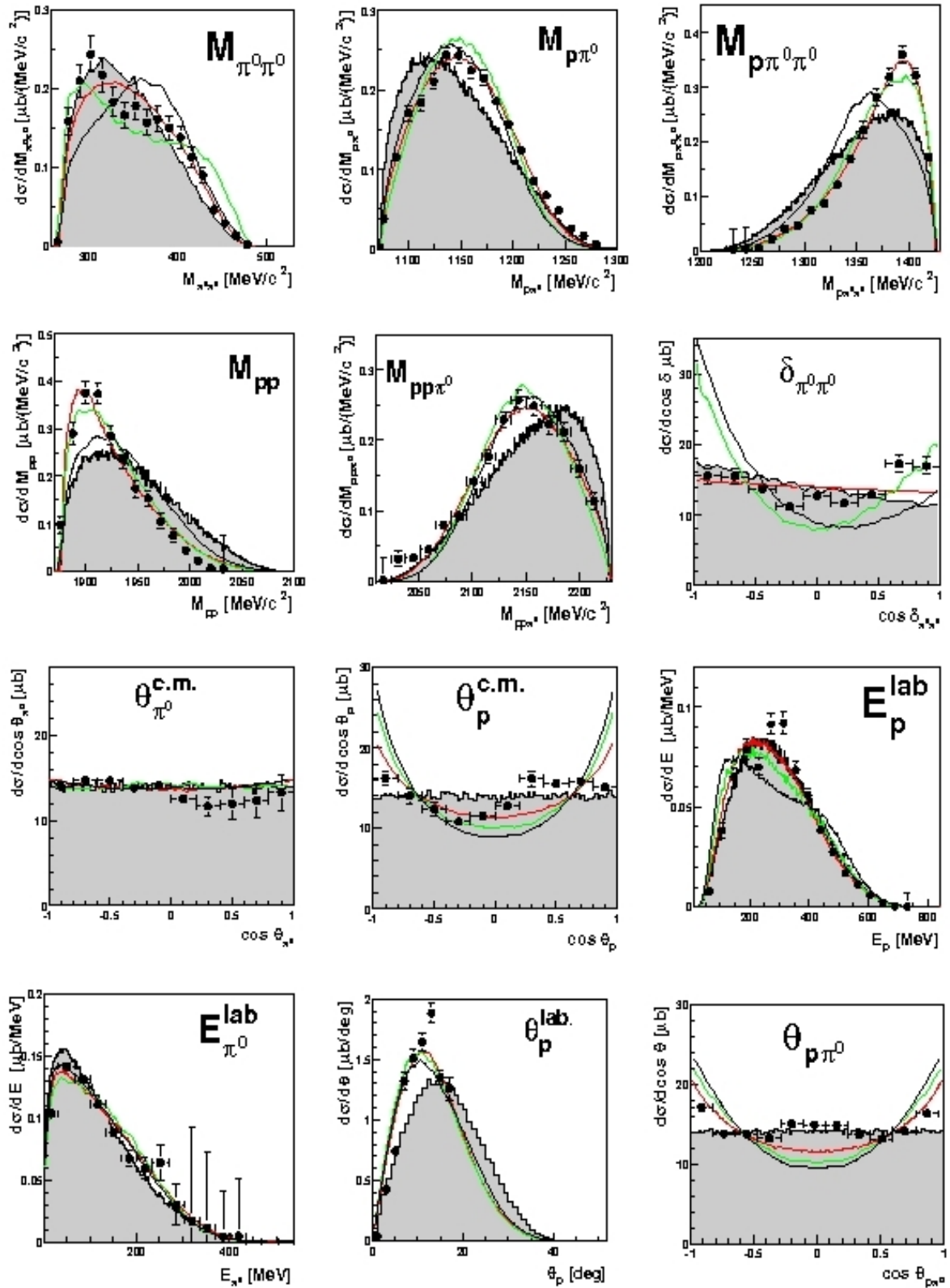# Appendix B: reaction $pp \rightarrow pp\pi^0\pi^0$ at $T_p=0.895$ GeV

.
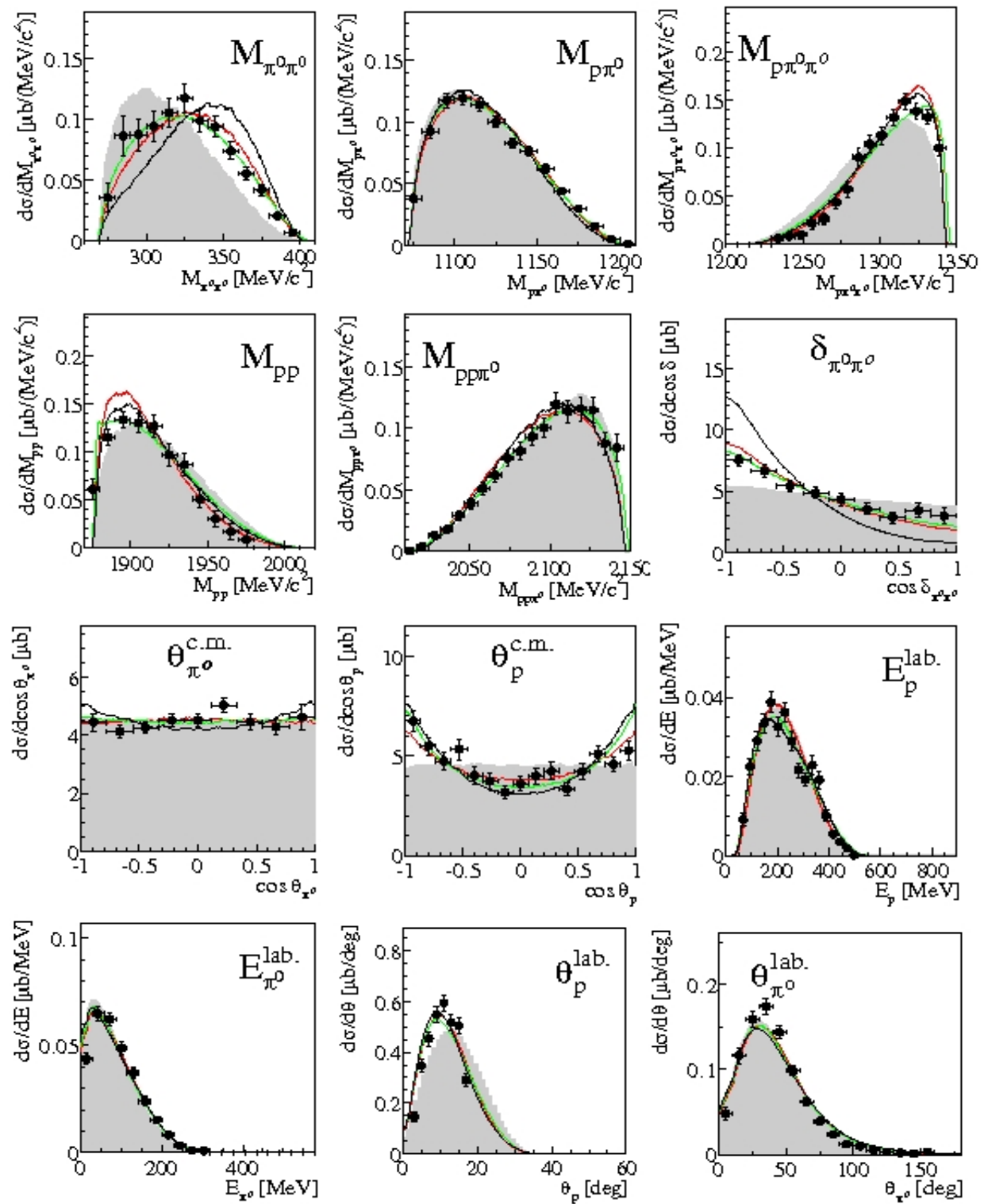
Figure 6.3 *Same as Fig. 5.2 but for $T_p=0.895$ GeV*
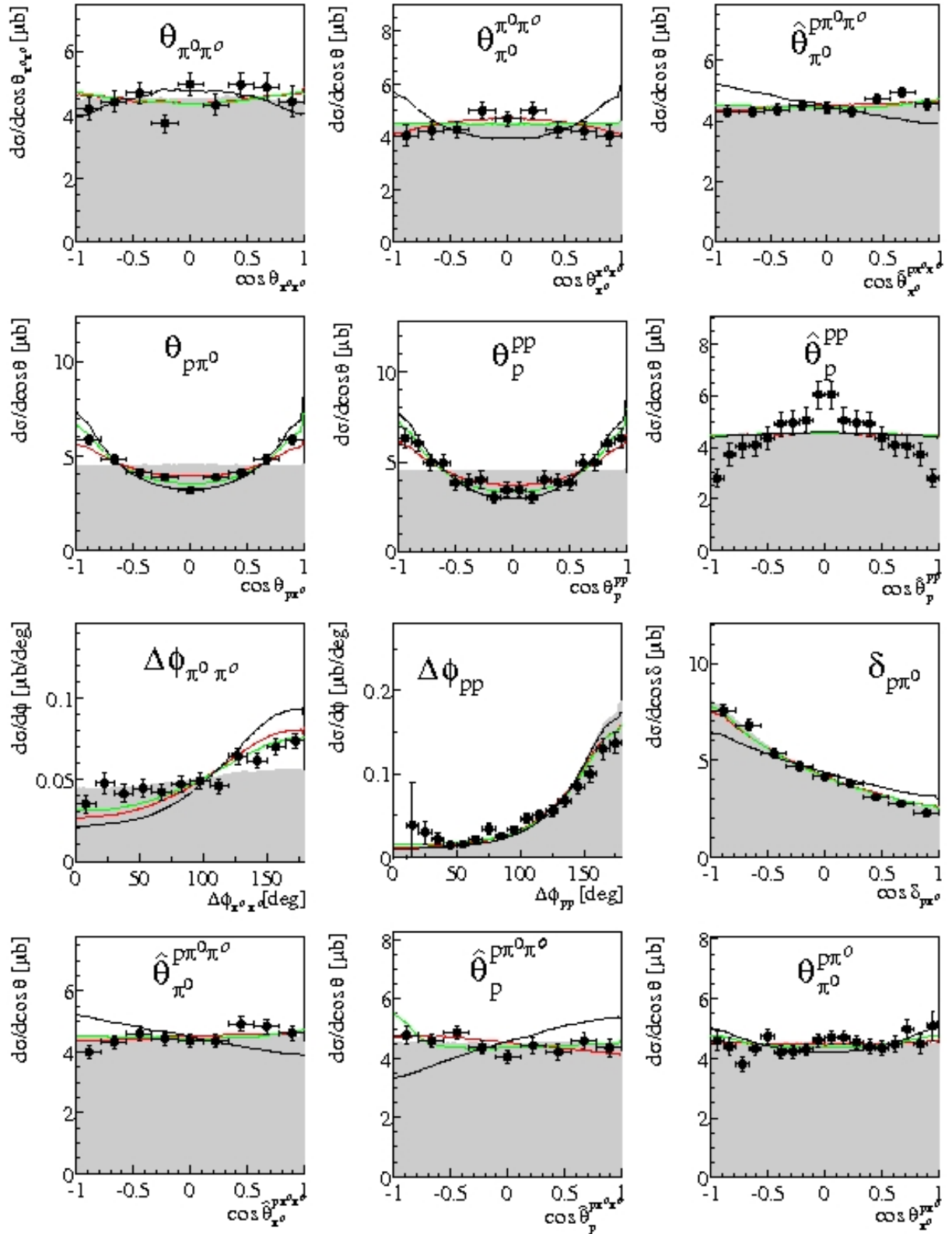
Figure 6.3 *continued*

Appendix C: reaction pp→ppπ⁰π⁰ at T_p=1 GeV

In Fig. 6.4 below the grey area denotes the phase space. Green lines are the Valencia calculations with the Roper excitation reduced according to isospin decomposition (Fig. 4.29). The black ones are the Valencia model calculations with contribution from the Roper decay branch $N^* \rightarrow \Delta\pi$ reduced by a factor of two in the amplitude. The red lines are calculations for the $(\Delta\Delta)_{0^+}$ model (this ansatz includes only two propagators for the Δ's without any angular dependence). In all calculations the Roper mass is M=1380 MeV and the width is Γ=180 MeV.

The data have been acceptance and efficiency corrected by the $(\Delta\Delta)_{0^+}$ model.

All theoretical curves are normalized in area to the data.
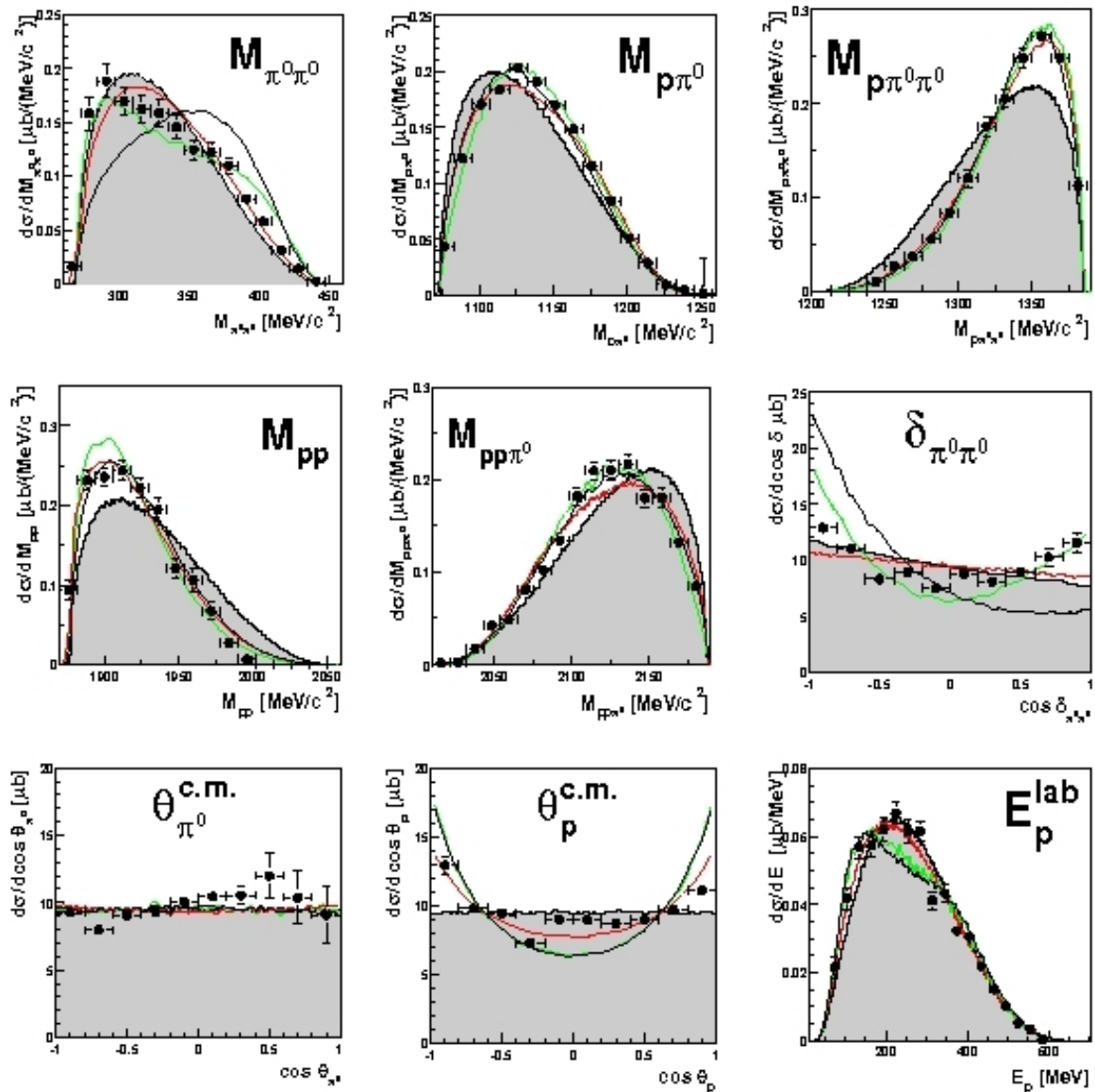
Figure 6.4

Figure 6.4 *continued*

Appendix D: reaction pp→ppπ⁰π⁰ at T_p=1.1 GeV

Figure 6.5 *Same as Fig. 5.4 but for T_p=1.1 GeV*
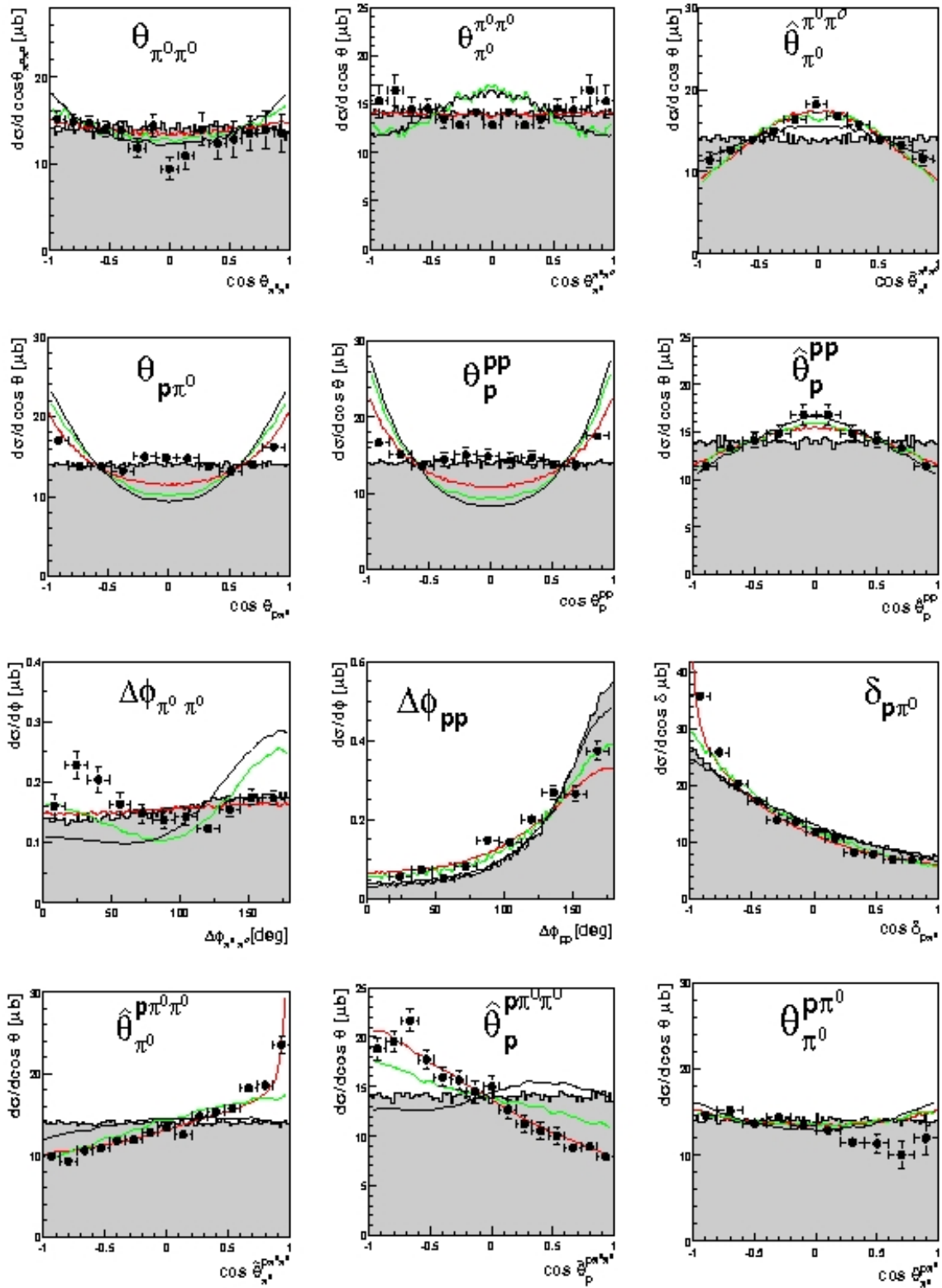
Figure 6.5 *continued*
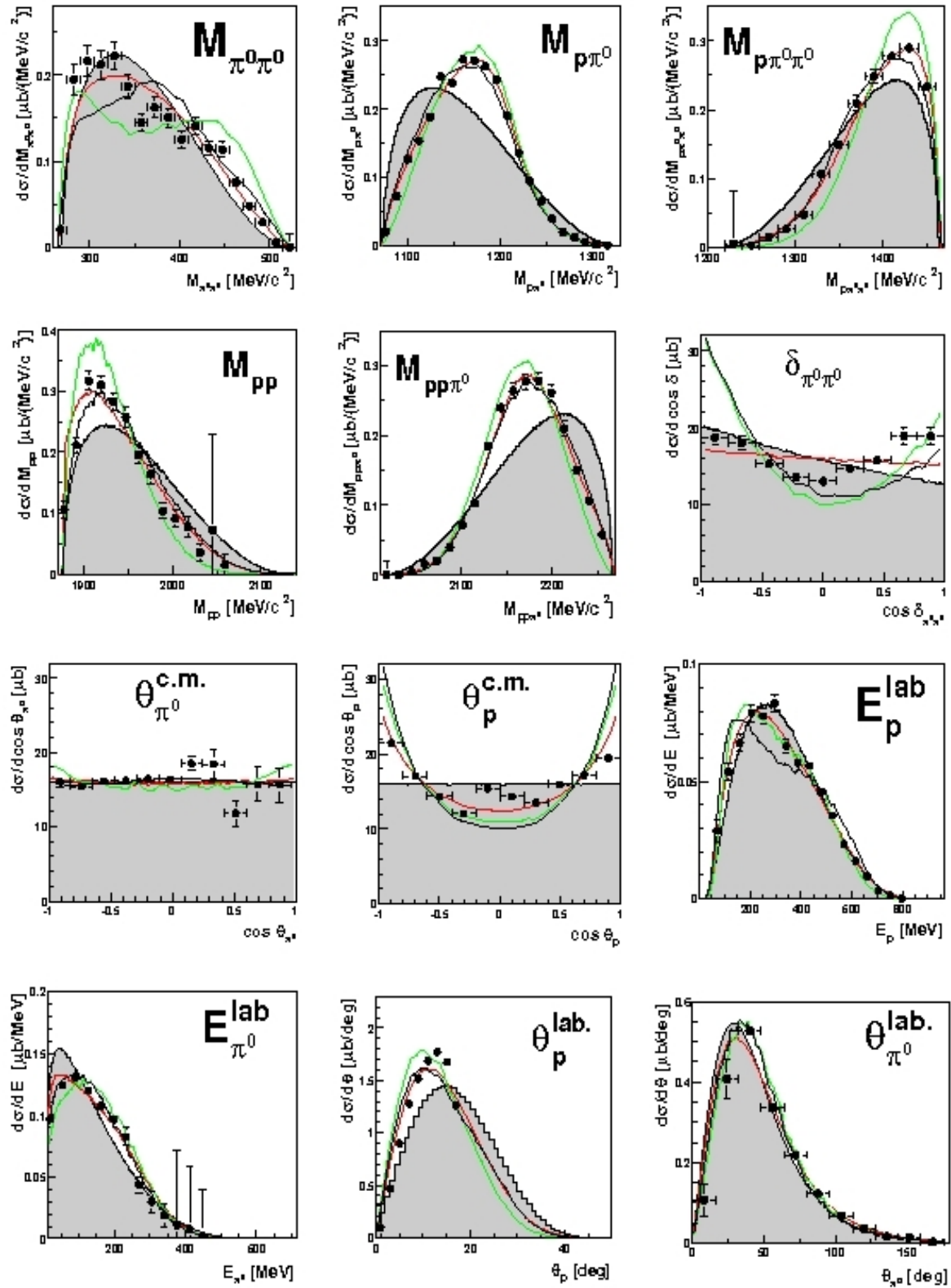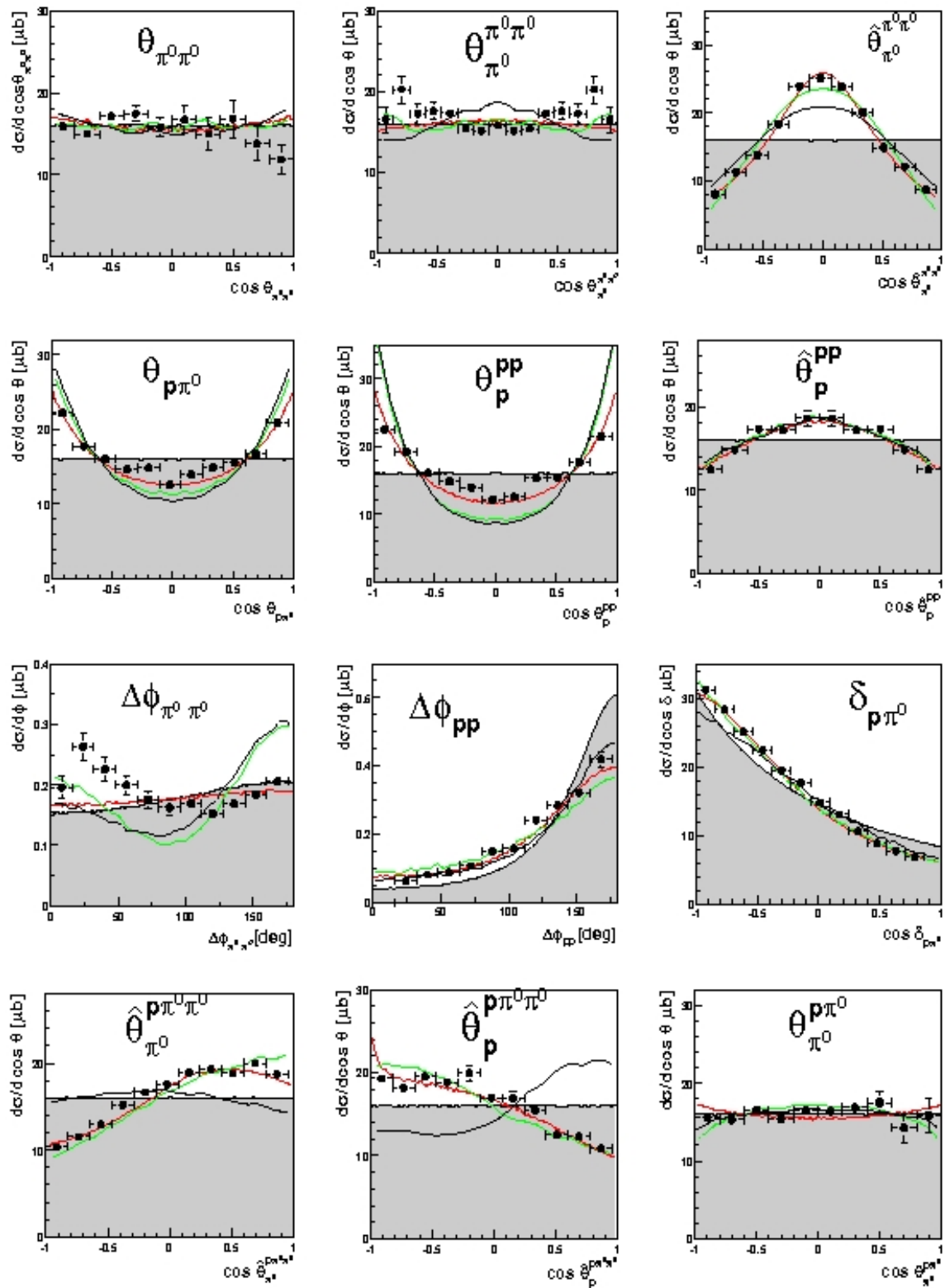
Appendix E: reaction pp→ppπ^{0}π^0 at T$_p$=1.2 GeV

Figure 6.6 *Same as Fig. 5.4 but for T$_p$=1.2 GeV*

Figure 6.6 *continued*
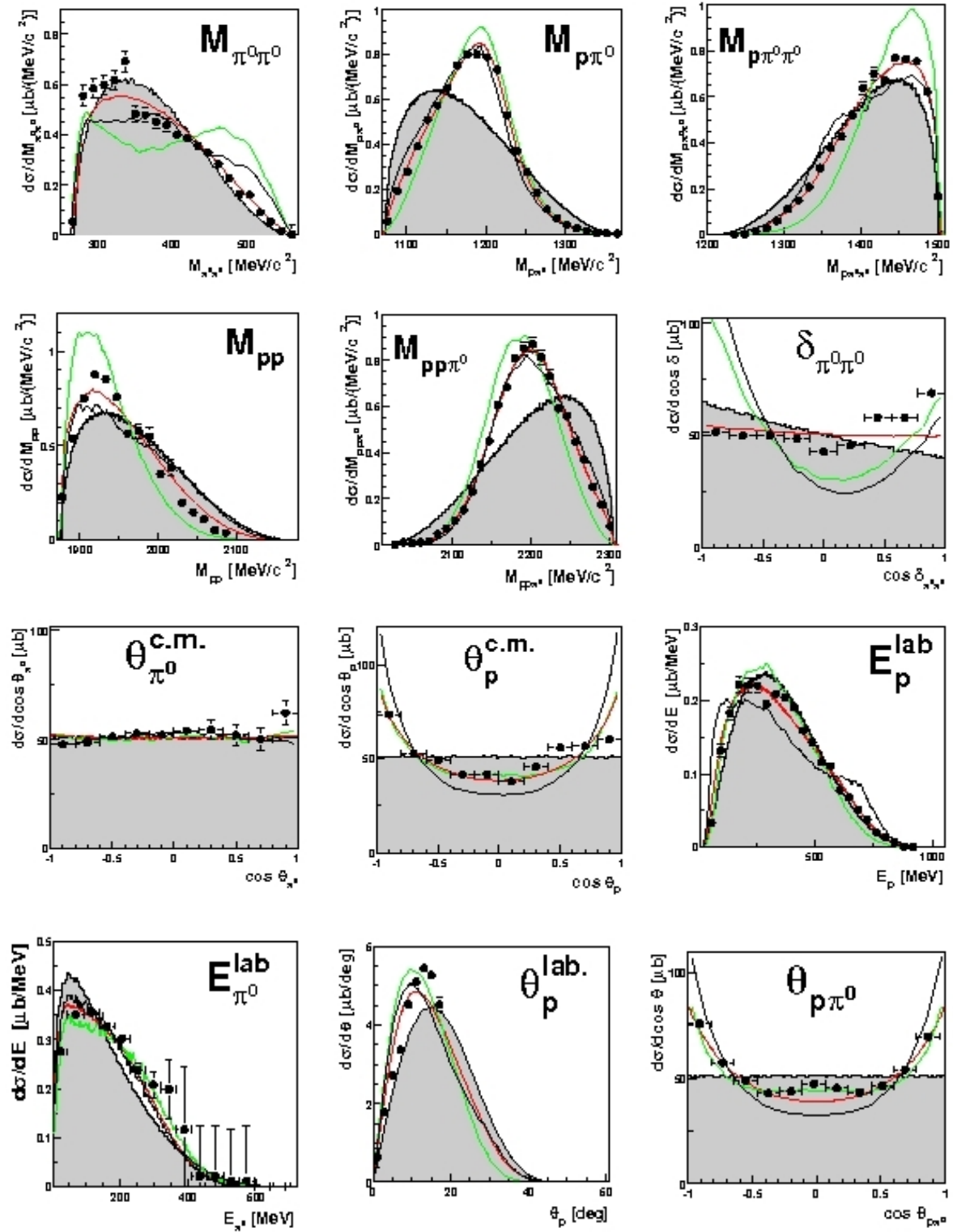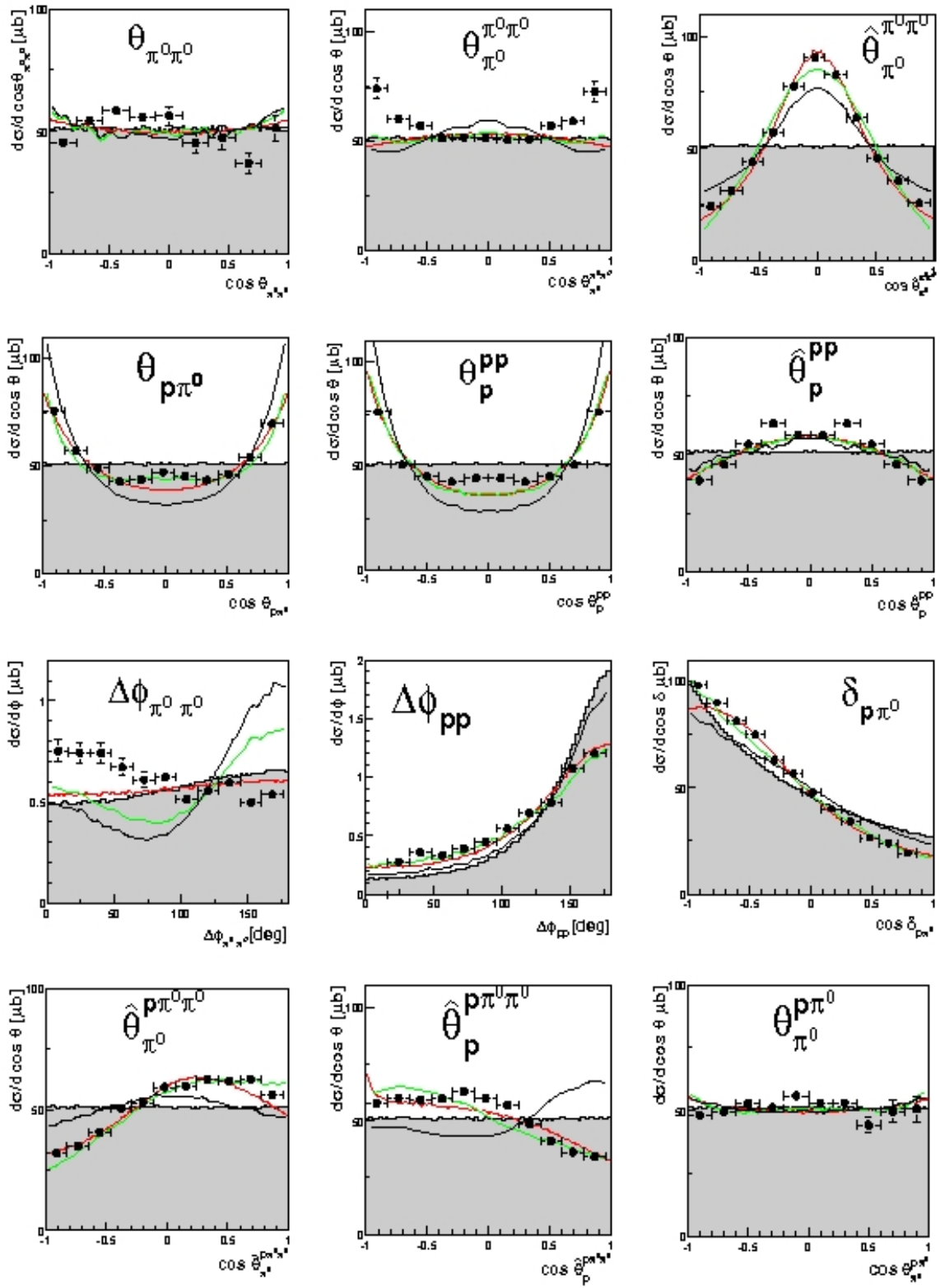
Appendix F: reaction pp→ppπ⁰π⁰ at T_p=1.3 GeV

Figure 6.7 *Same as Fig. 5.4 but for T_p=1.3 GeV*

Figure 6.7 *continued*

Appendix G: reaction pp→nnπ⁺π⁺ at T_p=1.1 GeV

In Fig. 6.8 the grey area denotes the phase space, the red lines are calculations for the $(\Delta\Delta)_{0^+}$ model (this ansatz includes only two propagators for Δ's without any angular changing), the black solid ones denote a modified Valencia model calculation with contributions from $\Delta\Delta$ and $\Delta(1600)$ excitation according to isospin decomposition. For the calculations of the $\Delta(1600)$ amplitude we used the calculation from Ref. [8] for diagram (9) with changing of the first Δ's mass to M=1600 MeV and width to Γ=350 MeV.

The data have been acceptance and efficiency corrected by the $(\Delta\Delta)_{0^+}$ model.

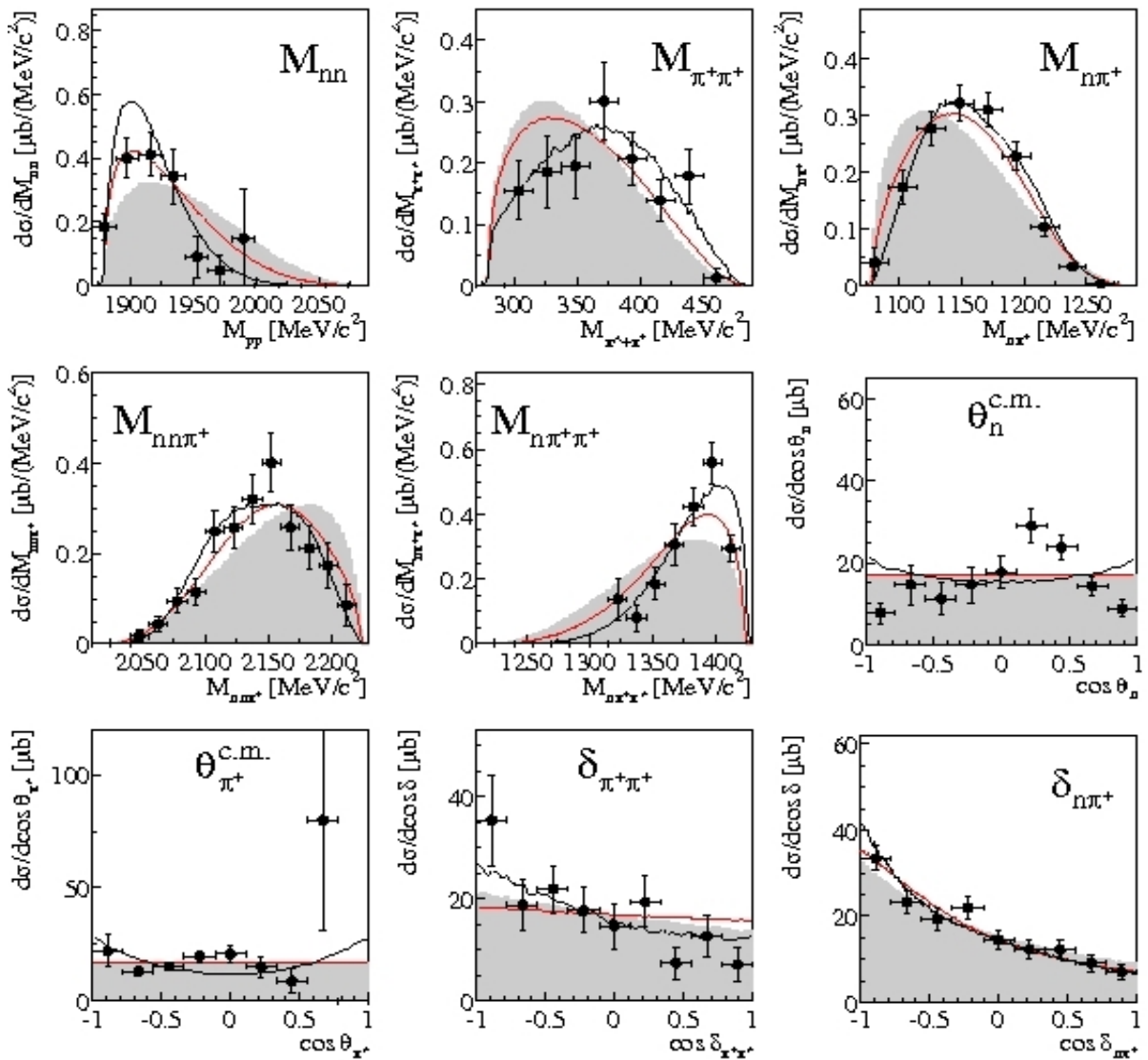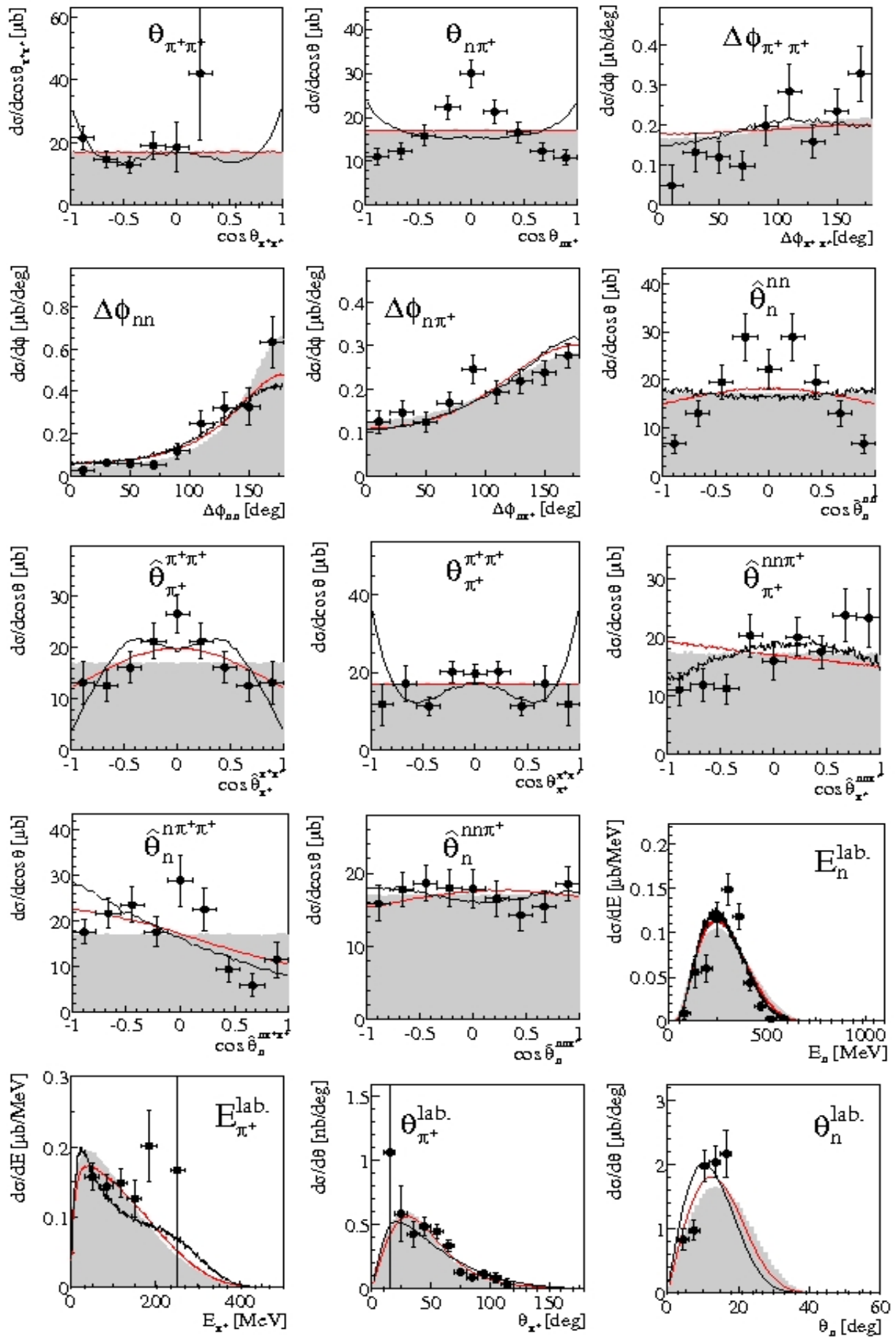All theoretical curves are normalized in area to the data.

Figure 6.8

Figure 6.8 *continued*

Appendix H: reaction pp→pnπ$^+$ at T$_p$=1.3 GeV

In the figures below the grey area denotes the phase space, the solid lines are calculations for the ansatz 4.4 with a=0.2 and b=0.3. In the calculations the Roper mass is M=1380 MeV and width is Γ=180 MeV.
The data have been corrected by ansazt (4.4).
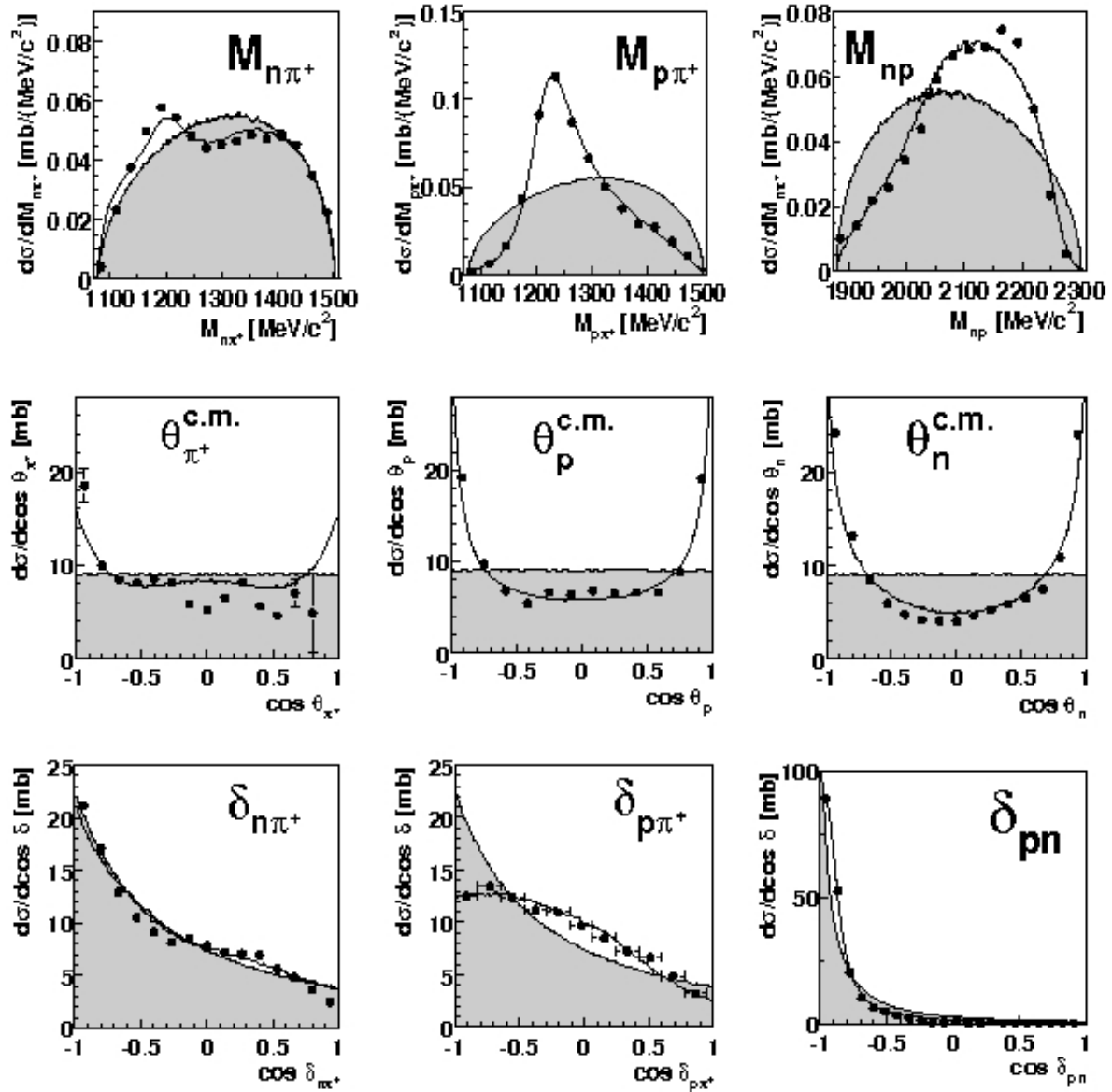All theoretical curves are normalized in area to the data.
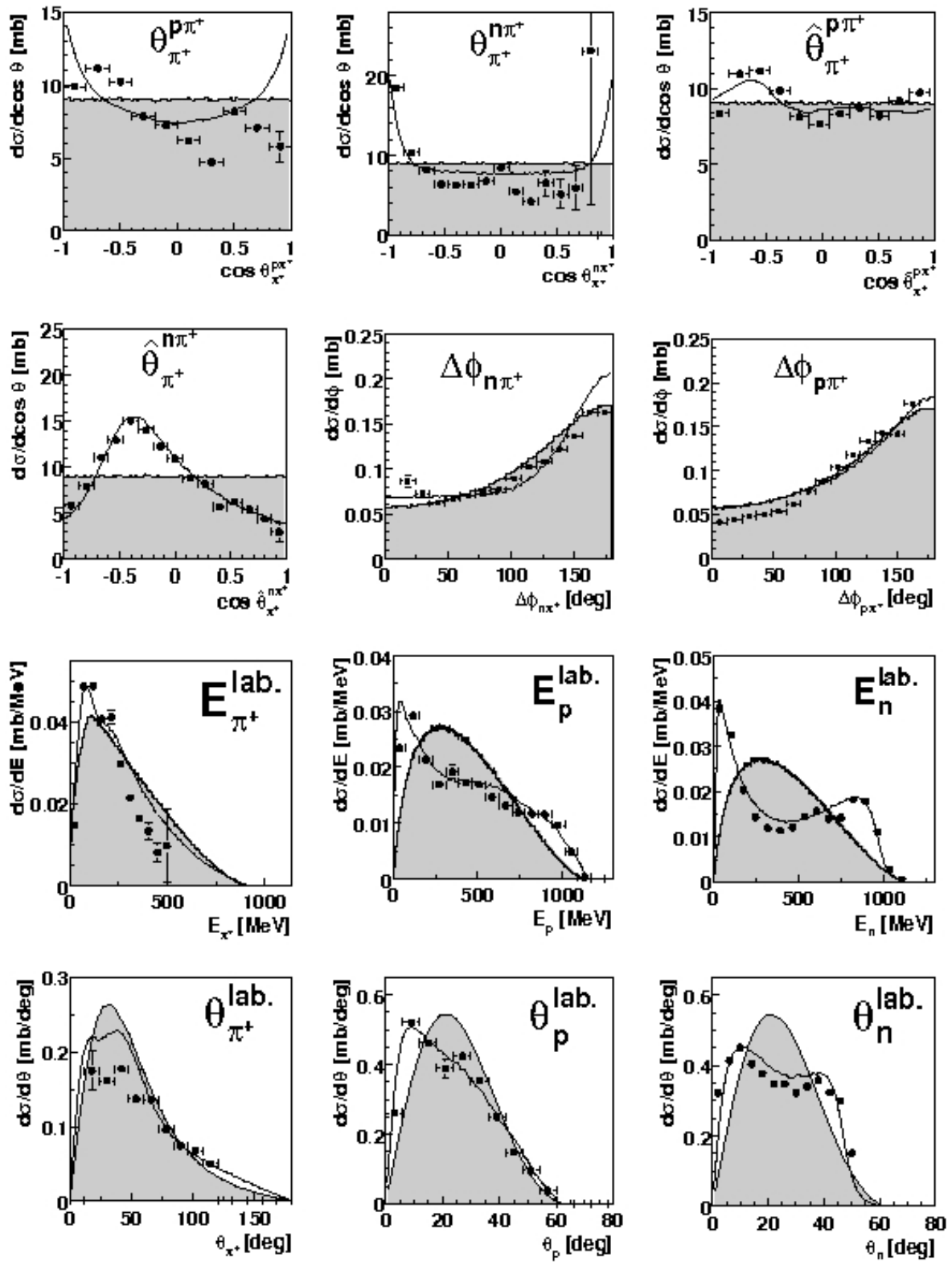

Figure 6.9

Figure 6.9 *continued*

105

Appendix I: reaction pp→ppπ⁰ at T_p= 0.895 GeV

In the figures below the grey area denotes the phase space, the solid lines are calculations for the ansatz 6.1.

$$A^2 \sim (1 + a \cdot \cos^2{}_{\pi^0}^{p\pi^0})D_\Delta^2(1 + b \cdot \cos^2{}_p^{pp}) \qquad\qquad 6.1$$

The coefficients *a* and *b* have been adjusted to data and have values *a*=3 and *b*=1.5. D_Δ denotes the Δ propagator, the best agreement with data we obtained at the Δ's mass 1230 MeV and width 80 MeV.
The data have been corrected by ansatz (6.1).
Fig. 6.10 shows data collected with the cluster trigger and Fig. 6.11 shows data collected with the energy trigger.
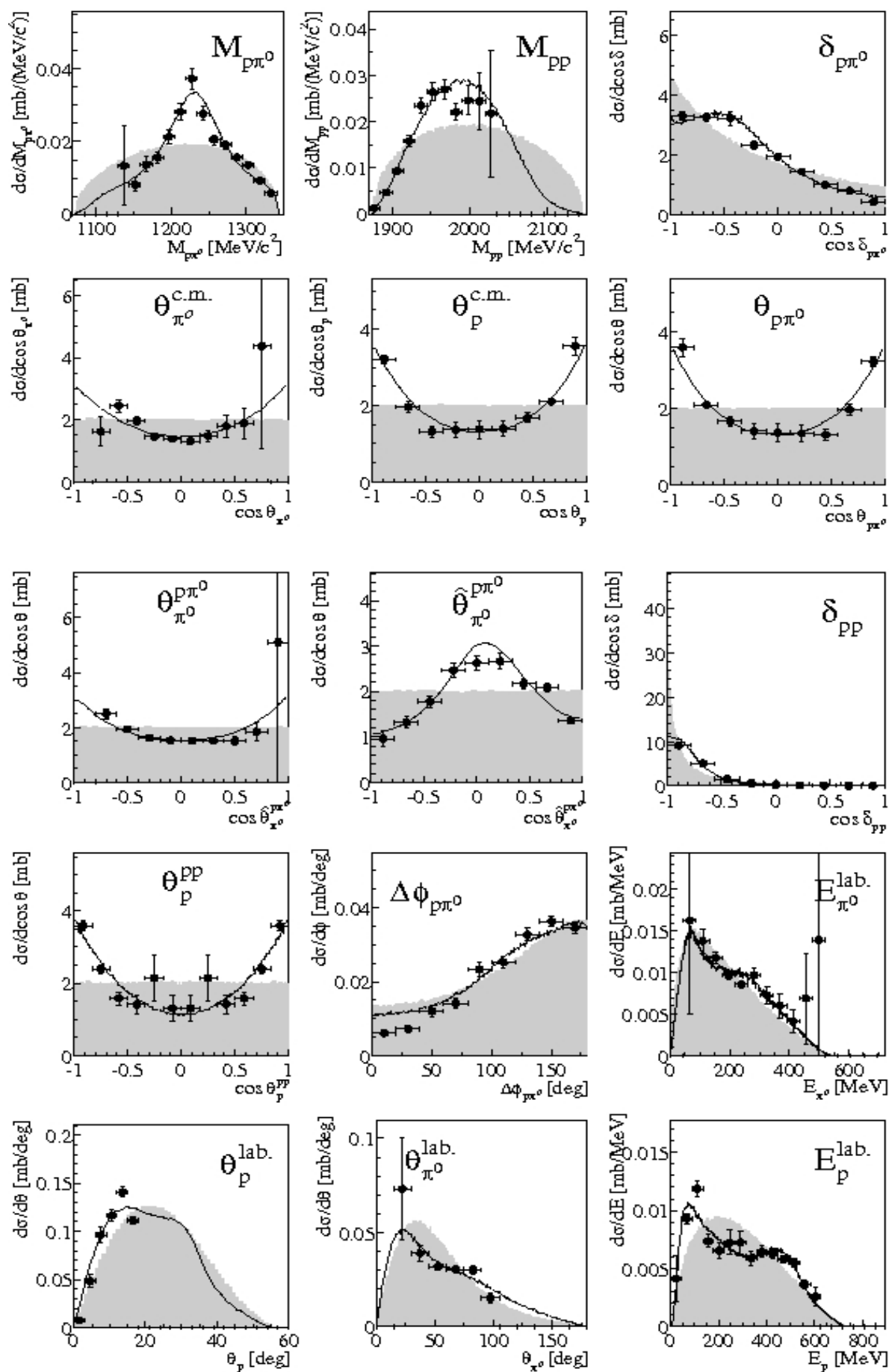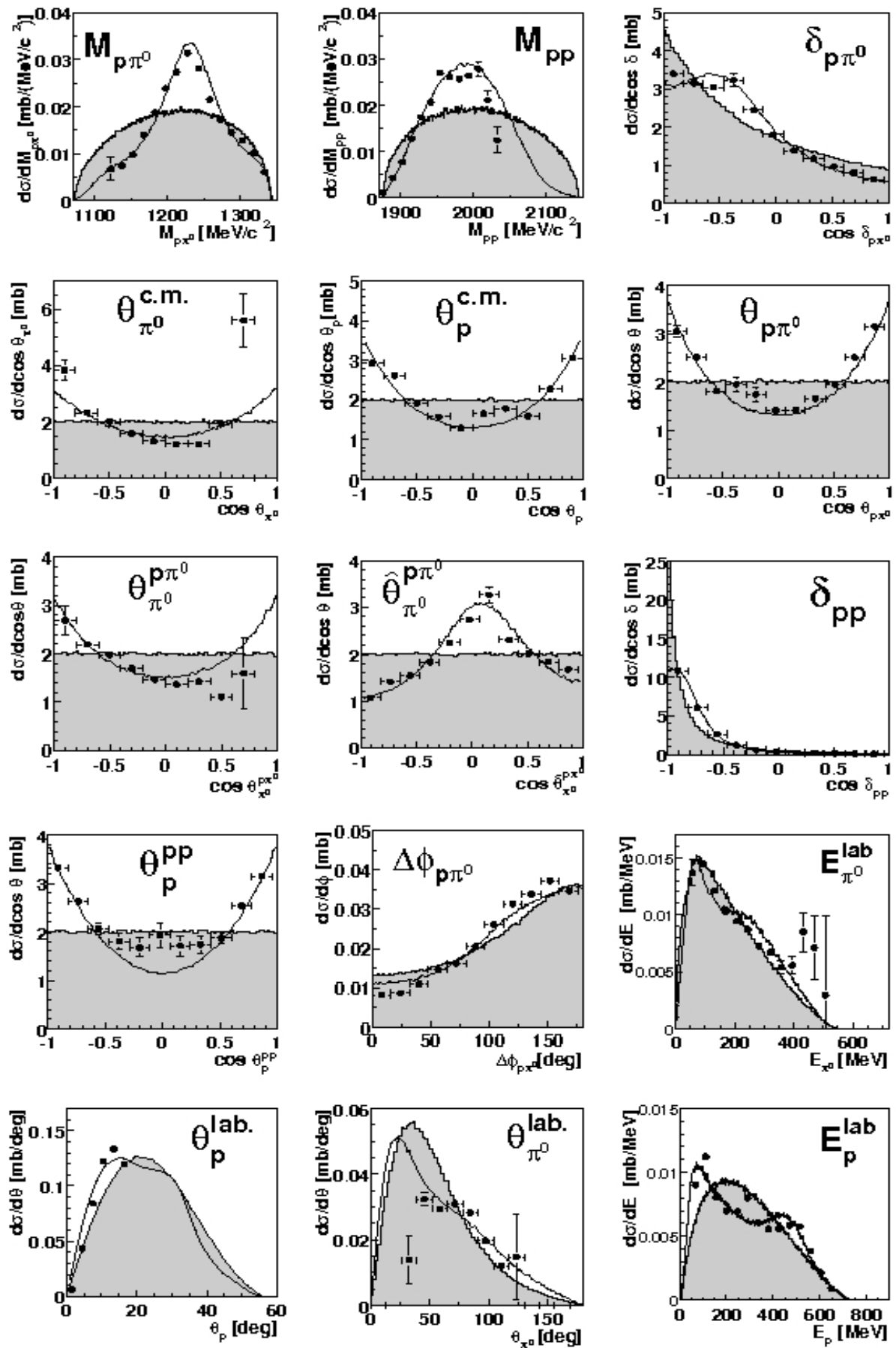All theoretical curves are normalized in area to the data.

Figure 6.10

Figure 6.11

Acknowledgments

I think the time, which I spent a PhD student in Tübingen, has been one of the best in my life not only because I could satisfy my curiosity at the University money, but because I met a lot a nice, interesting people, who always were ready to help me by advice, by critics, by joke.

I want to thank TSL colleges and first of all I am very thankful to Catharina Asbjork for her permanent help in the organization of accommodations in Uppsala. Nothing could be done in this work without expert explanations from Hans Calen, Kjell Fransson, Andrzey Kupsc, Josef Zlomanczuk. Now I cannot even count, how many times they patiently answered my stupid questions.

 I want to tanks Teresa Kupsc. Without her help in type reading, I think, the Roper analysis would never be performed.

I want to thanks Jan Greiff, who become my first teacher in a comprehension of underwater stones of the WASA analysis.

I am particularly grateful to Luis Alvarez-Ruso for using his code for the model calculations.

Of cause, there are no better people than WASA PhD students. Thank a lot Marek Jacewicz, Christian Pauly, Levent Demiros, Samson Keleta, Filippo Cappellaro, Henrik Pettersson, Karin Schonning, Micha Bashkanov. With your help I felt myself in a united team, in which I could ask, discuss, simply to talk about life.

I want to thanks my Tübingen colleges Eugeny Doroshkevich, Rudolf Meier, Gerhard Wagner for help in the understanding of my results and my mistakes.

I want to thanks out computer system administrator Arthur Erhardt. Without his help I would never be able to force my computer to calculate what I needed.

Especially want to thanks my supervisor Heinz Clement, who become practically my temporary "father" in Tübingen. He was not only my scientific leader, but he helped me a lot to solve many problems in my Tübingen life.

Thank you all.

References

[1] D. P. Barber et al., Phys. Rev. Lett. 43(1979) 830; M.Cacciari, hep-/0407187

[2] Ulf-G. Meissner, hep-ph/0408029

[3] F. Shimizu et al., Nucl. Phys. A 386(1982) 571; D. C. Brunt et al., Phys. Rev. 187(1969) 1856; L. Dakhno et al., Yad. Fz. 37(1983) 907

[4] W. Brodowski et al., Phys. Rev. Lett. 88(2002) 192301

[5] J. Pätzold et al., Phys. Rev. C67(2003) 052202

[6] R. Cool et al., Phys. Rev. 103(1959) 1082; W. Fichinger et al., Phys. Rev. 125(1962) 2082

[7] S. Lindenbaum and R. Sternheimer, Phys. Rev. 105(1957) 1874; Phys. Rev. 106(1957) 1107; Phys. Rev. 109(1958) 1723

[8] L. Alvarez-Ruso et al., Nucl. Phys. A 633(1998) 519

[9] W. Brodowski, PhD thesis, University of Tuebingen, 2001; J. Pätzold, PhD thesis, University of Tuebingen, 2002

[10] I. Seluzhenkov et al., Eur. Phys. J. A 18(2003) 321

[11] H.Clement, M. Kaskulov, E. Doroshkevich, Int. J. Mod. Phys. A20(2005) 674

[12] B. Trostell, Nucl. Instr. Meth. Phys. Res. A 362(1995) 41; C. Ekstrom et al., Nucl. Instr. Meth. Phys. Res. A 371(1996) 572

[13] J. Zabierowski et al., Phys. Scripta T99(2002) 159

[14] R. Ruber, PhD thesis, Uppsala Universitet, 1999

[15] M. Jacewicz, PhD thesis, Uppsala Universitet, 2004

[16] C. Pauly, PhD thesis, Hamburg Universitat, 2006

[17] F. Fransson, Phys. Scripta T99(2002) 176

[18] L. Demirrrrors, PhD thesis, Hamburg Universitat, 2005

[19] R. Craun and L. Smith, Nucl. Instr. and Meth. 80(1970) 239

[20] I. Koch, PhD thesis, Uppsala Universitet, 2004

[21] F. James, FWL − a General Monte-Carlo Phase Space Program, CERN Program Library Long Writeup W505, 1977

[22] GEANT − Detector Description and Simulation Tool, CERN Program Library Long Writeup W5013, 1993

[23] A. Kupsc, CELSIS-WASA Memo, 1998

[24] A. Pricking, private communications, 2007

[25] F. Fransson, private communications, 2004

[26] A. Konig and P.Kroll, Nucl. Phys. A 356(1981) 345

[27] E. Chiavassa et al., Phys. Lett. B 322(1994) 270

[28] S. Abd El-Bary et al., Eur. Phys. J. A 37(2008) 267

[29] J. Johanson, PhD thesis, Uppsala Universitet, 2000

[30] T. Skorodko et al., Eur. Phys. J. A 35(2008) 317

[31] N. Isgur and G. Karl, Phys. Rev. D 18(1978) 4187; S. Capstick and N.Isgur, Phys. Rev. D 19(1979) 2653

[32] O. Krehl et al., Phys. Rev. C 62(1999) 025207

[33] Ulf-G. Meissner and J. Durso, Nucl. Phys. A 430(1984) 670

[34] C. Hajduk and B. Schwesinger, Phys. Lett. B 140(1984) 172

[35] PDG, Phys. Lett. B 667(2008) 1

[36] R.A. Arndt et al., nucl-th/0605082

[37] H. Morsch et al., Phys. Rev. Lett. 69(1992) 1336: Phys. Rev. C 61(1999) 024002

[38] S. Hirenzaki et al., Phys. Rev. C 53(1996) 227

[39] M. Ablikim et al., Phys. Rev. Lett. 97(2006) 062001

[40] T. Ericson and W. Weise, „Pions and Nuclei", The international series of monographs on physics, Oxford 1988

[41] S. Huber and J. Aichelin, Nucl. Phys. A 573(1994) 587

[42] A. Sarantsev et al., Phys. Lett. B 659(2008) 94

[43] M.Bashkanov, private communications, 2005

[44] H. Müther, private communications, 2006

[45] H. Clement et al.,Int. J. Mod. Phys. A20(2005) 1747

[46] H. Boggild et al., Phys. Lett. B 302(1993) 510; D. Miskowiec et al., Nucl. Phys. A 610(1996) 237c

[47] R. Hanbury Brown and R.Q. Twiss, Nature 177(1956) 27; Nature 178(1956) 1046

[48] G. Baym, Acta Physica Polonica B 29(1998) 1839

[49] L. Dakhno et al.,Sov. J. Nucl. Phys. 37(1983) 540

[50] I. Juricic et al., Phys. Rev. D 39(1989) 1

[51] M. Bashkanov, PhD thesis, University of Tuebingen, 2006

[52] A. Abashian et al., Phys. Rev. Lett. 5(1960) 258; J. Banaigs et al., Nul. Phys. B 28(1971) 509; J. Banaigs et al., Nul. Phys. B 105(1976) 52

[53] T. Risser and M. Shuster, Phys. Lett. B 43(1973) 68

[54] M. Bashkanov et al., Phys. Rev. Lett. 10292009) 052301

[55] O. Khakimova, PhD thesis, University of Tuebingen, 2009

[56] L. Alvarez-Ruso, PhD thesis, University of Valencia, 1999

[57] T. Skorodko et al., submitted to Phys. Lett. B; nucl-ex/0906.3095